BRIDGING THE GAP BETWEEN ATOMISTIC AND CONTINUUM MODELS TO PREDICT DIELECTRIC AND THERMODYNAMIC PROPERTIES OF CONFINED FLUIDS

BY

MOHAMMAD HOSSEIN MOTEVASELIAN

DISSERTATION

Submitted in partial fulfillment of the requirements
for the degree of Doctor of Philosophy in Mechanical Engineering
in the Graduate College of the
University of Illinois at Urbana-Champaign, 2020

Urbana, Illinois

Doctoral Committee:

Professor Narayana R. Aluru, Chair and Director of Research
Professor Emad Tajkhorshid
Professor Sungwoo Nam
Assistant Professor Charles Sing

Abstract

Nanoconfined fluids are ubiquitous and play a prominent role in nature and technological applications. Understanding the physics of the confined fluids and obtaining atomic-level insights into their unusual properties is essential to develop and design novel nanofluidic applications related to energy, water, and health. For systems involving multiple length and time scales, atomistic simulations become forbiddingly expensive. On the other hand, classical continuum theories fails to accurately describe the fluid properties at atomic level. Thus, there is a need for a multiscale frame work to maintain the balance between accuracy and rigor of atomistic simulations and efficiency of continuum frameworks. In this work, we present an empirical potential-based quasi-continuum theory (EQT) that provides a framework to seamlessly integrate atomistic details into a continuum-based models. The main idea in EQT is to bridge the gap between atomistic and continuum models by incorporating molecular correlations, interatomic interactions, and anisotropic effects at a continuum level. We show that EQT can be used in classical density functional theory to predict the thermodynamic properties for confined fluids. Moreover, we present a hierarchical coarse-grain (CG) approach in which we coarse grain the degrees of freedom of polar liquids from the detailed all-atom (AA) level to the cheaper particle-based CG level, and to the continuum-based level. Our goal is to devise CG interaction potentials for polar liquids that reproduces not only the structure but also accurately describe the dielectric permittivity and its anisotropic nature in the confinement. Using the CG potentials in EQT we show that neglecting the tensorial form of the dielectric permittivity in the Poisson equation leads to incorrect screening and orientational polarization profiles near interfaces. Thus, using extensive molecular dynamics simulations, statistical-mechanical theories and multiscale methods, we study the out-of-plane (z-axis) and in-plane (x-y) dielectric response of protic and aprotic fluids confined inside slit-like graphene channels. We find a universal reduction in perpendicular permittivity for all the fluids. Whereas, the parallel dielectric response of polar liquids is enhanced and is proportional to dipolar correlations and density oscillation next to the interface. The perpendicular reduction and in-plane enhancement of the dielectric permittivity is attributed to the favorable in-plane (x-y plane) dipole-dipole electrostatic interactions of the interfacial fluid layer. These findings have important consequences in, developing accurate coarse-grained force fields and improving the solvent-implicit approaches often used in biology and continuum theories such as the Poisson-Boltzmann (PB) equation for accurate prediction of capacitance in the electric double-layer capacitors.

To my family.

Acknowledgments

First and foremost, I would like to express my gratitude and appreciation to my advisor, Prof. Narayana R. Aluru. I am deeply grateful for his guidance and support during my PhD. I have learned so much from him because of his patience in discussions, his passion for solving difficult problems, and his integrity in conducting research. I would also like to thank Prof. Emad Tajkhorshid, Prof. Sungwoo Nam, and Prof. Charles Sing or serving on my doctoral committee. I am also grateful to Dr. Sikandar Mashayak for being my mentor during the early years when I joined the Computational Multiscale Nanosystems group.

I would also like to acknowledge the National Science Foundation (NSF), Air Force Office of Scientific Research (AFOSR), Center for Enhanced Nanofluidic Transport (CENT), and Energy Frontier Research Center funded by the U.S. Department of Energy for financial support. I also acknowledge the computing resources provided by the Illinois Campus Cluster Program, Blue Waters, and Texas Advanced Computing Center.

Above all, I would like to thank my family especially my parents, Shohreh and Mohammad Reza, for their love, encouragement, and patience throughout the long and rewarding journey of the graduate school.

Table of Contents

List of Tables

List of Figures

Chapter 1

Introduction

1.1 Background and motivation

The physics and properties of confined fluids and their mixtures at length scales ranging from a few angstroms to micrometers are quite different than those in the macroscopic scale (bulk) [2–4]. The major reason for this is the inhomogeneity imposed by the confined environment. The interplay between the wall-fluid and the fluid-fluid interactions significantly alters the molecular configuration, structural correlations, dielectric properties, thermodynamic, and dynamical properties of a confined fluid in comparison to its bulk phase. Density oscillations [5], unusually high pressure regions [6, 7], existence of different phases [8, 9], anomalous dielectric properties [10], dynamical anomalies [11, 12], and wetting and capillary phenomena [13] are few examples of how the presence of an interface can alter the behavior of the fluid at sub-micrometer scales. Therefore, confined fluids have many applications such as nanofiltration [14–17], drug delivery [18, 19], enhanced oil recovery [20, 21], nano super-compressors [22], lubrication [23], and geophysical applications [24], CO2 reduction [25], and energy storage devices [26]. Therefore, to be able to design a novel nanofluidic device, the foremost step is to study and understand the physics of the confined fluid and obtain atomic-level insights into their unusual properties. To explain the molecular origin of the various phenomena occurring in the confinement, in addition to the experiments, both theory and computer simulations are of critical importance. Moreover, in some cases obtaining a molecular insight from experiments may not be accessible or hindered by high noise to signal ratio for nanoscale devices [27, 28]; thus, theory and computer simulations become viable tools to understand the underlying physics.

Over the past years, density functional theory (DFT) and high resolution atomistic simulations such molecular dynamics (MD) and Monte Carlo (MC) have been used to study interfacial fluids for a variety of applications in biology, physics, and material science. From these methods one can obtain molecular insights into the nature of different interactions and interpret the physical phenomena based on the knowledge of statistical mechanics. However, in many practical systems the time- and length-scales that need to be studied typically prohibits the use of fully atomistic simulations. For example in biological systems, the number of water molecules is of the order of several thousands to millions [29], making these methods forbiddingly expensive to simulate systems involving multiple length scales and timescales ranging from the quantum to atomic to continuum scales. On the other hand, although classical continuum theories, such as Navier-Stokes equations, are computationally efficient, they fail to accurately predict the properties of the atomically confined systems [30]. Therefore, there is a need to develop a multiscale method that is as fast as classical continuum methods, and as accurate as atomistic simulations.

In this thesis, we introduce the empirical potential-based quasi-continuum theory (EQT) which is a multiscale approach that provides a framework to seamlessly integrate atomistic details into a continuum-based model such as the Nernst-Planck (NP) equation. The main idea in EQT is to calculate the potential energies in a continuum approximation that involves information developed at the molecular level. For simple liquids such as Lennard-Jones (LJ), the atomistic information, can be directly incorporated into NP. On the other hand, for charged or dipolar systems, where electrostatic interaction plays an important role, bridging the gap between atomistic to the continuum models becomes more complicated. For such systems, in EQT we adopt a hierarchical coarse-graining approach. The objective of any CG simulation is to lower the atomistic resolution by representing the system with fewer degrees of freedom, while retaining the necessary details to capture the quantity of interest. Therefore, using the CG approach, we can bridge the gap between atomistic and continuum models within the EQT framework.

EQT was developed to predict structure and potential of mean force profiles of Lennard-Jones fluids, carbon dioxide and water in slit-like channels ranging from few Angstroms to hundreds of nano-meters width [31–35]. In order to predict properties other than the structure EQT has to be coupled continuum frameworks other than NP equation. For example, EQT can be coupled with classical function theory (cDFT) to predict various thermodynamic properties such as adsorption, local pressure tensor, surface tension, and solvation force of confined fluids [36]. Coupled with Poisson equation, EQT can predict electrolyte density distributions and electrostatic potential in electric double layers (EDL) [37, 38]. However, recently it has been shown that accurate representation of electrostatic interactions in EDLs, especially solvent screening effects, requires a careful evaluation of solvent dielectric permittivity.

Similar to the structural and dynamical changes that a fluid undergoes in the vicinity of an interface, the dielectric response of the confined fluid is no longer a scalar quantity (as is the case in the bulk) and is a second ranked tensor exhibiting an anisotropic behavior in different spatial directions (e.g. perpendicular, $\varepsilon_\perp$, or parallel, $\varepsilon_\parallel$, to a flat interface) [39, 40]. Such an anisotropic behavior implies a strong preferred directionality for electrostatic interactions [41] and can be very important in understanding dissociation in nanoconfinement [42, 43], dielectrophoretic deposition of carbon nanotubes (CNTs) [44], developing accurate coarse-grained force fields and improving the solvent-implicit approaches often used in biology and continuum theories such as the Poisson-Boltzmann (PB) equation [45] for accurate prediction of capacitance in the electric double-layer capacitors [46].

Therefore, in this thesis, we systematically develop an extended CG dipole model for polar liquids to capture not only RDF but also diffusion and bulk dielectric permittivity. We used our model in the EQT-Poisson framework to predict structure, parallel dielectric permittivity and polarization of water confined in slit-like channels. Furthermore, using extensive MD simulations we investigate the perpendicular response of polar liquids under the confinement. We develop a multiscale parallel-plate capacitor model to predict the perpendicular permittivity of polar liquids for confinement ranging from only few angstrom to micrometer in width. Finally, we generalize the EQT framework for mixture of confined fluids.

1.2 Thesis overview

The thesis is organized as follows. Chapter 2 describes the fundamentals on the EQT for mixtures. We introduce EQT as a multiscale method that seamlessly integrate atomistic details into a continuum-based model such as Nernst-Planck equation. We demonstrate the ability of EQT to accurately predict density and potential of mean force of confined fluid mixtures by simulating LJ fluid mixtures confined inside slit-like channels.

In chapter 3, the EQT potentials are used within the classical density functional theory (cDFT) in order to obtain thermodynamic properties other than the fluid structure. In this chapter, brief overview of the cDFT frame work is presented. Furthermore, necessary thermodynamic relations are derived and discussed. Various thermodynamic properties such as density profiles, adsorption, local pressure tensor, surface tension, and solvation force are predicted for system of confined LJ mixtures by the EQT-cDFT approach and compared with the MD simulation results.

In chapter 4, we report a multiscale investigation of water inside graphene slit-like channels that extends from the detailed all-atom level (AA) to the cheaper particle-based coarse-grained (CG) level, and to the continuum-based level. We have systematically developed an extended dipole-based CG model to reproduce the RDF, diffusion coefficient, and bulk dielectric permittivity of the underlying all-atom(AA) reference model. Furthermore, we use the empirical EQT framework to predict the density and polarization of water molecules inside nanoslit channels of various widths. Finally, by using coarse-grained molecular dynamics (CGMD) and EQT simulations, we comment on the applicability of dipolar-based CG models in reproducing the structure of water near charged interfaces.

In chapter 5, using extensive MD simulations, statistical-mechanical theories and multiscale methods, we study the out-of-plane (z-axis) dielectric response of protic and aprotic fluids confined inside slit-like graphene channels. We develop a multiscale parallel-plate capacitor model to predict the perpendicular permittivity of polar liquids for confinement ranging from only few angstrom to micrometer in width.

In chapter 6, we study the parallel (x-y) component of dielectric permittivity. Using statistical-mechanical theories and MD simulations, we show an explicit relation between the parallel dielectric permittivity, density variations, and dipolar correlations for protic and aprotic fluids confined in slit-like channels. We analyze the importance of dipolar correlations on the parallel dielectric permittivity inside large and extreme confinements. Finally, the concluding remarks of this thesis work are presented in Chapter 7.

Chapter 2

Empirical potential-based quasi-continuum theory (EQT)

2.1 EQT framework

Density is one of the most fundamental variables of confined fluid systems. Unlike the bulk system, the density of a confined fluid is inhomogeneous. For example, as shown in Fig. 2.1, for a slit-like geometry the inhomogeniety only exists in the z direction, and thus, the equilibrium particle density distribution can be obtained via solving the 1-D steady state Nernst-Planck (NP) equation,

$$\frac{d}{dz}\left(\frac{d\rho}{dz}+\frac{\rho}{k_{\mathrm{B}}T}\frac{dU}{dz}\right)=0 \tag{2.1}$$

with boundary conditions

$$\rho(0)=0 \tag{2.2a}$$

$$\rho(H)=0 \tag{2.2b}$$

$$\frac{1}{H}\int_0^L \rho(z)\,dz=\rho_{\mathrm{avg}} \tag{2.2c}$$

where, $\rho(z)$ and $U(z)$ are the density and total potential of the fluid at location z, respectively, T is the fluid temperature, k_{B} is the Boltzmann constant, H is the channel width, ρ_{avg} is the average density of the fluid inside the channel, and z-axis is normal to the wall. The solution of Eqs. 2.1 and 2.2 obeys the Boltzmann distribution,

$$\rho(z)=\rho_{\mathrm{ref}}\exp\left(-\frac{U(z)-U_{\mathrm{ref}}}{k_{\mathrm{B}}T}\right), \tag{2.3}$$

where ρ_{ref} and U_{ref} are the reference density and potential of the fluid, respectively. Due to the fact that the channel is in equilibrium with a bulk reservoir, the reference point can be taken to be the bulk, where the fluid thermodynamic properties are known *a priori*.

Eq. (2.1) relates density to the potential energy. To solve for density, one requires an expression for the total potential energy. In general, for a confined fluid mixture the total potential per particle at a given

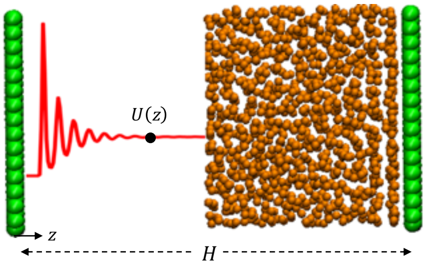

Figure 2.1: Atomistic (orange color) and continuum (red color) representation of confined fluid. The walls are represented in green color separated by a distance H and $U(z)$ is the total potential at location z.

location $\boldsymbol{r}$, is the sum of the wall-fluid and the fluid-fluid potentials (see Fig. 2.2):

$$U_i(\boldsymbol{r}) = U_i^{\mathrm{wf}}(\boldsymbol{r}) + U_i^{\mathrm{ff}}(\boldsymbol{r}) \tag{2.4}$$

where $i = 1, 2, \cdots, m$ is the label of a fluid component, m is the number of fluid species in the mixture , U_i^{wf} and U_i^{ff} are the wall-fluid and fluid-fluid potential of component i, respectively.

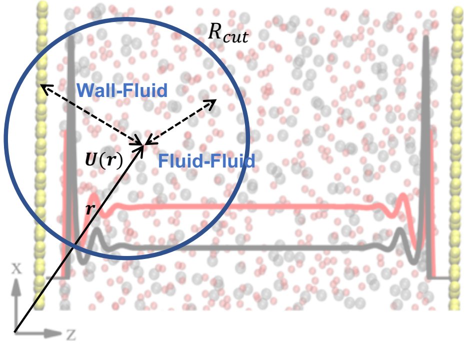

Figure 2.2: Schematic illustration of the total potential $U(\boldsymbol{r})$ as the sum of the wall-fluid and fluid-fluid potentials. The red and black colors represent a binary fluid mixture confined in slit-like channel.

The main idea of EQT is to incorporate atomistic details into U_i by using empirical pair potentials, and continuum representation of the wall and fluid atoms, i.e, their local densities.

2.1.1 Wall-fluid potential

In the continuum approximation, the wall structure is locally modeled as a continuous medium with a particle density, $\rho_{\mathrm{wall}}(\boldsymbol{r})$ (see Fig. 2.3). Hence, the wall-fluid potential of the i^{th} component is expressed as,

$$U_i^{\mathrm{wf}}(\boldsymbol{r}) = \int \rho_{\mathrm{wall}}(\boldsymbol{r}')u_i^{\mathrm{wf}}(r)d\boldsymbol{r}', \tag{2.5}$$

where $u_i^{\mathrm{wf}}(r)$ is the effective pair potential between the i^{th} fluid component and the wall atom, $\boldsymbol{r}$ and $\boldsymbol{r'}$ are the position vectors, and $r = |\boldsymbol{r} - \boldsymbol{r'}|$. Note that in Eq. 2.5, $\boldsymbol{r} = x\boldsymbol{i} + y\boldsymbol{j} + z\boldsymbol{k}$ is a general position vector. In the case of a 1-D slit channel, the system is periodic in x and y dimensions and therefore, we consider only the z-variations of the properties, i.e., $U_i^{\mathrm{wf}}(\boldsymbol{r}) = U_i^{\mathrm{wf}}(x, y, z) = U_i^{\mathrm{wf}}(z)\,\forall\, x, y$.

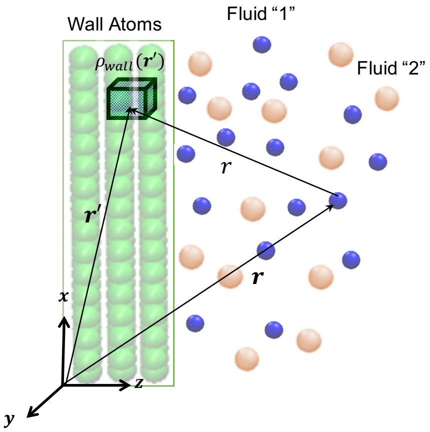

Figure 2.3: Illustration of wall-fluid potential calculation for mixture of confined fluid and the continuum approximation of wall in the EQT framework

2.1.2 Fluid-fluid potential

Calculating the fluid-fluid interactions is a non-trivial task. In a continuum frame work such as Navier-Stokes equations, the inter-atomic interactions between the fluid particles are neglected. However, the fluid-fluid interactions give rise to the finite size, i.e., excluded volume effects, dispersion attraction, and particle-particle correlations in the fluid medium [47]. Thus, Unlike the wall-fluid potential, a complete description of an inhomogeneous fluid requires the knowledge of density and pair correlation function, $g^{(2)}(\mathbf{r}, \mathbf{r}')$, that contains the information of particle-particle spatial correlations between the points $\mathbf{r}$ and $\mathbf{r}'$. Hence, the fluid-fluid potential can be expressed as,

$$U_i^{\mathrm{ff}}(\boldsymbol{r}) = \sum_{j=1}^{m} \int \rho(\boldsymbol{r'}) u_{ij}^{\mathrm{ff}}(r) g_{ij}^{(2)}(\boldsymbol{r}, \boldsymbol{r'}) d\boldsymbol{r'}, \tag{2.6}$$

where $u_{ij}^{\mathrm{ff}}(r)$ is the effective pair potential between components i and j. For example, in the case of the binary mixture of fluids (see Fig. 2.4), the total fluid potential at location $\boldsymbol{r}$ for the fluid component ”1” can be written as follows,

$$U_1^{\mathrm{ff}}(\boldsymbol{r}) = \int \rho_1(\boldsymbol{r'}) u_{11}^{\mathrm{ff}}(r) g_{11}^{(2)}(\boldsymbol{r}, \boldsymbol{r'}) d\boldsymbol{r'} + \int \rho_2(\boldsymbol{r'}) u_{12}^{\mathrm{ff}}(r) g_{12}^{(2)}(\boldsymbol{r}, \boldsymbol{r'}) d\boldsymbol{r'}. \tag{2.7}$$

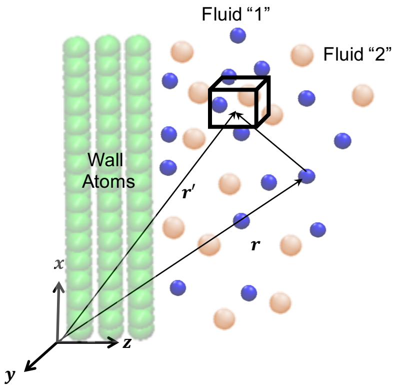

Figure 2.4: Illustration of fluid-fluid potential calculation for mixture of confined fluid.

The challenging term in Eq. (2.7) is the pair correlation function, as its inhomogeneity makes the calculations intractable [48]. Thus, in order to proceed further, we need to make an approximation for the pair correlation function. There are several approximations regarding the pair correlation which can classified into three categories: Mean field approximation (MFA), fundamental measure theory, and correlation correction potentials.

Mean field approximation

Mean field approximation has been widely used in the literature due to its simplicity and convenience. Basically in MFA, the structural correlations are neglected and thus, $g^{(2)}(\mathbf{r}, \mathbf{r}')$ is approximated by 1. Therefore, the fluid-fluid potential, $U_i^{\mathrm{ff}}(\boldsymbol{r})$ is given by

$$U_i^{\mathrm{ff}}(\boldsymbol{r}) = \sum_{j=1}^{m} \int \rho(\boldsymbol{r}') u_{ij}^{\mathrm{ff}}(r) d\boldsymbol{r}'. \tag{2.8}$$

Despite its convenience, MFA can be quantitatively problematic and even sometimes qualitatively incorrect [49, 50]. In addition, in Eq. 2.8, as $r \to 0$, the $u^{\mathrm{ff}}(r) \to \infty$. Consequently, this causes a numerical divergence in Eq. 2.8. To address these issues, one can approximate the hard repulsion core of the fluid-fluid pair potential by a softer function [31–34]. Choosing the soft core is not a trivial task and is numerically very sensitive to the choice of the excluded volume.

Correlation correction approach

To circumvent the aforementioned problems with MFA and soft core approach, the inhomogeneous pair correlation function can be approximated by the bulk radial distribution function (RDF), $g(r)$ [51–53]. Except for the system of hard spheres, estimating the bulk RDF for even simple LJ system is not straight forward, unless one resort to newly emerging solutions via machine learning [54]. On the other hand, there exist analytically expressions to obtain the bulk RDF of hard sphere system. A hard sphere fluid is an important reference system to model the short-range steep repulsion part of the fluid-fluid inter-particle interactions. One can imagine the system of hard sphere fluid as a pack of billiard balls, impenetrable for $r < d_{\mathrm{hs}}$, where d_{hs} is the diameter of the hard sphere, and zero attraction elsewhere, i.e.,

$$u_{\mathrm{hs}}(r) = \begin{cases} \infty, & r \leq d_{\mathrm{hs}} \\ 0, & \text{elsewhere} \end{cases} . \tag{2.9}$$

Although there are no attractive forces between the hardsphere particles, the repulsive forces and thus excluded volume effects affect the arrangement of the particles. Therefore, we approximate the inhomogeneous pair correlation function by the RDF of uniform hard spheres at the bulk density, ρ_{b}, i.e,

$$g^{(2)}(\mathbf{r}, \mathbf{r}') \approx g_{\mathrm{hs}}(r). \tag{2.10}$$

Similar approach to approximate the fluid-fluid correlations has been used by Tang and Wu [55]. To fully determine the hard sphere radial distribution function, we need to know the packing fraction $\eta = \frac{\pi \rho_{\mathrm{b}} d_{\mathrm{hs}}^3}{6}$. The hard sphere diameter for each fluid component can be calculated based on the relation proposed by Barker and Henderson [56],

$$d_{\mathrm{hs}}(T) = \int_0^{\sigma} (1 - \exp[-\frac{u^{\mathrm{ff}}(r)}{k_B T}]). \tag{2.11}$$

where σ is the length-scale parameter for LJ interaction. The RDFs are obtained using existing analytical expressions for additive hard sphere mixtures based on Percus-Yevick approximation [57, 58]. However, the hard sphere RDF approximation may not accurately reproduce the properties of a real fluid and can be problematic for inhomogenous systems [59]. Therefore, to account for these shortcomings, we add a correlation-correction potential (CCP), $u^{\mathrm{ff}}_{\mathrm{ccp}}$, and reformulate Eq. 2.8 as,

$$U_i^{\mathrm{ff}}(\mathbf{r}) = \sum_{j=1}^{m} \int \rho(\mathbf{r}') \left(u_{ij}^{\mathrm{ff}}(r) g_{ij}^{\mathrm{hs}}(r) + u^{\mathrm{ff}}_{\mathrm{ccp},ij}(r) \right) d\mathbf{r}'. \tag{2.12}$$

In EQT, $u^{\text{ff}}_{\text{ccp}}$ is modeled using uniform cubic B-splines as

$$u^{\text{ff}}_{\text{ccp}}(r) = \begin{bmatrix} 1 & t & t^2 & t^3 \end{bmatrix} \frac{1}{6} \begin{bmatrix} 1 & 4 & 1 & 0 \\ -3 & 0 & 3 & 0 \\ 3 & -6 & 3 & 0 \\ -1 & 3 & -3 & 1 \end{bmatrix} \begin{bmatrix} c_j \\ c_{j+1} \\ c_{j+2} \\ c_{j+3} \end{bmatrix}, \tag{2.13}$$

where the separation interval from 0 to the cut-off, $R^{\text{ff}}_{\text{cut}}$, is discretized into $n-1$ segments, $\{r_0, r_1, r_2, ..., r_{n-1}\}$, of equal size $\Delta r = R^{\text{ff}}_{\text{cut}}/(n-1)$ such that $r_i = i \times \Delta r$ $(i \in (0...n-1))$, $\{c_0, c_1, c_2, ..., c_{n+1}\}$ are the spline knots, the index j satisfies the condition $r_j \leq r < r_{j+1}$, and $t = \frac{r - r_j}{\Delta r}$.

Hard sphere functional approach

A hard sphere fluid is an important reference system to model the short-range steep repulsion part of the fluid-fluid inter-particle interactions. Due to the short-range repulsion each fluid molecule has a volume which is not accessible to other molecules. This effect is known as the excluded volume effect. The short-range repulsion plays a dominant role in determining the structure of fluids especially at high densities [60].

Rosenfeld's fundamental measure theory (FMT) [61] provides a framework to model the excess (over the ideal gas) free energy of inhomogeneous fluids due to the short-range steep repulsive part of inter-particle interactions. It accounts for both the excluded volume effects and pair correlations in an inhomogeneous fluid due to the hard repulsive part of pair interactions. In FMT, the excess hard sphere free energy, $F^{\text{ex}}_{\text{hs}}[\rho_i(\mathbf{r})]$, is calculated using [61–63],

$$F^{\text{ex}}_{\text{hs}}\left[\rho_i(\mathbf{r})\right] = k_{\text{B}}T \int \Phi\left[n_\alpha\left(\boldsymbol{r}\right)\right] d\boldsymbol{r}, \tag{2.14}$$

where Φ is the reduced free energy density, and n_α are the set of weighted densities that come in the scalar and the vector forms, and are defined as,

$$n_\alpha\left(\boldsymbol{r}\right) = \sum_{j=1}^{m} \int d\boldsymbol{r}' \rho_j\left(\boldsymbol{r}'\right) \omega_{j,\alpha}\left(\boldsymbol{r} - \boldsymbol{r}'\right), \tag{2.15}$$

In Eq. 2.15, $\omega_{j,\alpha}$ are the weight functions for each fluid component that are related to the geometrical measures (center of mass, surface area, and volume) of a spherical particle of radius R_{hs}. The detailed implementation of the above functionals and the weight functions in a slit channel are given in the appendix of Ref [37]. Therefore, in the FMT, the repulsive part of the fluid-fluid potential, $U^{\text{ff}}_{\text{hs}}(\boldsymbol{r})$, can be obtained by taking functional derivative of $F_{\mathrm{hs}}^{\mathrm{ex}}$ (Eq. 2.14):

$$U_{i,\mathrm{hs}}^{\mathrm{ff}}(\boldsymbol{r}) = k_{\mathrm{B}}T \int d\boldsymbol{r}' \frac{\partial \Phi\left(\{n_\alpha\}\right)}{\partial n_\alpha} \frac{\delta n_\alpha\left(\boldsymbol{r}'\right)}{\delta \rho_i\left(\boldsymbol{r}\right)}, \tag{2.16}$$

and the attractive (dispersion) part is treat via MFA:

$$U_i^{\mathrm{ff}}(\boldsymbol{r}) = \sum_{j=1}^{m} \int_{R_{\mathrm{min}}^{\mathrm{ff}}}^{R_{\mathrm{cut}}^{\mathrm{ff}}} \rho_j(\boldsymbol{r}') u_{ij}^{\mathrm{ff}}(r) d\boldsymbol{r}', \tag{2.17}$$

where $R_{\mathrm{min}}^{\mathrm{ff}}$ and $R_{\mathrm{cut}}^{\mathrm{ff}}$ are the inner and outer cut-offs for the dispersion part of the pair potential, respectively.

2.2 Results

To demonstrate the EQT approach, we consider a binary mixture of methane and hydrogen molecules confined in graphene slit channels with varying bulk compositions (see Fig. 2.2). The bulk compositions considered in this study are 30:70 and 70:30 CH_4/H_2 – the first is a hydrogen-rich bulk reservoir ($\mathrm{x}_m = 0.3$) and the second is a methane-rich mixture ($\mathrm{x}_m = 0.7$) with total bulk density of 17.73 atoms/nm^3. Methane and hydrogen molecules along with graphene carbon atoms are modelled as spherical LJ particles, interacting via standard 12-6 LJ potential,

$$u(r) = \frac{C_{12}}{r^{12}} - \frac{C_6}{r^6}, \tag{2.18}$$

where C_{12} and C_6, are the usual LJ parameters to be specified for each interaction. Table 2.1 summarizes the LJ parameters used in the MD simulations [64]. MD simulations are performed in canonical ensemble (NVT) using GROMACS [65] software. A cut-off of 1.524 nm(=$4\sigma_m$, where σ_m is the length-scale parameter for LJ interaction between methane molecules) is used for all the interactions. To maintain the temperature at 300 K, Nosé-Hoover thermostat [66] is used with a time constant of 0.2 ps. All systems are equilibrated for 2 ns, following a production run of 8 ns with 1 fs time step.

Table 2.1: LJ interaction parameters for methane (CH4) and Hydrogen (H2) molecules and graphene carbon (C) atom pairs.

	C_{12} (kJ/mol)	C_6 (kJ/mol)	σ (nm)
C-C	0.22222E-05	0.14385E-02	0.34000
C-H2	0.10652E-05	0.10749E-02	0.31575
C-CH4	0.10318E-04	0.47009E-02	0.36050
H2-H2	0.47563E-06	0.77525E-03	0.29150
H2-CH4	0.52117E-05	0.36058E-02	0.33625
CH4-CH4	0.46085E-04	0.15066E-01	0.38100

Nano-channels considered in this study, consist of two graphene layers extended in the $x - y$ plane and separated by a distance H in the z-direction. The lateral dimensions of the sheets are 3.834×3.689 nm^2 and the channel width is varied from $2\sigma_m$ to $15\sigma_m$ with an increment of $0.25\sigma_m$. Periodic boundary condition is applied in all the directions with an extra vacuum of $20\sigma_m$ in the z direction (perpendicular to the graphene layers) to avoid slab-slab interactions between periodic images. During the simulation, carbon atoms are kept frozen, i.e., their positions are not updated; thus, thermal vibrations of graphene layers are suppressed.

Linear superposition approximation (LSA) [67] method is adopted to estimate the number of molecules inside the channels of width larger than 1.524 nm ($=4\sigma_m$). It has been shown that LSA results in constant chemical potential except at very small separations (about two molecular diameters) [68]. Hence, for pores smaller than $=4\sigma_m$, the number of molecules obtained from NVT simulation of slit channels in contact with bulk mixture [69].

In the EQT simulations, for fluid-fluid and wall-fluid Lennard-Jones potentials the same interaction parameters as in MD simulations are used. Modeling correlation-correction potential using B-splines (Eq. 2.13) gives flexibility to the correction function and provides a numerically robust way of obtaining accurate density profiles. The B-splines knot values for the correlation-correction potentials are optimized based on the potential of mean force (PMF) matching technique [34], in which the mean-square error in density is minimized such that it reproduces the target potential of mean force within the specified tolerance. In PMF matching, for a slit-like system, where the fluid inhomogeneity is in one direction (z), optimization function for each fluid component is defined as,

$$\epsilon_i = \frac{1}{2H} \int_0^H \left(\rho_{i,b} \exp\left(-\frac{\bar{U}_i(z)}{k_{\mathrm{B}}T} \right) - \rho_i^{\mathrm{tgt}}(z) \right)^2 dz \tag{2.19}$$

where ρ_i^{tgt} is the target density of component i, obtained from the reference all-atom MD simulations and $\bar{U}_i(z)$ is defined as

$$\bar{U}_i(z) = U_i^{\mathrm{wf}}(z) + U_i^{\mathrm{ff}}(z) - U_{i,b}^{\mathrm{ff}}(z) \tag{2.20}$$

To obtain the optimal knot values in correction-correlation function, Eq. 2.19 is minimized using the Newton-Raphson optimization technique. Further details on PMF matching technique and Newton-Raphson optimization procedure can be found in [34]. There is no limitation to EQT in terms of system complexity. It has been shown that, EQT can also capture density variation of polar molecules such as water in nanoconfined channels [34]. In fact, EQT framework provides a tool to use particle-based coarse-grained potentials for which the electrostatic effects are already embedded.

In this work, we used the correlation correction potential approach. We optimize methane-methane, methane-hydrogen, hydrogen-hydrogen, and hydrogen-methane correlation-correction potentials for each bulk mixture composition. For each bulk mixture composition, PMF-matching-based optimization is performed using the methane and hydrogen density profiles in 6.34 nm channel, which are obtained from the reference MD simulations. We choose 6.34 nm channel for optimization because it is large enough that the layered structure and bulk region are well formed for both hydrogen and methane. Fig. 2.5 shows the optimized $\left(u_{ccp}^{\mathrm{ff}}\right)^*$ for different fluid-fluid interactions. Although, correlation-correction potentials are optimized for a reference channel of 6.34 nm width, we find that they are transferable across different pores at the same thermodynamic state.

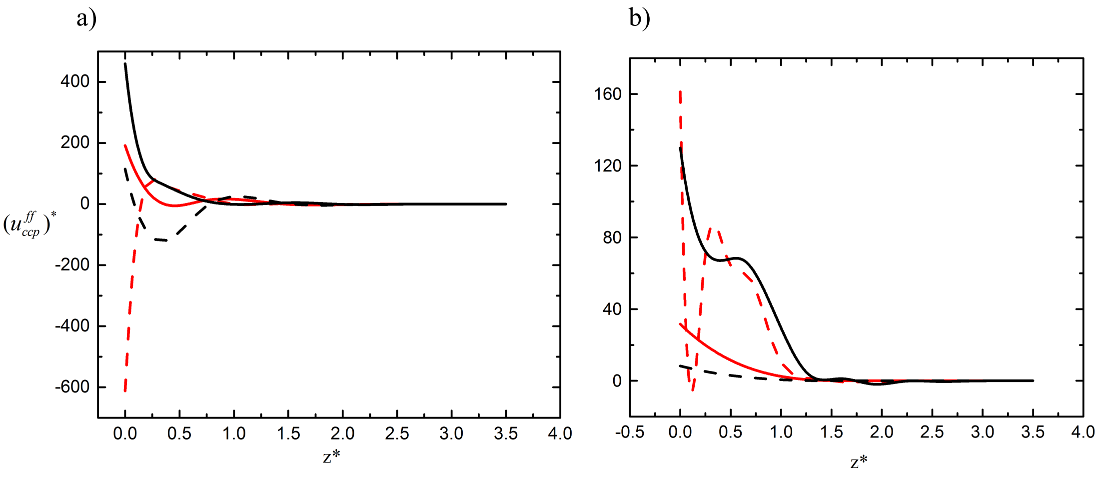

Figure 2.5: Correlation-correction potentials for x_m= 0.3 (a) and x_m= 0.7 (b) bulk compositions. Solid lines represent same component interactions: $CH_4 - CH_4$ (black), $H_2 - H_2$ (red); Dashed lines stand for cross interactions: $CH_4 - H_2$ (black), $H_2 - CH_4$ (red). The distance between walls, and correlation-correction potentials are made dimensionless based on hydrogen LJ parameters (σ_H, ϵ_H) and represented by $z^* = z/\sigma_H$, and $\left(u_{ccp,ij}^{\mathrm{ff}}\right)^* = u_{ccp,ij}^{\mathrm{ff}}/\epsilon_H$, respectively.

Fig. 2.6 depict that the density profiles from the quasi-continuum framework agree well with the MD simulations. In all cases, the EQT predictions are almost as accurate as MD. Both methane and hydrogen molecules arrange in layers and exhibit an oscillatory structural behavior due to the interplay of wall-fluid and fluid-fluid interactions. Well-formed layered structure and a plateau bulk region are observed for both hydrogen and methane in 6.34 nm channel, which is the largest channel considered in this study (see Figs. 2.6(a) and 2.6(d)). Layering is enhanced as the bulk composition increases from 0.3 to 0.7 (see Figs. 2.6(d-f) and 2.6(a-c)). This fact is more evident by comparing number of distinct density layers for methane and hydrogen in slits of width 3.21nm. For a bulk composition of 0.3, the number of distinct layers for methane and hydrogen is 6 (see Fig. 2.6(e)) whereas for a bulk mixture of 0.7, methane and hydrogen molecules are arranged in 8 layers (see Fig. 2.6(b)). Thus, increasing methane mole fraction enhances the structural order for both methane and hydrogen. Finally, by comparing the magnitude of the first peak for methane and hydrogen densities, it is evident that methane molecules are more concentrated in the vicinity of the wall. We have also tested the accuracy of the EQT at lower temperatures of 200 K and 250 K. We found that the density profiles from EQT approach are in good agreement with MD simulations.

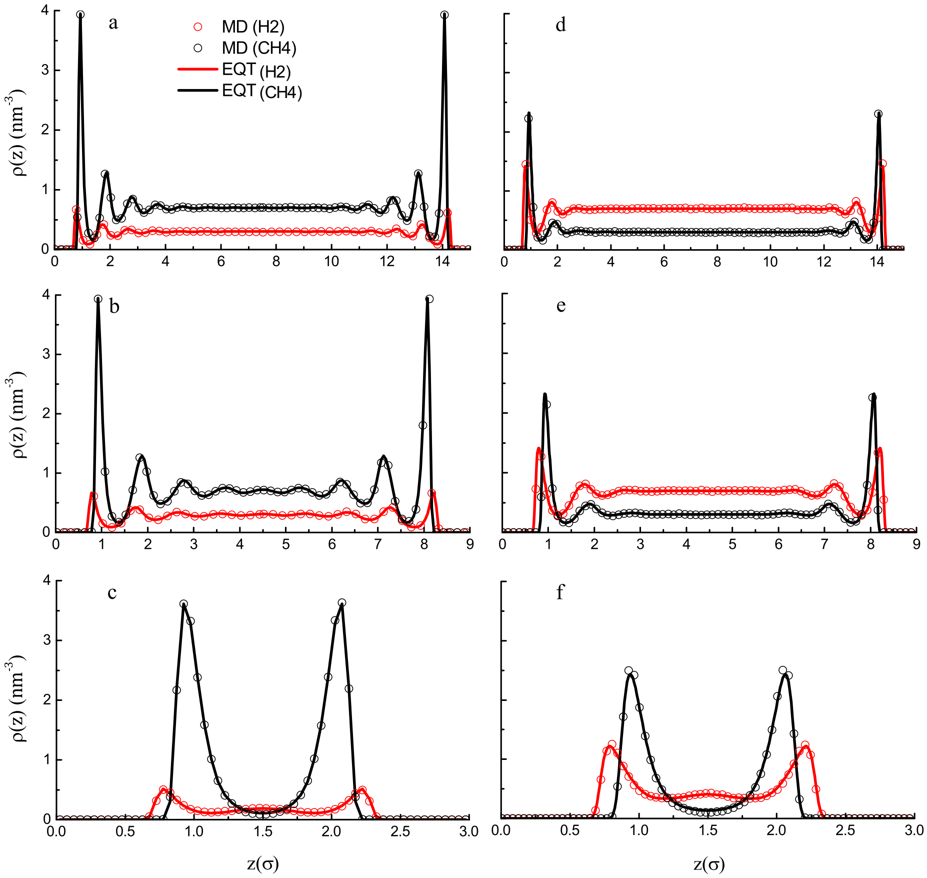

Figure 2.6: Comparison of density profiles of methane and hydrogen from EQT and MD simulations for different channel widths in equilibrium with hydrogen-rich (a-c) and methane-rich (d-f) bulk mixtures.

The essential new feature for mixtures is the change in composition due to confinement. Depending on the width, structure and material, nanopore may become selective towards a certain fluid component in the mixture. For a binary system, the selectivity (S) is often expressed as [24, 70–72]

$$S = \frac{x_{i,p}/\left(1 - x_{i,p}\right)}{x_{i,b}/\left(1 - x_{i,b}\right)} \tag{2.21}$$

where $x_{i,p}$ and $x_{i,b}$ represent the mole fraction of fluid component i in the pore and the coexisting bulk phase, respectively. For a slit channel of width H, the average mole fraction for a fluid component i inside the pore can be calculated from the following equation:

$$x_{i,p} = \frac{\int_0^H \rho_i(z)dz}{\sum_{i=1}^{2} \int_0^H \rho_i(z)dz} \tag{2.22}$$

Fig. 2.7 shows the selectivity of methane relative to hydrogen at T= 300 K as a function of pore width, for channels in equilibrium with the hydrogen-rich bulk reservoir ($x_m = 0.3$). It can be seen that the agreement between the MD and EQT results is good. In Fig. 2.7, S values greater than unity represent that the channel is completely selective toward methane. It can be seen that methane shows a higher adsorption affinity than hydrogen, especially in the smaller pores. This is due to the larger interaction energy between methane and graphene than hydrogen. The same line of reasoning has also been used in other literature [73, 74] in which they have shown that the molar fraction of the component having the strongest interaction with the channel is increased compared to the bulk.

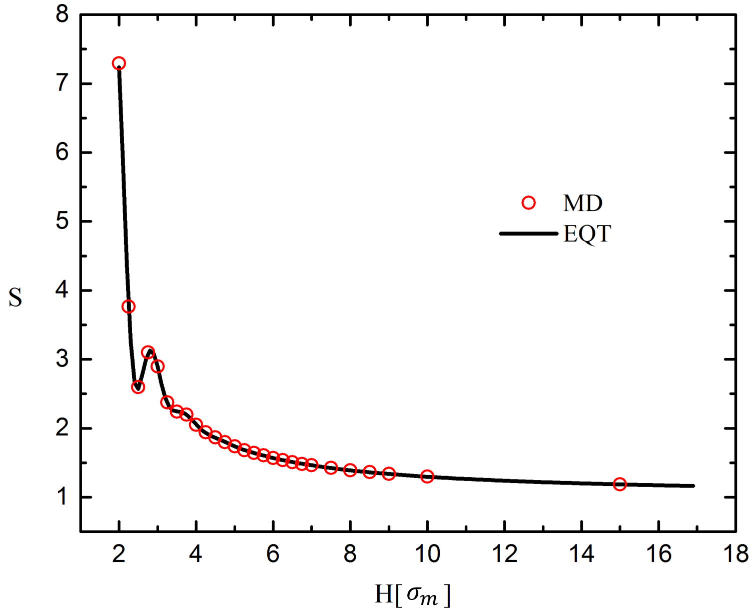

Figure 2.7: Selectivity of methane over hydrogen as a function of channel width.

2.3 Summary

In this chapter, we presented the EQT approach and compared it to the atomistic MD simulations. EQT is a practical, fast and easy approach to bridge the gap between atomistic and continuum methods by constructing potentials from atomistic interactions. Using correlation correction approach, we approximate the fluid-fluid correlations by the bulk hard-sphere radial distribution function (RDF) and add correlation correction potentials. These potentials can be used in a continuum framework such as the Nernst-Planck equation. We demonstrated the EQT for mixtures by predicting density distributions of methane and hydrogen mixtures confined in graphitic nanopores of various widths. We considered two extreme cases, where channels are in equilibrium with methane-rich and hydrogen-rich bulk mixtures. In both cases, theoretical results compare well with the MD simulations. We also used EQT results to calculate adsorption selectivity of the mixture rich in hydrogen. It is found that, though the bulk composition favors hydrogen, graphene slit channels exhibit selectivity for methane molecule. This finding can be attributed to the larger energy interaction of methane and graphene wall. EQT is a promising multiscale framework that can accurately predict structure of not only single component but also the mixture of confined fluids.

Chapter 3

An EQT-cDFT approach for thermodynamic properties of confined fluid mixtures

In this chapter, we integrate EQT frame work with classical density functional theory (cDFT), i.e., EQT-cDFT approach, in order to determine thermodynamic properties of confined fluids. The combination of EQT and cDFT provides a simple and fast approach that not only predicts the equilibrium structure, but also other thermodynamic properties, such as the local pressure profile, adsorption, solvation force, surface tension, etc. [36].

The relevant thermodynamic potential for an open system that is in equilibrium with a bulk phase (i.e., the system can exchange heat and particle with the bulk phase) is the grand potential, Ω.

$$\Omega = -P\mathrm{d}V - S\mathrm{d}T - \sum_{i=1}^{m} N_i \mathrm{d}\mu_i, \tag{3.1}$$

where S is the entropy, T is the temperature, P is the pressure, V is the volume, N_i is the number of the fluid particles of component i, μ_i is the chemical potential of the fluid particles of component i. When a fluid is narrowly confined between to parallel plates of area A, additional control variables comes into play. These new variables are the surface area of the plates, A and the spacing between them, H. Thus, for a fluid mixture confined between two flat surfaces of area A, the change in grand potential caused by an infinitesimal change of thermodynamic state is given by,

$$\mathrm{d}\Omega = -S\mathrm{d}T - P\mathrm{d}V - \sum_{i=1}^{m} N_i \mathrm{d}\mu_i + 2\gamma \mathrm{d}A - f_{\mathrm{S}} A \mathrm{d}H, \tag{3.2}$$

where γ is the wall-fluid surface tension, and f_{S} is the solvation force. Knowing the grand potential, we can obtain any thermodynamic property by taking the appropriate derivatives of Ω according to Eq. 3.2. For this purpose we are going to use the cDFT theory which gives an expression for the grand potential as a function of the confined fluid density.

3.1 cDFT

cDFT is a continuum-based technique that describes the properties of inhomogeneous fluids from a microscopic level. It is based on the theorem that, for a fluid in an external field, the Helmholtz free energy, F, is a unique functional of the average molecular density profile, $\rho(\mathbf{r})$, independent of the external potential, $V_{\text{ext}}(\mathbf{r})$ [47, 75, 76]. Thus, Ω can be written as

$$\Omega\left[\{\rho_i(\mathbf{r})\}\right] = F\left[\{\rho_i(\mathbf{r})\}\right] + \sum_{i=1}^{m} \int \left(V_i^{\text{ext}}(\mathbf{r}) - \mu_i\right) \rho_i(\mathbf{r}) d\mathbf{r}, \tag{3.3}$$

where F denotes the intrinsic Helmholtz free energy and V_i^{ext} is the external potential acting on fluid component i. The Helmholtz free energy has contributions from ideal and excess part:

$$F\left[\{\rho_i(\mathbf{r})\}\right] = F^{\text{id}}\left[\{\rho_i(\mathbf{r})\}\right] + F^{\text{ex}}\left[\{\rho_i(\mathbf{r})\}\right], \tag{3.4}$$

where the ideal part is exactly known, and it is given by

$$F^{\text{id}}\left[\{\rho_i(\mathbf{r})\}\right] = k_{\text{B}}T \sum_{i=1}^{m} \int \rho_i(\mathbf{r}) \left(\ln\left(\rho_i(\mathbf{r})\Lambda_i^3\right) - 1\right) d\mathbf{r}, \tag{3.5}$$

where k_{B} is the Boltzmann constant, $\Lambda_i = \left(\frac{2\pi\hbar^2}{m_i k_{\text{B}} T}\right)^{\frac{1}{2}}$ is the thermal de-Broglie wavelength, $\hbar$ is the reduced Planck's constant, and m_i is the mass of the i^{th} atom. Unlike the ideal part, the excess part of the Helmholtz free energy accounts for non-ideality due to the existing inter-molecular interactions. The treatment of this part is rather intractable, since it contains the information about correlations between the particles [13, 77, 78]. Thus far, the exact expression for F^{ex} is unknown and dealing with this part of the Helmholtz free energy is the most challenging task in the cDFT. There are approaches that provide functional forms for F^{ex} based on the fundamental-measure theory (FMT) [62, 63], modified FMT (MFMT) [79, 80], first-order mean-spherical approximation (FMSA) [81], accurate empirical equation of state [82], and statistical associating fluid theory (SAFT) [53, 83–86]. In this work, we use EQT to formulate F^{ex} as explained in Section 3.2.

3.2 EQT-cDFT

In the EQT-cDFT approach, the fluid-fluid EQT potential model (Eq. 2.12) is used to construct the excess part of the intrinsic Helmholtz energy functional:

$$F^{\mathrm{ex,EQT}}\left[\{\rho_i(\mathbf{r})\}\right] = \frac{1}{2}\sum_{i=1}^{m}\int \rho_i(\mathbf{r}')U_i^{\mathrm{ff}}(\mathbf{r}')d\mathbf{r}'. \tag{3.6}$$

Due to the chemical equilibrium condition between a confined fluid system and a bulk reservoir, the chemical potential of each fluid component in Eq. 3.3 is same as fluid components of the homogeneous phase, i.e, $\mu_i = \mu_{i,\mathrm{b}}$. Furthermore, we can split the bulk chemical potential into the ideal and the excess part, i.e,

$$\mu_{i,\mathrm{b}} = \mu_{i,\mathrm{b}}^{\mathrm{id}} + \mu_{i,\mathrm{b}}^{\mathrm{ex}}, \tag{3.7}$$

where the ideal part can be written as,

$$\mu_{i,\mathrm{b}}^{\mathrm{id}} = k_{\mathrm{B}}T\ln\left(\rho_{i,\mathrm{b}}\Lambda_i^3\right). \tag{3.8}$$

From the definition of the chemical potential, $\mu_{i,\mathrm{b}}^{\mathrm{ex}} = \left(\frac{\partial F_{\mathrm{b}}^{\mathrm{ex}}}{\partial \rho_{i,\mathrm{b}}}\right)_T$, and applying Eq. 3.6 in the bulk phase, it is easy to show that the excess part of the bulk chemical potential is equal to the EQT bulk fluid-fluid potential, U_{b}, i.e.,

$$\mu_{i,\mathrm{b}}^{\mathrm{ex}} = U_{i,\mathrm{b}}, \tag{3.9}$$

where $U_{i,\mathrm{b}}$ is obtained by applying Eq. 2.12 in the bulk phase:

$$U_{i,\mathrm{b}} = 4\pi\sum_{j=1}^{m}\rho_{j,\mathrm{b}}\int_0^{R_{\mathrm{cut}}^{\mathrm{ff}}} r^2\left(u_{ij}^{\mathrm{ff}}(r)g_{ij}^{\mathrm{hs}}(r) + u_{\mathrm{ccp},ij}^{\mathrm{ff}}(r)\right)dr. \tag{3.10}$$

For the slit-channel geometry the only external potential acting on the fluid mixture is the wall-fluid interaction, i.e, $V_i^{\mathrm{ext}}(\mathbf{r}) = U_i^{\mathrm{wf}}(\mathbf{r})$. Hence, using Eqs. 3.3-3.9, the grand potential in the EQT-cDFT formalism can be written as,

$$\begin{aligned}\Omega^{\mathrm{EQT}}\left[\{\rho_i(\mathbf{r})\}\right] = \sum_{i=1}^{m}\Bigg(& k_{\mathrm{B}}T\int\rho_i(\mathbf{r})\left[\ln\frac{\rho_i(\mathbf{r})}{\rho_{i,\mathrm{b}}} - 1\right]d\mathbf{r} \\ & +\frac{1}{2}\int\rho_i(\mathbf{r})U_i^{\mathrm{ff}}(\mathbf{r})d\mathbf{r} \\ & +\int\rho_i(\mathbf{r})\left(U_i^{\mathrm{wf}}(\mathbf{r}) - U_{i,\mathrm{b}}\right)d\mathbf{r}\Bigg).\end{aligned} \tag{3.11}$$

At equilibrium, the grand potential is minimum with respect to the density distributions; thus, from the variational principle given as,

$$\left.\frac{\partial\Omega^{\mathrm{EQT}}\left[\{\rho_i(\mathbf{r})\}\right]}{\partial\rho_i}\right|_{eq} = 0, \tag{3.12}$$

the equilibrium density profile of each species satisfies

$$\rho_i(\mathbf{r}) = \rho_{i,\mathrm{b}} \exp\left(-\frac{1}{k_{\mathrm{B}}T}\left(U_i^{\mathrm{ff}}(\mathbf{r}) + U_i^{\mathrm{wf}}(\mathbf{r}) - U_{i,\mathrm{b}}\right)\right). \tag{3.13}$$

Using an iterative method such as Picard iteration, Eq. 3.13, Eq. 2.12 and Eq. 2.5 can be solved self-consistently to obtain the equilibrium density profiles of the confined fluid mixture.

3.3 Thermodynamic properties

As mentioned in Section 2.2, the inhomogenous fluid mixture we consider in this study, is confined in slit pores made up of two graphene sheets infinitely long in the xy plane, located at $z = 0$ and $z = H$. Due to the planar geometry, we will assume that all the mean quantities vary only in the z direction. In this work, we compute thermodynamic quantities such as average densities, local pressure tensor, surface tension, and solvation force for different bulk mixture compositions.

Studying the local pressure tensor profiles in an inhomogenous fluid system is important from both industrial and scientific point of view. For homogeneous fluids, the pressure tensor is isotropic (i.e, $P_{\mathrm{xx}} = P_{\mathrm{yy}} = P_{\mathrm{zz}}$), whereas in a confined fluid, it is anisotropic and varies spatially. For slit channels, due to the symmetry in the lateral dimensions, the off-diagonal terms in the local pressure tensor are zero, and the relevant quantities are the normal, $P_{\mathrm{n}}(z)$, and lateral, $P_l(z)$, pressure profiles. Moreover, the condition of mechanical equilibrium, requires that the normal pressure be constant across the channel [87], and be equal to the average force per unit area exerted by the fluid molecules on the wall.

To obtain P_{n}, one can use the central difference method to calculate the derivative of the grand potential with respect to the channel width [36]. This method is also analogous to the volume perturbation expressions proposed by de Miguel and Jackson [88] in the context of vapor-liquid interfaces. Alternatively, from the balance of the forces in the confined direction, the normal pressure can be calculated based on the average density and the wall-fluid potential [89], i.e,

$$P_{\mathrm{n}}(H) = -\sum_{i=1}^{m}\int_0^H \left(\rho_i(z)\frac{dU_i^{\mathrm{wf}}(z)}{dz}\right) dz. \tag{3.14}$$

Unlike the normal pressure, the lateral pressure is not constant across the channel and varies in the z

direction. For a planar system, it is possible to define the lateral pressure as the negative of the grand potential density, $\omega(z)$ [90–92]; thus from Eq. 3.11, P_l can be calculated as,

$$P_l(z) = -\sum_{i=1}^{m} \Bigg(k_{\mathrm{B}}T\rho_i(z)\left[\ln\frac{\rho_i(z)}{\rho_{i,\mathrm{b}}} - 1\right] + \frac{1}{2}\rho_i(z)U_i^{\mathrm{ff}}(z) + \rho_i(z)\left(U_i^{\mathrm{wf}}(z) - U_{i,\mathrm{b}}\right)\Bigg). \tag{3.15}$$

We can further simplify Eq. 3.15, by substituting the density profile from Eq. 3.13 and reformulate the lateral pressure in the EQT-cDFT framework as,

$$P_l(z) = \sum_{i=1}^{m}\left(k_{\mathrm{B}}T\rho_i(z) + \frac{1}{2}\rho_i(z)U_i^{\mathrm{ff}}(z)\right). \tag{3.16}$$

The surface tension, γ, can be calculated using the thermodynamic or the mechanical route. The thermodynamic definition is based on the amount of isothermal work required to increase the interface by unit area, i.e., $\gamma = \frac{1}{2}\left(\frac{\partial\Omega}{\partial A}\right)_{T,\mu,L}$ for a slit-channel system. According to the mechanical definition, for planar systems, the surface tension can be calculated based on the integral difference of the tangential and normal components of the pressure tensor profiles along the confined direction [90, 93], i.e.,

$$\gamma(H) = \frac{1}{2}\int_0^H \left(P_{\mathrm{n}} - P_l(z)\right) dz. \tag{3.17}$$

Finally, the quantity f_{S}, which is commonly referred to as solvation force, is actually the average force per unit area exerted by the fluid molecules normal to the surface [94]. Hence, the solvation force has a unit of pressure and can be calculated as,

$$f_{\mathrm{S}}(H) = P_{\mathrm{n}}(H) - P_{\mathrm{b}}, \tag{3.18}$$

where P_{b} is the fluid mixture bulk pressure.

3.4 Results

One of the advantages of the EQT-cDFT approach over the Nernst-Planck approach (Eq. 2.1), is that a solution of the EQT-cDFT approach does not require ρ_{avg} as an input; instead, ρ_{avg} can be computed as an output of the EQT-cDFT simulation from the equilibrium density profile. The average density of each species inside the channel can be obtained from the EQT-cDFT approach

$$\rho_{i,\mathrm{avg}} = \frac{N_i}{A \times H}, \tag{3.19}$$

The average densities for methane and hydrogen molecules in various size channels are given in Table 3.1.

Table 3.1: Average fluid densities (nm^{-3}) in MD simulations of various size channels for different bulk molar compositions.

ρ_{avg}	$15\sigma_m$	$10\sigma_m$	$9\sigma_m$	$8\sigma_m$	$7\sigma_m$	$6\sigma_m$	$5\sigma_m$	$4\sigma_m$	$3\sigma_m$	$2\sigma_m$
H2($x_m = 0.3$)	11.02	10.33	10.10	9.81	9.46	8.97	8.27	7.24	5.38	2.23
H2($x_m = 0.7$)	4.72	4.42	4.33	4.20	4.03	3.83	3.52	3.01	2.10	0.74
CH4($x_m = 0.3$)	5.60	5.75	5.79	5.84	5.94	6.03	6.16	6.35	6.68	6.96
CH4($x_m = 0.7$)	11.86	11.60	11.50	11.39	11.24	11.04	10.76	10.34	9.65	8.07

To calculate the MD local stress tensor, we use GROMACS-LS code by Vanegas et al. [95], which is based on Hardy-Mudroch procedure. As mentioned in Section 3.3, due to the mechanical equilibrium, P_n is constant across the nanopore. Therefore, for a large enough channel (e.g. $15\sigma_m$) with a well-formed bulk region in the middle, P_n should be equal to the mixture bulk pressure. We use this fact to verify the GROMACS-LS code for our simulation purposes. We observe that the normal pressure obtained from the code is constant along z direction and it is equal to the mixture normal pressure calculated from the total force perpendicular to the wall [96],

$$P_n = \frac{|\sum_{i=1}^{N_f} F_{z,i}^{wf}|}{A}, \tag{3.20}$$

where N_f is the total number of fluid molecules (hydrogen and methane) and $F_{z,i}^{wf}$ is the z component of the force produced by molecule i on the wall. Other thermodynamic properties such as surface tension and solvation force can be calculated from Eqs. 3.17 and 3.18 using the values in the local pressure tensor.

Fig. 3.1 shows the variation of the average density of each species with the channel width and the bulk composition. For channels in equilibrium with the methane-rich bulk mixture, both methane and hydrogen average densities monotonically decrease (slight undulations) until $H = 6\sigma_m$. As the channel width further decreases, we observe noticeable undulations in the average densities versus H. These oscillations in ρ_{avg} for smaller channels follow the formation of adsorbed layers with increasing H. A similar trend has been observed for hydrogen average density for channels in equilibrium with the hydrogen-rich bulk mixture. However, the onset of undulations has been observed for $4\sigma_m$ channel width. Moreover, unlike the x$_m = 0.7$ case, the methane average density in the channel is higher than its bulk density and grows monotonically until $H = 4\sigma_m$. For the $15\sigma_m$ channel, the hydrogen average density is higher than that of methane. As the channel width gets smaller, hydrogen molecules get depleted from the channel and are replaced by methane molecules. This trend continues, until the number of methane molecules surpasses the hydrogen molecules in the channel of $3.25\sigma_m$ width. Further decrease in the channel width, results in adsorption of more methane molecules in comparison to hydrogen, despite the fact that the bulk mixture is rich in hydrogen content. Therefore, we can clearly see how graphene is selective towards methane. In fact, the origin of this behavior is rooted in the higher interaction energy between carbon-methane compared to carbon-hydrogen.

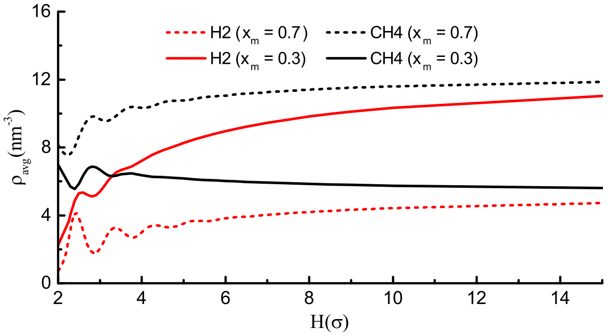

Figure 3.1: EQT-cDFT predictions for average densities of methane and hydrogen molecules as a function of channel width.

Fig. 3.2 shows the variation of the lateral pressure tensor profiles in the channels corresponding to the methane and hydrogen-rich bulk mixtures. It can be seen that the EQT-cDFT predictions are in good agreement with the MD simulations. As it is evident from Eq. 3.16, due to the layering in the density profiles, an oscillatory behavior is also observed in the lateral pressure profiles. We observe that in confinement, the lateral pressure is significantly enhanced compared to its bulk value. This effect is more pronounced in the vicinity of the walls, where the value of the pressure is approximately 5 times higher than bulk value for $15\sigma_m$ channel (see Fig. 3.2b). Such high values of pressure can enhance chemical reactions, and give rise to high pressure solid phases in nanoconfinements [6, 97–100].

From Figs. 3.2 and 2.6, we observe that the high lateral pressure regions correspond to the locations where the methane density profile exhibits peaks. Eventhough hydrogen molecules also contribute to the pressure, due to their smaller diameter and interaction energy compared to methane, the lateral pressure profiles follow closely the methane density profiles, irrespective of the bulk mixture composition. This fact is more evident as the channel width gets smaller. The higher adsorption affinity of methane in the narrower channels makes it the dominant contributor to lateral pressure in these channels.

By comparing Figs. 3.2(a) and 3.2(b), we find that the channels in equilibrium with methane-rich bulk mixture exhibit higher pressure. In addition, by looking at the $15\sigma_m$ channels, it is clear that by increasing

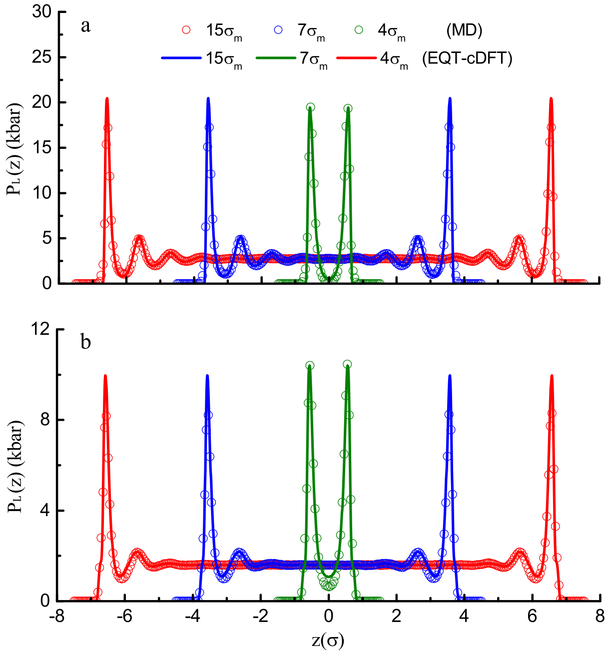

Figure 3.2: Comparison of lateral pressure profiles of methane-rich mixture (a) and hydrogen-rich mixture (b) from EQT-cDFT and MD simulations for various channel widths.

the methane content of the bulk, the oscillations in the lateral pressure profile become more pronounced and decay slower than the hydrogen-rich bulk mixture to the bulk value. The origin of this behavior lies in the tendency of graphene for attracting methane molecules over hydrogen, and the ordering enhancement caused by the methane molecules (compare Figs. 2.6(b) and 2.6(e)) in confinement.

In Fig. 3.3, we show the variation of the normal pressure, solvation force and surface tension as a function of the channel width for both methane and hydrogen-rich bulk mixtures. We observe that the theoretical predictions by EQT-cDFT approach compare well with MD simulations. As mentioned in Section 3.3, due to the mechanical equilibrium, for a slit channel, normal pressure is constant across the channel width (i.e. independent of z). However, it shows an oscillatory behavior as a function of the channel width. These oscillations are well-known and relate to the number of adsorbate layers, the interlayer spacing [101], and the behavior of the average density [97, 102], which depends on the channel width. As a corollary, solvation force and surface tension also exhibit an oscillatory behavior with decaying amplitude as the channel width gets larger. For larger channels, the wall effects become weaker and hence P_n converges to the bulk value, and f_s and γ approach zero.

To investigate the effect of mixture composition and its constituents, we focus our attention on Figs. 3.3(a)-

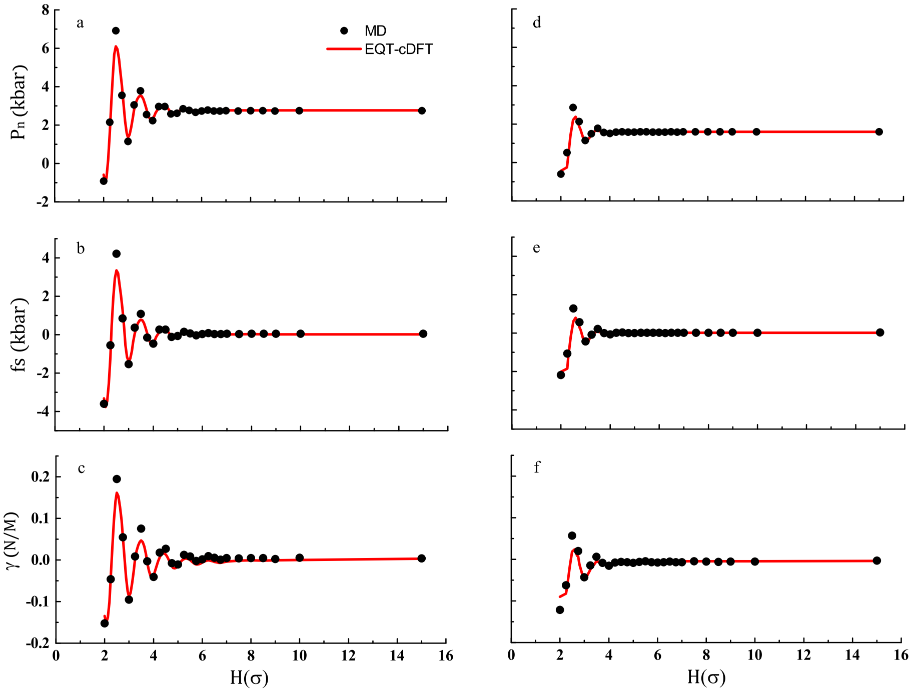

Figure 3.3: Variation of normal pressure (P_n), solvation force (f_s) and surface tension (γ) with channel width corresponding to the methane-rich (a-c) and hydrogen-rich (d-f) bulk mixture compositions.

3.3(c) and 3.3(d)-3.3(f). It can be seen that for $\mathrm{x}_m = 0.7$ bulk composition, the maximum value of the normal pressure is about 3 times higher than that of for channels in equilibrium with $\mathrm{x}_m = 0.3$ bulk mixture. Moreover, we observe that the oscillations in the f_s (Fig. 3.3(e)) disappear at $4.25\sigma_m$ for $\mathrm{x}_m = 0.3$, whereas for the channels in equilibrium with methane-rich bulk mixture, the oscillations persist until $6.6\sigma_m$. Again, this confirms the observations that for the channels in equilibrium with methane-rich mixture, the extent of oscillatory behavior observed in thermodynamic properties is larger compared to the bulk composition of $\mathrm{x}_m = 0.3$.

3.5 Summary

In this chapter, we showed that using the EQT-based potentials, we can construct an expression for the excess free energy functional in the cDFT frame work to obtain various thermodynamic properties, such as density, local pressure tensor, solvation force and surface tension. We demonstrated the EQT-cDFT approach for a binary mixture of methane and hydrogen molecules confined in slit nano channels of various widths and two different bulk compositions. We found that our theoretical predictions compare well with the MD simulations, showing that the EQT-cDFT is a promising approach to obtain thermodynamic properties of confined fluid mixtures.

Chapter 4

Multiscale dipolar model for confined polar liquids

In this chapter we introduce a multiscale investigation of water inside graphene slitlike channels that extends from the detailed all-atom level (AA) to the cheaper particle-based coarse-grained (CG) level, and to the continuum-based level using EQT. Since water is a highly polar solvent, the detailed description of its structural and dielectric properties close to the interfaces is of paramount importance in many applications. For this purpose, we will systematically develop an extended dipole-based CG model that can accurately reproduce the radial distribution function (RDF), diffusion coefficient, and bulk dielectric permittivity of the underlying AA reference model. The CG representation model is simple yet complex enough to shed light on the role of dipolar interactions in polar liquids such as water. Using the CG potentials, we will asses the structure, parallel dielectric permittivity, and polarization profiles compared to all-atom molecular dynamics simulations. Furthermore, we show that EQT framework can also be used for complex molecules such as water to predict the density and polarization of water molecules inside nanoslit channels of various widths. Finally, by using coarse-grained molecular dynamics and EQT simulations, we comment on the applicability of dipolar-based CG models in reproducing the structure of water near charged interfaces.

4.1 Water coarse grain models

Water is one of the most abundant molecules on the Earth. Even though it is a chemically “simple” molecule, water has posed a great challenge to the scientific community in terms of describing its behavior at interfaces and in aqueous solutions. Due to its geometry and distinct charge distribution, water is a highly polar molecule with a relatively high dielectric constant. The dielectric permittivity is directly related to the ability of the fluid in screening charges. Thus, the electrostatic interactions of water in the presence of an external field or with charged objects such as charged colloidal particles, ions, proteins, and lipid membranes are profoundly affected by its very existence [103, 104]. Thus, an in-depth understanding of these interactions and accurate representation of water screening effects are essential to many applications such as water desalination [105, 106], protein folding [107, 108], peptides self-assembly [109], double-layer capacitance [110], and electrochemical applications of ionic liquids [111].

Due to its computational cost, many theoretical models treat water as a background solvent with a constant dielectric permittivity [30, 112–114]. Although it is true in the case of bulk water, near interfaces the dielectric permittivity varies significantly. Therefore, considering a uniform permittivity may not accurately reflect the underlying physics of charge screening. In fact, capturing the anisotropic nature of dielectric variations, which are reminiscent of the well-known spatially varying density oscillations at an interface, is of paramount importance to many biological and industrial applications [115, 116].

Over the past years, density functional theory (DFT) and high resolution atomistic simulations such as, molecular dynamics and Monte Carlo simulations have been adopted to study water for a variety of applications in biology, physics and material science. From these methods one can obtain molecular insights into the nature of different interactions and interpret the physical phenomena based on the knowledge of statistical mechanics. However, for many practical systems the number of water molecules is of the order of several thousands to millions [29], making these methods forbiddingly expensive to simulate systems involving multiple length and time scales ranging from the quantum to atomic to continuum scales. Thus, developing multiscale methods that are accurate, fast and rooted in statistical mechanics can be of high value.

In order to reduce the computational cost, CGMD simulations can be used to access larger length and time scales. The objective of any CG simulation is to lower the resolution by representing the system with fewer degrees of freedom, while retaining the necessary details to capture the quantity of interest. For any polar molecule, the dipole-dipole interactions and fluctuations are mainly responsible for the dielectric response of the fluid. These interactions are ubiquitous in nature, and they exist in many systems, such as colloids, ferro and electro-rheological fluids [117]. Moreover, in addition to the spherically symmetric short-range interactions, dipolar molecules bring in anisotropic forces due to their long-range dipole-dipole interactions, and thus, can serve as a simple model to understand the structure, dynamics and thermodynamic properties of polar fluids or dipolar colloidal systems [117, 118].

Recently, there have been efforts to develop CG models that include and optimize charges/dipole moments to reproduce various properties of the reference system. The reason behind such efforts is two-fold. First, due to the existence of dipole fluctuations, one can calculate the dielectric constant of the fluid. Since the dielectric permittivity incorporates both short- and long-ranged correlations, it can serve as a good test for the accuracy of an inter-molecular potential [119]. On the other hand, the implicit treatment of electrostatic interactions for polar molecules, in particular water, fails to capture their dielectric screening effect [120]. One of the earliest studies is based on the well-known Stockmayer potential [121] (a single-site interaction with an associated orientation), which models water as a hard sphere with a point dipole and is referred to as Bratko, Blum, and Luzar (BBL) model [122]. A soft sticky dipole potential is also developed for liquid water, which is the same as the BBL model, except that the hard-sphere interaction is replaced by the softer Lennard-Jones potential [29]. More generally, the generalized Stockmayer (GSM) potential is developed for polar liquids that consists of a spherical Kernel with dipole-dipole interaction [123] and has been recently applied for water [124]. There are also efforts to match properties of water to experiments (top-down CG methods). One of the top-down CG approaches that maps water into a single-site CG bead with an embedded point dipole is the electrostatic based (ELBA) model. The model was originally developed for a lipid membrane. The parameters are tuned such that with a loss of local structure, it reproduces the bulk water density, and diffusion at room temperature in a good agreement with experiments [125, 126]. In a more systematic way, the force matching technique is used with the Drude-like model, to reproduce the radial distribution functions (RDFs) and the dielectric permittivity of some amines and alchohols such as methanol [127]. In this study, we systematically develop an extended dipole-based model for polar fluids that can accurately predict the radial distribution function (RDF), diffusion coefficient, and the bulk permittivity of the reference all-atom model. We apply our model to reproduce water RDF, diffusion coefficient, and dielectric permittivity in the bulk. For this purpose, we model water molecules into extended dipoles, and optimize the dipole moment within the relative entropy framework. However, as we show later in Section 4.6.1, the dipole optimization alone does not guarantee that the water dipolar properties, in particular the dielectric permittivity, are reproduced by the CG model. Thus, we employ the constrained relative entropy (CRE) method [128] to reproduce the all-atom bulk permittivity in the CG model.

The remainder of this chapter is organized as follows. In Section 4.2, we provide details on the extended dipole-based CG model and apply it to water molecules. In Section 4.3.1, we first describe the details of systematic charge optimization within the relative entropy frame work for dipole-based CG models and then in Section 4.3.2, we describe the CRE method in order to reproduce the bulk water permittivity of an all-atom reference model. In Section 4.3.3, we discuss how to match diffusion through modifying the inertia features of our model. In Section 4.3.4, we discuss systematic coarse-graining in inhomogenous environment by optimizing the wall-fluid interaction energy. In Section 4.4, we describe the theory of the EQT framework. In Section 4.5, we first provide the necessary details of the MD, CG, and EQT simulations. Second we provide the CG potentials obtained via charge and dielectric permittivity optimization. We then demonstrate the ability of our CG models in reproducing density and parallel permittivity profiles of water molecules inside neutral graphene channels of various widths. In addition, using the EQT framework, we investigate the applicability of the MFA for capturing the dipolar interactions inside the slit-like graphene channels.

4.2 Extended dipole model

In this study, we consider a CG model consisting of extended dipolar molecules [37, 129], in which two opposite charges, $\pm q$, are located at a distance d from each other, thereby creating a dipole moment of $\mu = qd$. The topology of the extended dipole molecule is shown in Fig. 4.1(a). It can be seen that the molecule has an effective diameter of σ and a van der Waals (vdW) interaction site that is located at the center, $d/2$ distance away from either of the charges. Thus, the interaction energy between the extended dipolar molecules consists of four Coulombic interactions due to the positive and negative charges, and a vdW pair potential between the molecules center. Compared to the point dipole spherical models, the extended dipole model provides a more realistic picture of highly polar fluids [129]. In addition, it has been shown that for $d/\sigma \leq 0.25$, the extended dipole and point dipole models are similar. In this study, we assumed that the distance d is fixed, so the CG model is not polarizable. Although the distance between the charges can be considered as an optimization parameter, for simplicity we only consider optimizing the charges on the molecule as well as the vDW interaction.

In order to optimize the charges and the vdW interaction, we follow a systematic bottom-up coarse-graining approach to reproduce the properties of the underlying all-atom reference model. To demonstrate our model, we coarse-grain the all-atom SPC/E water into the extended dipolar molecules with $d = 0.058\,\mathrm{nm}$, which represents the distance between the oxygen and the center of the line intersecting the hydrogen atoms in the SPC/E AA water model.

4.3 CG optimization

Our objective is to reproduce the RDF, diffusion coefficient, and the dielectric permittivity in the bulk CG system. There are various systematic CG methods such as iterative Boltzmann inversion (IBI) [130], inverse Monte-Carlo (IMC) [131], and relative entropy (RE) minimization [132, 133] that can accurately reproduce the AA target RDFs. When RDF is the only target of interest, the choice of center-of-mass (COM) mapping of atoms/molecules into spherical beads is a common choice. However, to reproduce the dielectric permittivity, one needs to take into account the dipolar fluctuations. So for a CG system to be able to predict the dielectric constant, dipole-dipole interactions have to be explicitly considered in the model.

Here, we use the RE framework to systematically optimize the vdW and electrostatic interactions between the extended dipolar molecules to reproduce the RDF and dielectric constant of the SPC/E water at the temperature of 298 K and density of 1.0 g/cm^3.

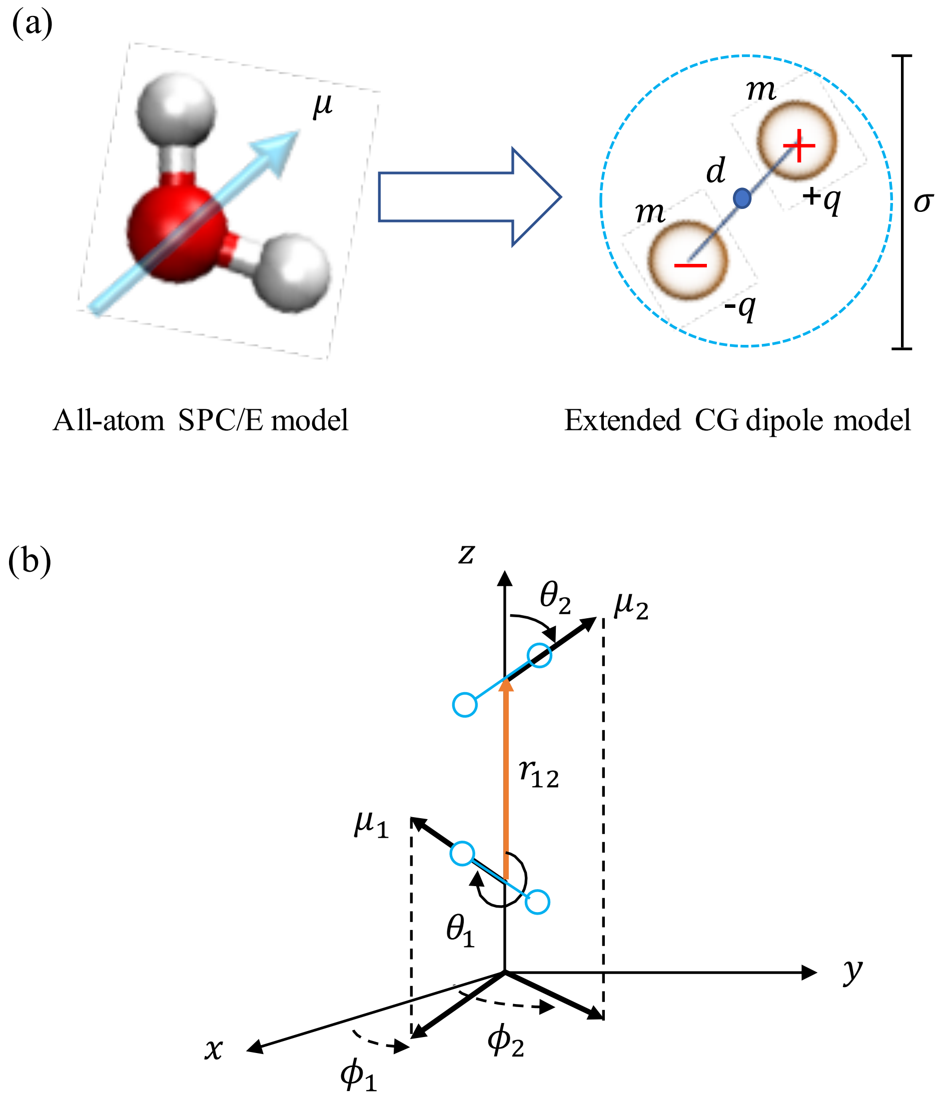

Figure 4.1: (a) Topology of the extended dipole water molecule. (b) Coordinate system: dipoles are denoted by their dipole vector μ and their corresponding angles, (θ, ϕ). r_{12} is the separation distance vector between dipoles μ_1 and μ_2.

4.3.1 Charge optimization

Relative entropy quantifies to what extent the configurational probability distributions vary from one another between the CG and AA model. Therefore, minimizing the relative entropy with respect to the potential parameters results in the CG energy landscape that reproduces as best as possible the underlying AA probability distribution function in the CG degrees of freedom. It has been shown that in the canonical ensemble the RE can be written as [132],

$$S_{rel} = \beta \left\langle U_{\mathrm{CG}} - U_{\mathrm{AA}} \right\rangle_{\mathrm{AA}} - \beta \left(F_{\mathrm{CG}} - F_{\mathrm{AA}} \right) + \left\langle S_{map} \right\rangle_{\mathrm{AA}} , \tag{4.1}$$

where U is the total energy, F is the configurational part of the Helmholtz free energy, $\langle \dots \rangle$ represents the Boltzmann weighted average in the corresponding ensemble, S_{map} is the mapping degeneracy in the AA model, and $\beta = 1/k_B T$ with k_B as the Boltzmann constant and T as the temperature. As mentioned earlier, the interaction energy for a system of the extended dipolar molecules consists of the vdW and Coulombic part. We assume that the total CG interaction energy is pairwise additive, and we model it as

$$U_{\mathrm{CG}} = \sum_{i=1}^{N} \sum_{j>i}^{N} u_{\mathrm{dd},CG} \left(r_{ij} \right) , \tag{4.2}$$

where the summations are over all the distinct dipole molecules, N is the number of dipolar molecules, r_{ij} is the center-to-center distance between i and j dipoles, and $u_{\mathrm{dd,CG}}$ is the CG pair potential between two extended dipole molecules, which is defined as,

$$u_{\mathrm{dd,CG}} \left(r_{ij} \right) = u^{\mathrm{ff}}_{\mathrm{vdW,CG}} \left(r_{ij} \right) + u^{\mathrm{ff}}_{\mathrm{elec,CG}} \left(r_{ij} \right) , \tag{4.3}$$

where $u^{\mathrm{ff}}_{\mathrm{vdW,CG}}$ is the coarse-grained fluid-fluid vdW potential and $u^{\mathrm{ff}}_{\mathrm{elec,CG}}$ represents the fluid-fluid electrostatic interaction between two extended dipole molecules. In order to determine the $u^{\mathrm{ff}}_{\mathrm{vdW,CG}}$ in Eq. 4.3, we model it by uniform cubic-B splines, due to their flexibility and robustness. Hence, $u^{\mathrm{ff}}_{\mathrm{vdW,CG}}$ can be expressed as,

$$u^{\mathrm{ff}}_{\mathrm{vdW,CG}}(r) = \begin{bmatrix} 1 & t & t^2 & t^3 \end{bmatrix} \frac{1}{6} \begin{bmatrix} 1 & 4 & 1 & 0 \\ -3 & 0 & 3 & 0 \\ 3 & -6 & 3 & 0 \\ -1 & 3 & -3 & 1 \end{bmatrix} \begin{bmatrix} c_j \\ c_{j+1} \\ c_{j+2} \\ c_{j+3} \end{bmatrix} , \tag{4.4}$$

where the separation interval from 0 to the cut-off, $R^{\mathrm{ff}}_{\mathrm{cut}}$, is discretized into $n-1$ segments, $\{r_0, r_1, r_2, ..., r_{n-1}\}$, of equal size $\Delta r = R^{\mathrm{ff}}_{\mathrm{cut}}/(n-1)$ such that $r_i = i \times \Delta r$ $(i \in (0...n-1))$, $\{c_0, c_1, c_2, ..., c_{n+1}\}$ are the spline knots, the index j satisfies the condition $r_j \leq r < r_{j+1}$, and $t = \frac{r-r_j}{\Delta r}$. According to Fig. 4.1(a), the electrostatic part of the pair potential in Eq. 4.3 can be written as,

$$u^{\mathrm{ff}}_{\mathrm{elec,CG}}\left(r_{ij}\right) = A_c \sum_{l=1}^{2} \sum_{k=1}^{2} \frac{q_{il} q_{jk}}{4\pi\varepsilon_0 \left|\boldsymbol{r}_{il} - \boldsymbol{r}_{jk}\right|}, \tag{4.5}$$

where q_{il} and q_{jk} are the point charges of dipole molecules i and j, respectively, $q_{i1} = q_{j1} = -q$ and $q_{i2} = q_{j2} = +q$, in which q is set to the charge of the oxygen atom in the SPC/E water model, i.e., $q = 0.8476$, ε_0 is the vaccum dielectric permittivity, and $\boldsymbol{r}_{il}$ and $\boldsymbol{r}_{jk}$ are the positions of q_{il} and q_{jk}, respectively. In Eq. 4.5, A_c is the charge scalar factor to be optimized within the relative entropy framework.

Given the definitions of the pair potentials in Eqs. 4.4 and 4.5, the optimization parameters consist of a set of knot values and a scalar charge factor, i.e, $\boldsymbol{\lambda} = \{c_0, c_1, \ldots, c_{n+1}, A_c\}$. Since all the adjustable parameters are linear coefficients in the potential, there exists a single global minimum for the relative entropy function [133]. To obtain these parameters, we use the Newton-Raphson optimization technique. In each iteration the parameters are obtained from the following relation,

$$\boldsymbol{\lambda}^{(k+1)} = \boldsymbol{\lambda}^{(k)} + \omega d\boldsymbol{\lambda}, \tag{4.6}$$

where ω is the relaxation factor and $d\boldsymbol{\lambda}$ is the change in the parameters at each iteration, and is given by

$$d\boldsymbol{\lambda} = -\boldsymbol{H}^{-1}_{S_{rel}} \cdot \boldsymbol{\nabla}_{\boldsymbol{\lambda}} S_{rel}, \tag{4.7}$$

where $\boldsymbol{H}_{S_{rel}}$ is the Hessian matrix. For more information regarding the expressions in Eq. 4.7 as well as the implementation, see Ref [134].

Although optimizing the CG pair potential ($u^{\mathrm{ff}}_{\mathrm{vdW,CG}}$) indirectly affects the dipolar orientations due to the change in the molecular packing, the electrostatic interaction plays an influential role on the dipole-dipole distribution, thereby directly affecting the dielectric permittivity of the fluid. In this study, we optimize the electrostatic interaction through the scalar charge factor, A_c. To gain more insight into what optimizing the parameter A_c means, we take a look at the first derivative of the relative entropy. To minimize the RE function, the optimality condition requires that the first derivative of S_{rel} w.r.t any parameter be zero, i.e.,

$$\frac{\partial S_{rel}}{\partial \boldsymbol{\lambda}} = \beta \left(\left\langle \frac{\partial U_{\mathrm{CG}}}{\partial \boldsymbol{\lambda}} \right\rangle_{\mathrm{AA}} - \left\langle \frac{\partial U_{\mathrm{CG}}}{\partial \boldsymbol{\lambda}} \right\rangle_{\mathrm{CG}} \right) = 0. \tag{4.8}$$

Thus, by using Eqs. 4.2 and 4.8, and choosing λ to be A_c, we arrive at:

$$\left\langle \sum_{i,j=1,j>i}^{N} \sum_{l,m=1}^{2} \frac{q_{il} q_{jm}}{4\pi\varepsilon_0 r_{ij}} \right\rangle_{\mathrm{AA}} = \left\langle \sum_{i,j=1,j>i}^{N} \frac{u^{\mathrm{ff}}_{\mathrm{elec,CG}}\left(r_{ij}\right)}{A_c} \right\rangle_{\mathrm{CG}} . \tag{4.9}$$

The right hand-side of Eq. 4.9 is equal to the average CG electrostatic potential divided by the factor A_c. Thus, by optimizing A_c, one can obtain the full average electrostatic potential (both short and long range) energy in the mapped all-atom ensemble. In other words,

$$\left\langle U^{\mathrm{dd}}_{\mathrm{elec,AA}} \right\rangle = \frac{1}{A_c} \left\langle U_{\mathrm{elec,CG}} \right\rangle , \tag{4.10}$$

where $U_{\mathrm{elec,CG}}$ is the total electrostatic potential energy of the CG system and $U^{\mathrm{dd}}_{\mathrm{elec,AA}}$ represents the dipolar part of electrostatic potential in the all-atom reference simulation.

4.3.2 Dielectric permittivity optimization

For a homogeneous system (bulk) of polar molecules with periodic boundary conditions, the bulk dielectric permittivity is related to the fluctuation of the dipole moment and can be calculated from the following relation [135, 136]:

$$\varepsilon_r = 1 + \frac{\left\langle \boldsymbol{M}^2 \right\rangle}{3\varepsilon_0 V k_B T}, \tag{4.11}$$

where ε_r is the bulk dielectric permittivity, V is the volume of the system, and $\boldsymbol{M}$ is the total dipole moment of the liquid defined as,

$$\boldsymbol{M} = \sum_{i=1}^{N} \boldsymbol{\mu}_i . \tag{4.12}$$

Certainly, scaling the charges through parameter A_c affects the value of the dielectric permittivity. However, for a highly polar molecule such as water, where hydrogen bonding plays an important role, the RE minimization alone does not guarantee that the bulk dielectric permittivity is reproduced. Hence, to reproduce ε_r for water, we enforce it as a constraint in the RE minimization. For this purpose, we use the constraint relative entropy (CRE) minimization method proposed in Ref [128]. In general, the CRE has the form,

$$S_{crel} = S_{rel} + \chi C\left(\boldsymbol{\lambda}\right), \tag{4.13}$$

where χ is the Lagrange multiplier, and $C(\boldsymbol{\lambda})$ is the imposed constraint. To obtain the optimal parameters we use Eq. 4.6 with $d\boldsymbol{\lambda}$ replaced by $d\boldsymbol{\lambda}^c$, which is given by,

$$d\boldsymbol{\lambda}^c = d\boldsymbol{\lambda} + \boldsymbol{H}_{S_{rel}}^{-1}\boldsymbol{J}^T \cdot \left(\boldsymbol{J} \cdot \boldsymbol{H}_{S_{rel}}^{-1}\boldsymbol{J}^T\right)^{-1}\left(C(\boldsymbol{\lambda}) + \boldsymbol{J} \cdot d\boldsymbol{\lambda}\right). \tag{4.14}$$

where $\boldsymbol{J}$ is the constraint Jacobian matrix . For the detailed derivation of the CRE method, see the supplementary information of Ref. [128]. In this study, we define C as,

$$C = \frac{1}{2}\left(\frac{\varepsilon_{r,\mathrm{CG}} - \varepsilon_{r,\mathrm{AA}}}{\varepsilon_{r,\mathrm{AA}}}\right)^2, \tag{4.15}$$

and the corresponding Jacobian matrix has only a nonzero value w.r.t the parameter A_c. Thus, it can be written as,

$$J = \left(\frac{\varepsilon_{r,\mathrm{CG}} - \varepsilon_{r,\mathrm{AA}}}{\varepsilon_{r,\mathrm{AA}}}\right)\frac{d\varepsilon_{r,\mathrm{CG}}}{dA_c}, \tag{4.16}$$

where the first derivative of ε_r w.r.t. A_c can be written as,

$$\frac{d\varepsilon_{r,\mathrm{CG}}}{dA_c} = \frac{\varepsilon_{r,\mathrm{CG}} - 1}{A_c}. \tag{4.17}$$

For details on the derivation of Eq. 4.17, see Appendix A.

4.3.3 Matching diffusion coefficient

In this study, we have also examined the diffusion coefficient of the extended dipole model. As it's the case for any CG model, the consequence of removing degrees of freedom is lower friction which results in faster dynamics for the CG models compared to the all-atom counterparts. Thus, the diffusion coefficient obtained from the CGMD simulations is typically an order of magnitude higher than the AAMD simulations [137]. One way to match the diffusion coefficient is to modify the equations of motion via a thermostat that alters the viscous frictional forces on the particles [138]. The other way is to modulate the diffusion coefficient through particles' inertia features [125]. Since the distance within the extended dipole molecule is fixed, we optimize the moment of inertia via changing the mass of the molecule. To match the diffusion coefficient, we used the downhill simplex algorithm with the following objective (or penalty) function,

$$y = |D_{tgt} - D_{CG}|, \tag{4.18}$$

where D_{tgt} and D_{CG} are the diffusion coefficients of the AA reference and CG simulations, respectively, which can be calculated from the Einstein relation,

$$D = \lim_{t\to\infty} \frac{1}{6tN} \sum_{i=1}^{N} \langle [\boldsymbol{r}_i(t) - \boldsymbol{r}_i(0)]^2 \rangle. \tag{4.19}$$

4.3.4 Wall-fluid potential for confinement

It is known that the bottom-up systematic CG potentials developed for bulk systems may not be transferable in the presence of an external potential. For instance, it has been shown that the bulk-based CG potential may not adequately represent the water structure close to the planar graphene sheets [34]. Recently, there have been efforts to develop systematic ways of coarse-graining for inhomogenous systems. Mashayak and Aluru [35] employed the RE method to coarse-grain both fluid-fluid and wall-fluid interactions inside the slit-like graphene channels. They have shown that by coarse-graining the wall-fluid interaction, the water density profile can be predicted reasonably well when compared to the reference AA simulations. Sanyal and Shell [139] have developed a local density-based approach that modifies the fluid-fluid interactions through a local density potential function. Wagner et al. [140] proposed an order-parameter dependent potentials, in which they have used the multiscale coarse-graining (MS-CG) approach [141, 142] where the order parameter can be local, such as local density at a CG site, or global, such as the distance from a wall. In this study, we use the approach of Mashayak et al. [35], except that we use the bulk-based CG pair potential for the fluid-fluid interaction and optimize the wall-fluid interaction within the RE framework. Thus, compared to Eq. 4.2 the total potential of a confined CG system will have an additional contribution from the wall that depends on the separation distance between the wall and the fluid, and it can be written as,

$$U_{\mathrm{CG}}^{\mathrm{wf}} = \sum_{i=1}^{N_w} \sum_{j=1}^{N_f} u_{\mathrm{CG}}^{\mathrm{wf}} \left(r_{ij} \right), \tag{4.20}$$

where N_w and N_f are the number of wall atoms and confined fluid atoms, respectively, and $u_{\mathrm{CG}}^{\mathrm{wf}}$ is the CG wall-fluid pair potential that is optimized to account for the missing structure nearby the wall-fluid interface. Similar to the bulk fluid-fluid potential, $u_{\mathrm{vdW,CG}}^{\mathrm{ff}}$, we use Eq. 4.4 to model the wall-fluid pair interaction in our simulations. Therefore, for the confined system of extended dipole molecules we perform an additional optimization to determine the CG wall-fluid interaction.

4.4 EQT-cDFT for polar liquids

As mentioned in Section 3.2, upon minimizing the grand potential of a confined fluid in contact with a bulk reservoir, the equilibrium density profile satisfies the Boltzmann relation,

$$\rho(\mathbf{r}) = \rho_{\mathrm{b}} \exp\left(-\frac{1}{k_{\mathrm{B}}T}\left(U^{\mathrm{wf}}(\mathbf{r}) + \frac{\delta F^{\mathrm{ex}}[\rho(\mathbf{r})]}{\delta\rho(\mathbf{r})} - U_{\mathrm{b}}\right)\right). \tag{4.21}$$

In the case of a neutral wall, the total wall-fluid potential can be obtained from Eq. 2.5. For a simple LJ fluid (Chapter 2) the wall-fluid pair potential is taken from the reference all-atom simulations, whereas in a system for which the wall-fluid interaction is coarse-grained, the wall-fluid potential is taken from the CG system, i.e, $u^{\mathrm{wf}}(r) = u^{\mathrm{wf}}_{\mathrm{CG}}(r)$. In this way, we systematically incorporate the information at the finer level into the continuum representation. To model the excess free energy we use the FMT approach. The excess free energy functional is split into hard sphere and dispersion parts as:

$$F^{\mathrm{ex}}[\rho(\mathbf{r})] = F^{\mathrm{ex}}_{\mathrm{hs}}[\rho(\mathbf{r})] + F^{\mathrm{ex}}_{\mathrm{disp}}[\rho(\mathbf{r})]. \tag{4.22}$$

We note that this is similar to what Mashayak et al. have used in the Langevin-Poisson-EQT method [37]. The first and second terms in Eq. 4.22 can be obtained from Eq.2.14 and using the MFA, the second term can be modeled as,

$$F^{\mathrm{ex}}_{\mathrm{disp}}[\rho(\mathbf{r})] = \int\int \rho(\mathbf{r})\rho(\mathbf{r}')u^{\mathrm{ff}}(r)d\mathbf{r}d\mathbf{r}', \tag{4.23}$$

where $u^{\mathrm{ff}}(r)$ is the effective fluid-fluid potential, and r is bounded between the inner and outer cutoffs, R_{min} and R_{cut}, respectively. Similar to the treatment of the wall-fluid potential, the effective fluid-fluid interaction is taken from the CG model, i.e, $u^{\mathrm{ff}}(r) = u^{\mathrm{ff}}_{\mathrm{vdW,CG}}(r)$. We note that due to the mean-field approximation in FMT and absence of an external electric field, all the dipole orientations are equally likely [143]. Hence, there would be no electrostatic contribution to the excess free energy functional (Eq. 4.22). Once the excess free energy functional is determined, using Eqs. 4.22, 2.14,and 2.17, Eq. 4.21 can be rewritten as,

$$\rho(\mathbf{r}) = \rho_{\mathrm{b}} \exp\left(-\frac{1}{k_{\mathrm{B}}T}\left(U^{\mathrm{wf}}(\mathbf{r}) + U^{\mathrm{ff}}_{\mathrm{hs}}(\mathbf{r}) + U^{\mathrm{ff}}_{\mathrm{CG}}(\mathbf{r}) - U_{\mathrm{b}}\right)\right), \tag{4.24}$$

where $U^{\mathrm{ff}}_{\mathrm{hs}}$ is obtained from Eq. 2.16: and the CG fluid-fluid potential energy is given by

$$U^{\mathrm{ff}}_{\mathrm{CG}}(\boldsymbol{r}) = \int_{r=R_{\mathrm{min}}}^{r=R_{\mathrm{cut}}} \rho(\mathbf{r}')u^{\mathrm{ff}}_{\mathrm{vdW,CG}}(r)d\mathbf{r}'. \tag{4.25}$$

4.5 Simulation Details

4.5.1 MD simulations

In general, for any bottom-up coarse graining method, a set of reference trajectories are required to obtain the corresponding CG potentials. As mentioned in Section 4.2, we parametrized the CG potentials to reproduce RDF and dielectric constant of the bulk SPC/E water. All the simulations were performed in the canonical ensemble (NVT) using the GROMACS [144] software. Equations of motion are integrated with the leap-frog algorithm with a time step of 1 fs. During the simulations the temperature is kept constant at 298K using the Nosé-Hoover thermostat with a 0.2 ps time constant. For the bulk simulations, all systems were initially equilibrated for 2 ns, following a 10 ns of production run. The SHAKE algorithm [145] was used to keep water molecules rigid. For the short-ranged interactions, the cutoff radius was set to 1.2 nm. Both energy and pressure tail corrections [146] have been applied to the standard 12-6 LJ potential for the bulk MD simulations. The long range electrostatic interactions were calculated using the particle mesh Ewald (PME) summation [147] with the tinfoil boundary condition (infinite dielectric) and a FFT grid spacing of 0.12 nm. Periodic boundary conditions were applied in all the directions. In order to obtain enough statistics to calculate the bulk dielectric permittivity, trajectories of atoms were collected every 0.1 ps. For the confined water simulations, our system consists of two parallel graphene sheets separated at a distance of H in the z direction. The lateral dimensions lie in xy plane with an area of $3.834 \times 3.68927\,\mathrm{nm}^2$. A periodic boundary condition was applied in all the directions with an extra vacuum of 30σ (where σ is the diameter of the water oxygen atom, and is equal to 0.317 nm) in the z direction to avoid slab-slab interactions between periodic images. The LJ length and energy scale parameters for carbon-water interaction (σ_{cw}, ε_{cw}) are 0.32777 nm and 0.38959 kJ/mol, respectively. The cut-off radius for the short-ranged interactions, was set to 0.9 nm. During the simulation, the graphene sheets were frozen, i.e., their positions were not updated. In this study, we have considered simulating water in neutral channels of width 10σ, 7σ, and 4σ. The number of water molecules in these channels and the interaction parameters are adopted from reference [34]. Additionally, we have simulated water in a capacitor channel of width 12σ, where a uniform partial charge was assigned to the wall atoms to achieve the surface charge density of $-0.061\,\mathrm{C/m}^2$ and $+0.061\,\mathrm{C/m}^2$ for the left ($z = 0$) and right ($z = H$) walls, respectively. The number of water molecules inside the channel were tuned such that the water bulk density is recovered in the middle of the channel. In order to obtain reliable results, especially in calculating the dielectric permittivity, the equilibrium properties are averaged over a set of 7 MD simulations of length 8 ns, in which the first 2 nanoseconds were discarded.

4.5.2 CG simulations

For all the CGMD simulations, we follow the same procedure as in AAMD simulations (see Section 4.5.1). To obtain the CG potentials and parameters, we used and modified the VOTCA software [134] to perform RE and CRE minimization. To obtain the CG potentials, PME is used for long-ranged electrostatic interactions. Nevertheless, we have also examined using the reaction field to incorporate the water screening effects through a constant dielectric permittivity of 71.89, in accordance with the SPC/E water model dielectric constant. The cut-off used for the short-ranged Coulomb interactions with reaction field was chosen based on the correlation length of the dipole-dipole pair correlation function, which is chosen as 1.2 nm. Beyond this distance the dipole-dipole pair correlation function decays to zero. Therefore, based on this criterion we treat water as a continuum dielectric media beyond 1.2 nm. Furthermore, to verify 1.2 nm is an appropriate cut-off for the reaction field, we performed another simulation with a cut-off of 1.5 nm and found no changes in the results. Once the optimal CG potentials are obtained, we perform the downhill simplex algorithm implemented in VOTCA package [134] to reproduce the diffusion coefficient of SPC/E water at the temperature of 298 K and density of $1.0\,\mathrm{g/cm^3}$. We verified that the water structure, permittivity, and all the correlation functions remained unchanged upon matching diffusion or using reaction field for electrostatic interactions. Finally with the aid of the softer CG potentials, we can increase the integration time step to speed up and run longer simulations. For this purpose, we setup the CGMD simualtion with the time step of 6fs, and we observed that the results were unchanged. Therefore, on four cores of Intel Xenon CPU ES-1607 3.00GHz processor compared to the AAMD simualtions, the CGqε model is about an order of magnitude faster. In addition, using the reaction field instead of PME, gives an extra speed up factor of ∼1.5 in the CGMD simulations. The potential parameters and tables along with the running files for CGMD simulations are publicly available on GitHub [148].

4.5.3 EQT simulations

To obtain density and potential profiles in the EQT simulations, we self-consistently solve Eqs. 2.5 and (4.24)-(4.25). To obtain the bulk potential in Eq. 4.24, we use Eqs. 2.16(check) and 4.25 with the corresponding bulk density. For all the pair interactions the cut-off radius is set to 0.9 nm consistent with the confined AAMD and CGMD simulations. The $R^{\mathrm{ff}}_{\mathrm{min}}$ and the hard sphere diameter, d_{hs}, are set to 0.26 nm and 0.27 nm, respectively. These values are chosen such that the density profiles from the EQT simulations compare well with the AAMD simulations. As mentioned in Section 4.4 all the vdW pair interactions are adopted from the CGMD simulations. By incorporating the interaction information at a finer level, EQT bridges the gap between the atomistic and the continuum representations. In EQT, we approximate the wall by a continuum media with a uniform density. In the case of a graphene interface, the wall density, ρ_{wall}, is set to 38.18 atoms/nm^3. Given the set of parameters and potentials, we start with the bulk density as our initial guess and iteratively solve the aforementioned equations using the Picard iteration method with a relaxation factor of 0.02.

In order to obtain the density, orientation and polarization profiles for the capacitor wall, EQT is coupled with the Poisson equation to account for the electrostatic interactions between the wall and dipoles through the mean field approximation and the Langevin dipole (LD) model [37]. Unlike the neutral wall case, oppositely charged walls generate an external electric field that directly affects the molecule dipole orientation. In this case, in addition to the vdW interactions, the total potential energy has a non-zero electrostatic part which can be written as,

$$U_{\text{elec}}(z) = \mu \left\langle \cos\theta(z) \right\rangle \frac{d\phi(z)}{dz}, \tag{4.26}$$

where ϕ is the electrostatic potential, $\cos\theta(z)$ is the average cosine of dipole orientation, and θ is defined as an angle between the positive z axis and the dipole moment vector. In Eq. 4.26, the electrostatic potential can be obtained from the Poisson equation. For the case of ion-free water confined in a capacitor wall, the Poisson equation reads,

$$\frac{d^2\phi}{dz^2} = \frac{1}{\epsilon_0}\frac{dP_\perp(z)}{dz}, \tag{4.27}$$

with the following boundary conditions

$$\left.\frac{d\phi}{dz}\right|_{z=0} = -\frac{\sigma_{\text{wall-L}}}{\varepsilon_0}, \tag{4.28a}$$

$$\left.\frac{d\phi}{dz}\right|_{z=H} = \frac{\sigma_{\text{wall-R}}}{\varepsilon_0}, \tag{4.28b}$$

$$\phi\left(z = H/2\right) = 0, \tag{4.28c}$$

where $\sigma_{\text{wall-L}}$ and $\sigma_{\text{wall-R}}$ are the surface charge densities of the left ($z = 0$) and right ($z = H$) walls, respectively. Furthermore, in Eq. 4.27, $P_\perp(z)$ is the perpendicular orientation polarization which can be expressed as,

$$P_\perp(z) = \rho(z)\mu \left\langle \cos\theta(z) \right\rangle. \tag{4.29}$$

In order to avoid the divergence of Picard iteration, we start with the neutral wall solution (density) and increase the surface charge density in a step by step manner using an increment of 0.0122 C/m^2. In each step, we determine the density profile and use it as an initial guess for the next surface charge density. We repeated this process until we reach the target surface charge density of 0.061 C/m^2 on the walls. For a

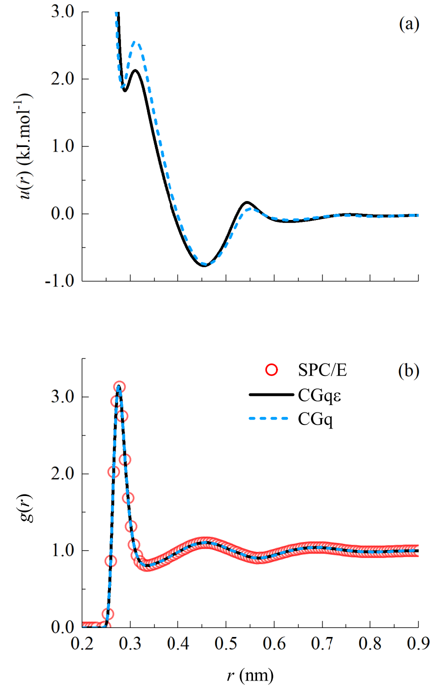

Figure 4.2: (a) Dipole-dipole CG potentials obtained by CGq and CGqε methods. (b) Comparison of the center-of-mass radial distribution functions from AAMD and CGMD simulations.

detailed derivation and numerical implementation of the Langevin-Poisson-EQT method, see Ref. [37].

4.6 Results

4.6.1 Bulk

As mentioned in Section. 4.2, we adopt two approaches to obtain the fluid-fluid CG potentials for the extended dipole molecules. The potentials obtained via the charge optimization method are referred to as CGq, and those obtained by the dielectric permittivity optimization are denoted by CGqε. Fig. 4.2 shows the vdW CG potentials and RDF profiles from the CGq and CGqε method.

As illustrated in Fig. 4.2(b), both methods are able to match the water RDF from the reference AA simulations. Since we are using the relative entropy method, which is a structure-based CG method, it is guaranteed that upon a finely discretized grid space in the pairwise distances, the CG potential can reproduce the target RDF [132, 133]. It is interesting to observe that even though our CG model explicitly considers the electrostatic interactions (through a dipole moment), the CG potentials still exhibit a well-known double-well-type shape similar to what has been observed for single site spherical water CG models.

Table 4.1: Charge, dipole moment and dielectric permittivity values for SPC/E, CGq, and CGqε water models.

Model	A_c	q (e)	μ (D)	ε_{r}
CGq	0.3544	0.5046	1.399	21.45
CGqε	0.6555	0.6862	1.903	72.92
SPC/E	1.0	0.8476	2.350	71.89

The double-well-type shape potential has been shown to be important to represent the tetrahedral packing of water [137]. A simple Stockmayer fluid [121] (point dipole + LJ interaction site), which does not have a double-well-type shape potential, may not be able to fully represent the tetrahedral packing of the water molecules [124]. Therefore, it is essential to have a double-well shape potential between the dipoles in order to reproduce the water structure. Table. 4.1 summarizes the values of A_c, charge, dipole moments and bulk permittivity for SPC/E, CGq, and CGqε water models. The results show that charge optimization alone cannot reproduce the dielectric permittivity of the SPC/E water model. Despite taking into account the dipolar fluctuations in the CG model, relative entropy minimization fails to reproduce the dielectric permittivity of water.

Thus, it is necessary to look at correlation functions, other than the RDF, to investigate why the CGqε method is capable of reproducing the dielectric constant of water. Since the dielectric permittivity is directly related to the electrostatic interactions, we investigate the orientational correlation functions in bulk water. For a system of water molecules, complete information regarding the correlations between the molecules (spatially and orientationally) is given by the molecular pair distribution function, $g\,(1,2) = g\,(\boldsymbol{r}_1, \boldsymbol{r}_2, \boldsymbol{\Omega}_1, \boldsymbol{\Omega}_2)$, which depends on the positions $(\boldsymbol{r})$ and angles $(\boldsymbol{\Omega} = (\theta, \phi))$ of molecules 1 and 2 [149] (see Fig. 4.1(b)). The orientational part of $g(1,2)$ can be expanded into an infinite basis set of angular functions using generalized spherical harmonics. However, not all terms in the expansion are necessary to obtain insights into the long-range orientational ordering in water. Since the dipole-dipole interaction is the dominant term in the multipole expansion of the long-ranged part of the molecular pair potential, we restrict our attention to the minimal basis set for dipolar molecules first introduced by Wertheim [150]. Thus, $g(1,2)$ can be approximated by,

$$g(1,2) \approx g(r)S + 3h_{\Delta}(r)\Delta(1,2) + \frac{3}{2}h_D(r)D(1,2), \tag{4.30}$$

where $g(r)$ is the radial distribution function, $h_{\Delta}(r)$ is the dipole-dipole pair correlation function, and $h_D(r)$ represents the angular dependence of the dipole-dipole interaction energy. S, $\Delta(1,2)$, and $D(1,2)$ are the basis sets and are defined as,

$$S = 1, \tag{4.31a}$$

$$\Delta(1,2) = \hat{\boldsymbol{\mu}}_1 \cdot \hat{\boldsymbol{\mu}}_2, \tag{4.31b}$$

$$D(1,2) = 3\left(\hat{\boldsymbol{\mu}}_1 \cdot \hat{\boldsymbol{r}}_{12}\right)\left(\hat{\boldsymbol{\mu}}_2 \cdot \hat{\boldsymbol{r}}_{12}\right) - \hat{\boldsymbol{\mu}}_1 \cdot \hat{\boldsymbol{\mu}}_2, \tag{4.31c}$$

where $\hat{\boldsymbol{\mu}}$ is the unit vector in the direction of $\boldsymbol{\mu}$ and $\hat{\boldsymbol{r}}_{12}$ is the unit vector in the direction of $\boldsymbol{r}_{12} = \boldsymbol{r}_2 - \boldsymbol{r}_1$. Note that these basis sets are orthogonal but not orthonormal. For more information regarding these basis sets and their properties see Refs. [149–151].

Using the definition of $\Delta(1,2)$ given by Eq. 4.31b, we can calculate $h_\Delta(r)$ from MD simulation as,

$$h_\Delta(r) = \frac{1}{N\rho_b}\langle \sum_{i=1}^{N}\sum_{j\neq i}^{N} \hat{\boldsymbol{\mu}}_i \cdot \hat{\boldsymbol{\mu}}_j \delta\left(\boldsymbol{r} - \boldsymbol{r}_{ij}\right)\rangle. \tag{4.32}$$

Furthermore, by looking at the definition of the total dipole moment vector (Eq. 4.12), we can write,

$$\langle \boldsymbol{M}^2 \rangle = \sum_{i=1}^{N}\sum_{j=1}^{N}\langle \boldsymbol{\mu}_i \cdot \boldsymbol{\mu}_j \rangle = N\langle \mu^2 \rangle + \langle \mu^2 \rangle \sum_{i=1}^{N}\sum_{j\neq i}^{N}\langle \hat{\boldsymbol{\mu}}_i \cdot \hat{\boldsymbol{\mu}}_j \rangle. \tag{4.33}$$

Using Eqs. 4.32 and 4.33, we arrive at,

$$\langle \boldsymbol{M}^2 \rangle = N\langle \mu^2 \rangle \left(1 + \int \rho_b h_\Delta(r) d\boldsymbol{r}\right), \tag{4.34}$$

where the term in the parenthesis is the well-known Kirkwood g-factor, G_k, which is obtained as the asymptotic value of the r-dependent Kirkwood g-factor,

$$G_k\left(r\right) = 1 + \int_0^r \rho_b h_\Delta(r) d\boldsymbol{r}. \tag{4.35}$$

It can be seen that for uncorrelated dipoles, the value of G_k is equal to 1.

Fig. 4.3(a) shows the comparison of dipole-dipole pair correlation function from AAMD, CGq, and CGqε. We observe that h_Δ is longer-ranged than the radial distribution function and decays in an oscillatory manner consistent with the recent second-harmonic light scattering experiments [152, 153]. This long-range behavior has also been observed by previous studies from molecular dynamic simulations [149, 154–157]. From AAMD simulations, we observe that there is a strong short-ranged correlation between dipoles of water molecules in the first solvation shell (∼3Å). This is due to the fact that the hydrogen bonding imposes a strict restriction on the molecular orientations, thus, adjacent water molecules tend to align via H-bond network [136]. In fact, such a strong positive dipole-dipole correlation can partly explain the high dielectric permittivity of hydrogen-bonded fluids such as water [136, 158]. It can be seen that the CGqε method captures this feature

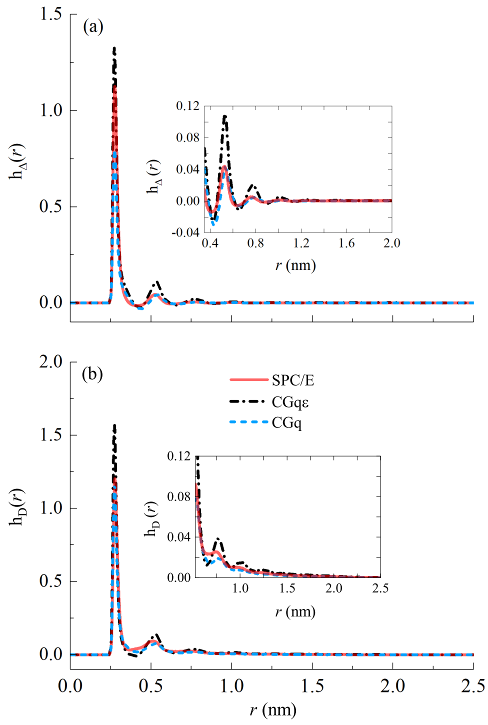

Figure 4.3: Orientational correlation functions from AAMD and CGMD simulations: (a) dipole-dipole pair correlation function (b) angular dependent part of the dipole-dipole interaction energy.

to a good extent, whereas the CGq method underestimates the first peak in the dipole-dipole pair correlation function. Interestingly, as we move away from the first peak, the CGq method closely follows the AAMD dipole-dipole pair correlation function. This indicates that at longer distances a dipolar representation of water with the CG potentials obtained from the charge optimization is able to reproduce the dipole-dipole pair correlation function. However, according to the definition of the bulk permittivity, Eq. 4.11, and Eq. 4.34, we see that the bulk dielectric permittivity depends not only on the G_k (integral of h_Δ) but also on the magnitude of the dipole moment (μ^2). Therefore, solely optimizing the charges does not guarantee that the water dielectric permittivity is reproduced.

Fig. 4.4(a) shows the r-dependent Kirkwood factor for CG and AA models. It can be seen that $G_k(r)$ asymptotically reaches a plateau. We can also observe that the most important contribution for the SPC/E model comes from the first shell of neighbors, which could be associated with the short-ranged H-bond network in water [136]. It can be seen that the CGqε method follows the SPC/E curve reasonably well up to first coordination shell. Indeed this is not surprising, as the first peak in the dipole-dipole pair correlation function is better captured by the CGqε method. However, unlike in SPC/E, we observe another jump around 0.6 nm, which causes the curves to deviate from each other. The reason behind this can be understood by looking at locally varying dielectric permittivity, which represents screening variations in the neighborhood of an arbitrary molecule. By using Eqs. 4.11, 4.34, and 4.35, we arrive at,

$$\varepsilon_r(r) = 1 + \frac{N \left\langle \mu^2 \right\rangle G_k(r)}{3\varepsilon_0 V k_B T}. \tag{4.36}$$

We note that there exist other ways to calculate the local dielectric constant such as using a composite r-dependent Kirkwood factor which combines the results of the constant electric field and constant electric displacement simulations [159].

Fig. 4.4(b), shows the locally varying dielectric permittivity from AA SPC/E model, CGq and CGqε methods. We observe that the local screening effects are more prominent in the SPC/E model, whereas in the CGqε method these effects are underestimated. Thus, the dipoles are more correlated from the CGqε method compared to the AA SPC/E model (see Figs. 4.3(a) and 4.4(a)). However, by construction, the CGqε is able to converge to the SPC/E model beyond 2.5 nm, where dipoles are not correlated and the value of the permittivity reaches its macroscopic value. On the other hand, although CGq method is able to reproduce the AAMD dipole-dipole pair correlation function reasonably well (especially at longer distances) due to its low dipole moment, it drastically underestimates the screening effects; hence it fails to reproduce the dielectric constant of water.

Another important quantity that can be studied is $h_D(r)$, which represents the angular dependence of the dipole-dipole interaction energy, and can be defined as,

$$h_D(r) = \frac{1}{N\rho_b} \langle \sum_{i=1}^{N} \sum_{j>i}^{N} \left[3\left(\hat{\boldsymbol{\mu}}_i \cdot \hat{\boldsymbol{r}}_{ij}\right)\left(\hat{\boldsymbol{\mu}}_j \cdot \hat{\boldsymbol{r}}_{ij}\right) - \hat{\boldsymbol{\mu}}_i \cdot \hat{\boldsymbol{\mu}}_j\right] \delta\left(\boldsymbol{r} - \boldsymbol{r}_{ij}\right) \rangle. \tag{4.37}$$

Using Eq. 4.37 we can write the expression between $h_D(r)$ and average electrostatic dipolar energy as follows,

$$\langle U^{dd} \rangle = -4\pi N \rho_b \int_0^\infty \mu^2 \frac{h_D(r)}{r} dr. \tag{4.38}$$

Note that in Eq. 4.38, we use the convention $4\pi\varepsilon_0 = 1$ for simplicity. Fig. 4.3(b) shows the comparison of $h_D(r)$ from AAMD, CGq, and CGqε. Unlike $h_\Delta(r)$, the correlation function, $h_D(r)$ is almost positive everywhere, suggesting that the preferable alignment of dipoles is to lower the dipole-dipole interaction energy [149]. Moreover, by examining the inset of Fig. 4.3(b), we observe that $h_D(r)$ is much longer-ranged than dipole-dipole pair correlation function, as $h_D(r)$ represents the angular dependent part of the dipole-dipole interaction energy and decays as $\sim r^{-3}$ at large distances. However, the results reported from MD

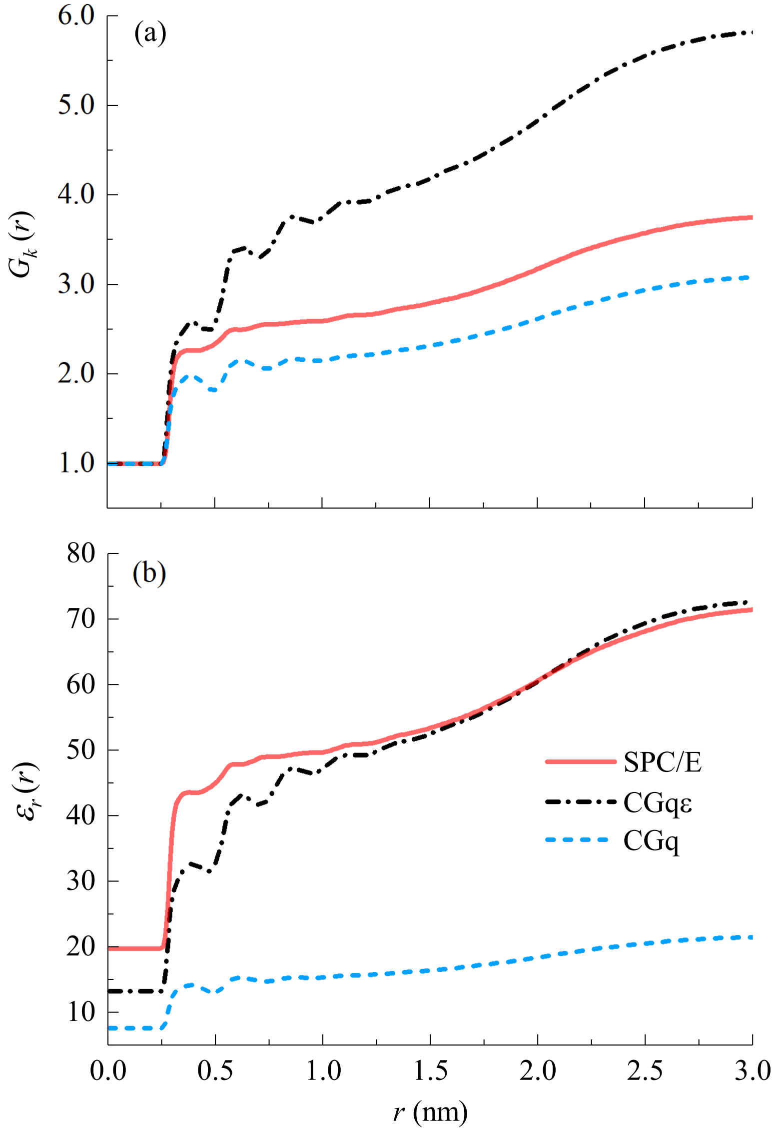

Figure 4.4: (a) r-dependent Kirkwood factor. (b) The r-dependent local dielectric constant obtained from Eq. 4.36.

Table 4.2: Electrostatic potential energy for SPC/E, CGq, and CGqε water models.

Model	U^{elec} (kJ/mol)	A_c
SPC/E	-121459.02	1.0
CGq	-18848.88	0.3544
CGqε	-42971.05	0.6555
SPC/E(dipole-dipole)	-53175.6	1.0

Table 4.3: Mass and the diffusion coefficient values for the CGqε and SPC/E water models.

Model	m (amu)	$D(10^{-5}\,\mathrm{cm}^2/s)$
SPC/E	18.0154	2.5875 ± 0.1045
CGqε	18.0154	10.2096 ± 0.0052
CGqε	141.00	2.5606 ± 0.0298

simulations are somewhat inconclusive [155]. Although it seems that the h_D correlation function decays to zero beyond 25Å, recent large scale MD simulations have shown that it has a non vanishing tail even at 75Å [154, 160]. However, in order to have a one to one comparison with the experiment and to precisely determine the range at which h_D decays to zero, it requires a very large simulation box (at least 10 nm) [153], which is computationally expensive from AAMD simulations. From the CGMD simulations, it can be seen that the CGq method is able to capture the variation in h_D correlation function to a good extent. This is a promising result which can accelerate the simulations compared to AAMD and provide insights into long-ranged behavior of dipolar alignment with respect to a vector along their separation distance, that can be a subject of future studies. Table 4.2 summarizes the total dipole electrostatic energy from AAMD, CGq and CGqε simulations. As mentioned in Section 4.3.1, scaling the CGq electrostatic potential by the factor A_c^{-1}, recovers the all-atom dipole electrostatic potential. However, Eq. 4.38 cannot represent the full electrostatic potential of the system of water molecules, as the higher dipole moment of water plays an important role in the electrostatic potential of the system.

Finally, as mentioned in Section 4.3.3, to match the diffusion coefficient, we optimized the mass of the molecule via simplex algorithm after obtaining the CG potential parameters via the CGqε method. Table 4.3 summarizes the results for optimal mass and the diffusion coefficient from the downhill simplex algorithm. We observed that optimizing the mass did not affect the structure and the dielectric permittivity value obtained from the CGMD simulations.

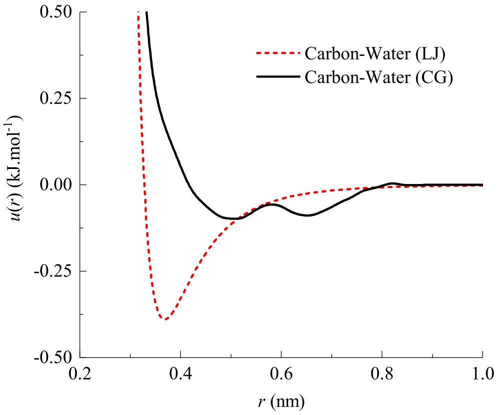

Figure 4.5: Carbon-water pair potentials used in AAMD and CGMD simulations. The red color (dashed line) represents the 12-6 LJ potential between carbon and oxygen. The black color (solid line) is the coarse-grained carbon-water interaction obtained by relative entropy minimization.

4.6.2 Confinement

Neutral Walls

Fig. 4.5 shows the pair potential between carbon and water from all-atom and coarse-grained representation. We observe that upon coarse graining water into extended dipole molecules, the effective wall-fluid pair potential is no longer of the 12-6 LJ interaction form. In fact, the CG optimization yields a double-well-type pair potential, suggesting that the energy and length scales have to be altered in order for the CG model to reproduce water structure at the interface.

Fig. 4.6 shows the density profiles of water inside slit-like graphene channel of width 10σ from both AAMD and CGMD simulations. In this figure, "wflj" refers to the wall-fluid interaction used to perform the confined AAMD simulations (i.e., standard 12-6 LJ interaction between carbon and oxygen). We observe that the confined CG system ,in which a water molecule is coarse-grained into an uncharged spherically symmetric bead (CG-wflj), overestimates the first density peak and exhibits a shoulder peak at about 2 molecular diameter away from the wall compared to the AA SPC/E water model. This clearly shows that the bulk fluid-fluid potential optimized for the single-site CG water is not transferable to the non-bulk (inhomogenous) environment [124]. In other words, the molecular packing of the water molecules close to an interface is quite different than in bulk. Thus, it's not surprising that an isotropic single-site CG model of water fails to accurately predict the confined water density profile [34, 161]. On the other hand, switching from the confined single-site representation to the extended dipole model (CGqε-wflj), improves the water density distribution beyond the first valley (0.5 nm away from the wall), making the model more

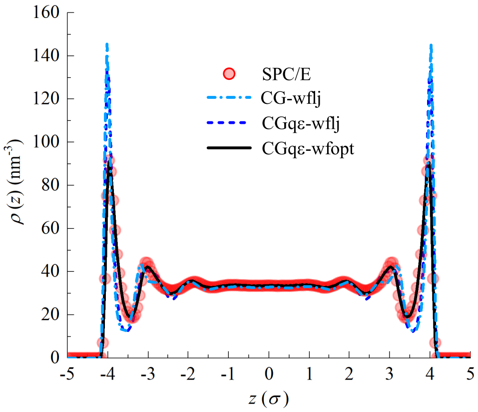

Figure 4.6: Comparison of the water density profiles from CGMD and AAMD simulations inside a 10σ channel with different fluid-fluid and wall-fluid pair potentials.

transferable and shows the role of the anisotropic forces in the fluid-fluid CG potential arising from the explicit electrostatic interactions. However, the density near by the interface (where the wall-fluid interaction is dominant) is not well-captured compared to the AA distribution, which indicates that the LJ wall-fluid interaction is too attractive for the confined CG system. This fact is more evident by looking at Fig. 4.5, where the energy scales associated with the CG wall-fluid potential are much less than the depth of the carbon-water LJ potential well. Thus, by optimizing the wall-fluid interaction and using the bulk fluid-fluid CG potential for the extended dipole model (CGqε-wfopt), the water structure can be predicted reasonably well when compared to the AAMD simulation. From here on, unless otherwise noted, by CGMD simulation, we refer to the confined extended dipole system with the CG wall-fluid potential (CGqε-wfopt).

It is well-known that the presence of a solid surface not only gives rise to density variations in the direction perpendicular to the solid surface, but also affects the molecular packing of the fluid parallel to the interface. For this purpose, we have divided the density profile into three regions: I) interfacial region II) intermediate and III) bulk-like region (see Fig. 4.7(a)). In each layer we have calculated the water center-of-mass in-plane (lateral) RDF and compared that to the bulk radial distribution function. The RDFs are calculated in the slabs centered at the location of the maximum density with a thickness of 1Å to avoid interference of atoms from the adjacent layers [162]. The in-plane RDF provides information on how molecules arrange in the plane parallel to the wall (here, x-y plane), hence, it can be used to identify ordering and possible phase transition close to an interface [8, 9, 163]. A CG model that can capture structural variations both in the parallel and perpendicular directions to an interface can be of high value. Figs. 4.7(b) and (c) show the lateral RDFs for region I and II from both AAMD and CGMD simulations. Compared to the bulk, the radial distribution of the contact layer (region I), is more structured and pronounced, showing a higher degree of

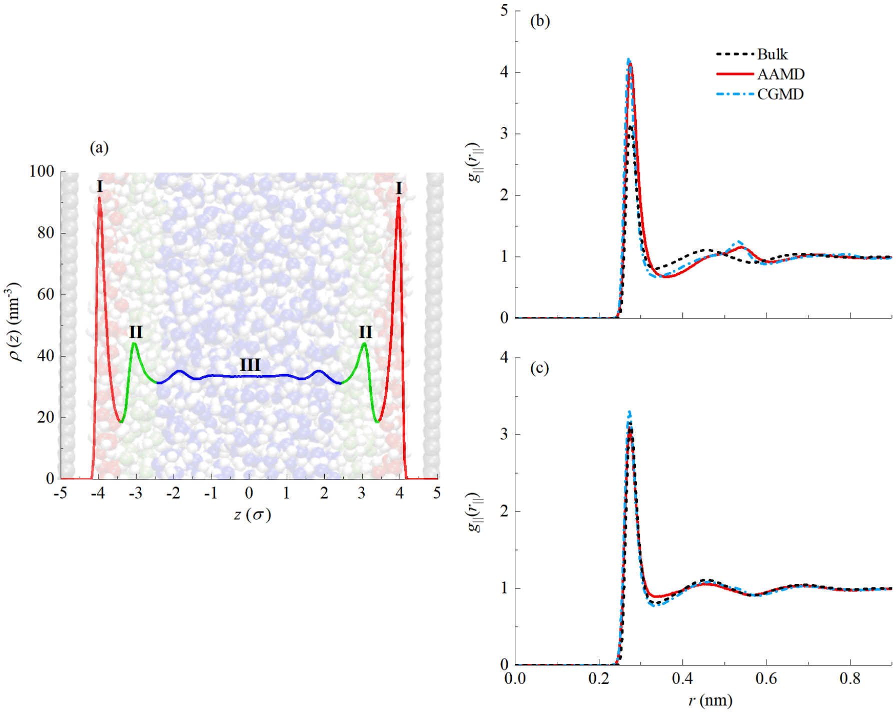

Figure 4.7: (a) Snapshot of water confined in a 10σ graphene channel. We define three different regions: an interfacial region (I), an intermediate region (II), and a central region (III), where the in-plane RDF does not show any significant deviation from the bulk RDF. Hydrogen atoms are depicted as white and oxygen atoms are colored as red, green, and blue in regions I, II, and III, respectively. The in-plane RDFs from AAMD and CGMD simulations correspond to regions I (b) and II (c). The dashed line in the figure represents the in-plane RDF far from the surfaces (bulk).

ordering in the liquid. It can be seen that the results from the CGMD simulation are in good agreement with that of AAMD simulations. Moving away from the wall, in region II, although we observe that the first valley of the lateral RDF in AAMD is shallower than the bulk RDF, the location of the peaks and valleys follow closely the bulk radial distribution function. This indicates that the in-plane water structure in region II is similar to that of bulk with a slightly higher density. In this region the CG potentials result in an RDF very similar to that of bulk and in good agreement with AAMD simulation results.

To further test the applicability of our CG potentials, we simulated water in narrower confinements such as 7σ and 4σ channels. Fig. 4.8(a) shows the comparison of the density profiles from AAMD, CGMD, and EQT simulations. Since all the channels are in chemical equilibrium with the same bulk reservoir, the CG potentials are transferable across channels of different width. It can be seen that the results from CGMD simulations are close to AA SPC/E water model. Thus, as far as the structural properties are concerned, the physics near by the wall is captured well upon optimizing the wall-fluid interaction.

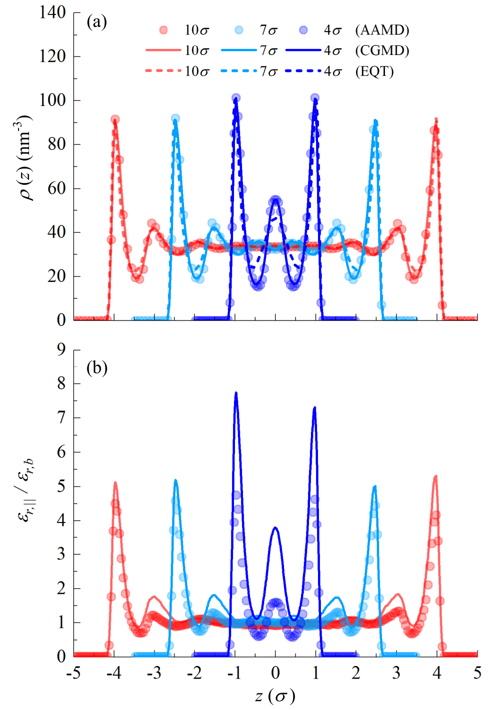

Figure 4.8: Water density distributions (a) and parallel permittivity profiles (b) inside graphene slit-like channels of various widths. In the figure, circles, solid line, and dashed line represent AAMD, CGMD, and EQT results, respectively.

Furthermore, from a continuum perspective, the use of CG potentials together with mean-field approximation (MFA) and FMT functional provides a good description of water molecular arrangement inside the neutral graphene slit channels. It is important to mention that for the neutral wall, the EQT formulation does not explicitly take into account the dipole-dipole interactions, yet we observe that except for a very narrow channel such as 4σ, where it is likely that the fluid-fluid correlations play an important role, the EQT predictions are in good agreement with AAMD and CGMD results.

One of the benefits of using the extended dipole CG model is that it retains the dipolar information necessary for permittivity calculation. This is important, as it can explicitly account for the water screening effects in confinement. For many confined systems where properties vary spatially in the confined direction, the dielectric permittivity has a tensorial form. For a slab geometry, the dielectric constant has two components that vary with the z direction (inhomogenous axis): parallel ($\varepsilon_{r,||}(z)$) and perpendicular ($\varepsilon_{r,\perp}(z)$) to the wall. To calculate each of the components we use the fluctuation formulas derived by Ballenegger and Hansen [164]. Fig. 4.8(b) shows the variation of the normalized parallel permittivity for different channel widths. The values are normalized by the bulk AA SPC/E dielectric constant value of 71.89. In the 10σ

channel, where both the layered structure and bulk region are well-formed, the dielectric permittivity is not constant, but it exhibits an oscillatory behavior in an interfacial region of three to four molecular diameters. For such a channel the water screening strength parallel to the wall is seen to be ∼5 times higher than that of bulk. This emphasizes the need of using a realistic CG model that can capture such pronounced oscillations near an interface. As we move away from the wall, $\varepsilon_{r,||}(z)$ decays until it reaches the bulk value at roughly 4 molecular diameters away from the surface. It can be seen that on average, $\varepsilon_{r,||}$ of water is higher than its bulk value, indicating that the in-plane (xy) screening effects are enhanced by the presence of a planar interface. This is also in agreement with the results of previous studies for planar interfaces [129, 165]. It can be seen that except for a very narrow confinement (4σ channel) the extended dipole CG model does a reasonable job in reproducing the parallel component of water dielectric permittivity compared to the AAMD simulations. In the 4σ channel, due to the extreme confinement effect in the z direction, the molecules are closely spaced and packed in the $x-y$ plane, which results in an enhancement of dipole-dipole correlations parallel to the surface [166]. Under these circumstances, we see that the CG model overestimates the parallel dielectric constant. This means that the dipoles are more strongly correlated in the CG representation compared to their AA counterpart. This fact is more evident by looking at the in-plane RDF of the contact layer (see Fig. 4.7(b)), where the CG model slightly overestimates the lateral RDF, which can be magnified in the case of extreme confinement such as in the 4σ channel. Furthermore, although optimizing the wall-fluid potential improved the CG density profile significantly, $u_{\mathrm{CG}}^{\mathrm{wf}}$ is isotropic and does not directly take into account the orientational degrees of freedom.

Capacitor Walls

In this section, we comment on the applicability of the EQT and the CG model on reproducing the density, polarization and dipolar angle profiles of water inside a capacitor-like channel (negative and positive walls). For this purpose, we simulated water in the presence of an external electric field generated from the negative and positive partial charges on the left and right graphene sheets. We calculated the density, dipolar angle, and polarization profiles from both atomistic and continuum simulations. Due to the presence of the charges on the wall, in addition to the vdW interactions, we have to consider the electrostatic interactions arising from the charge-dipole and dipole-dipole interactions in the EQT framework. For this purpose, we use the EQT-Langevin-Poisson framework, in which the effective electrostatic potential is calculated through the Poisson equation, and the water permittivity and polarization variations are modeled using the LD approximation. Fig. 4.9(a) shows the result for water density profile in the charged 12σ channel from AAMD, CGMD and EQT simulations. We observe that the AA water density profile is asymmetric with respect to the middle of the channel, and exhibits more pronounced peaks next to the positively charged interface. At the positively charged wall, due to the favorable electrostatic interactions between the wall and water, more oxygen atoms are attracted to the surface creating a region of high density at the interface. This causes the water dipole moments to point away from the wall, making more hydrogens available to form H-bonds with the neighboring water molecules, and resulting in an increase in water density in the preceding layer. As we move towards the middle of the channel the layering is suppressed and the bulk-like region is recovered in the central region of the channel.

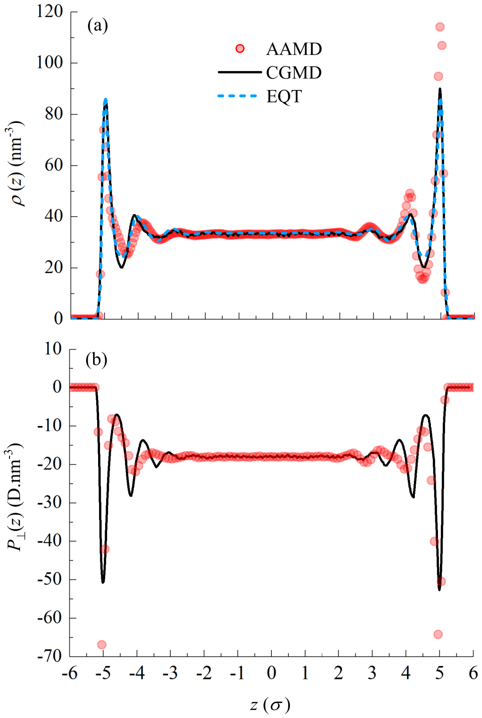

Figure 4.9: Comparison of water density profile in a capacitor channel of width 12σ.

From the CGMD simulations, the extended dipole model is able to predict the density of water molecules. However, it fails to quantitatively capture the density close to the negatively and positively charged walls. This is expected as, unlike the SPC/E AA water, the extended dipole model is incapable of forming H-bonds, and the CG wall-fluid interaction has been optimized for the neutral walls, which may not be transferable to the charged walls. The former is a limitation of the model, while the latter is the result of the well-known transferability problem of the bottom-up coarse-graining approaches. Nevertheless, the CG model is able to predict the perpendicular polarization ($P_\perp(z)$) profile in a reasonable agreement with the AAMD simulation (see Fig. 4.9(b)). This indicates that to a good extent the perpendicular permittivity variations are being captured, as the $P_\perp(z)$ is proportional to the weak electric field in the cavity by $\varepsilon_{r,\perp}$, according to the linear response theory [129].

The EQT results for density match with the CGMD simulation, which indicates that the hard sphere approximation and the mean field treatment of the electrostatic interactions together with the use of CG potentials, are capable of capturing the structural variations of the dipolar molecules inside the charged confinement. However, by looking at Fig. 4.10 (b), we observe that the EQT-Langevin-Poisson approach cannot capture the variations in the $P_\perp(z)$. Upon a closer inspection, we see that the bulk polarization value

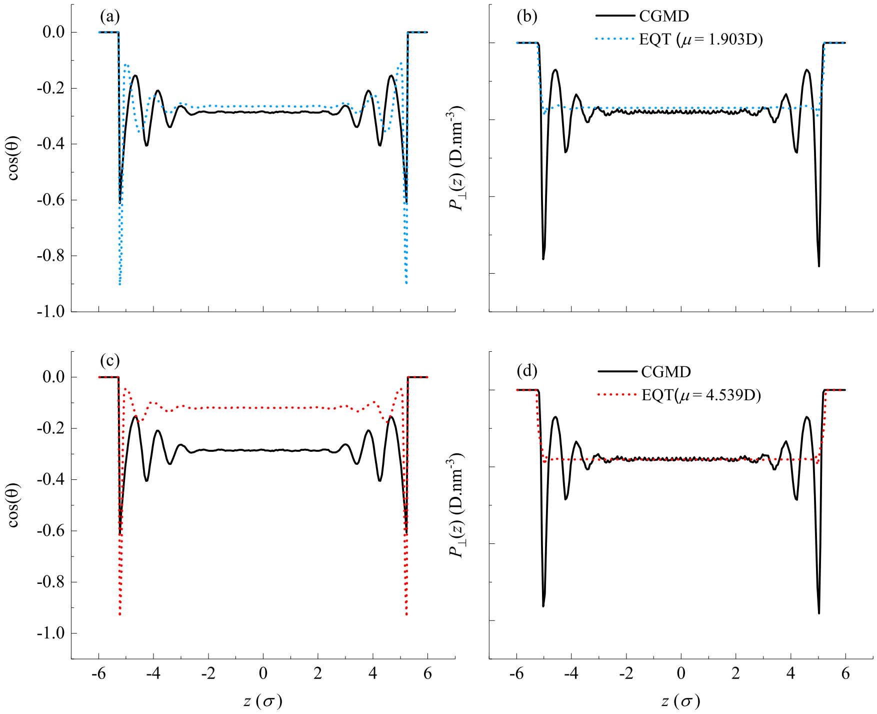

Figure 4.10: Water dipolar orientation and polarization profiles from CGMD and EQT simulations inside a capacitor channel of width 12σ.

is underestimated even though the same dipole moment as CGMD simulations is used. To understand this better we examine the average cosine of dipole orientation profile since it directly affects the polarization (see Eq. 4.29). Fig. 4.10 (a) shows the average orientation profiles from both EQT and CGMD simulations. EQT predicts a higher alignment of dipoles at the charged walls compared to the CGMD simulations, resulting in an over-screening of the external electric field that leads to a lower (in magnitude) dipole orientation in the middle of the channel. Nevertheless, EQT is able to qualitatively capture the oscillations in the average orientation profile with an offset in the location of the peaks and valleys. This is important in computing the perpendicular polarization. Since these structural variations occur over few nanometers in the vicinity of the interface, even a few Angstroms offset in the dipole orientation can drastically affect the polarization profile.

Fig. 4.11 shows the permittivity predicted by the EQT-Langevin-Poisson approach with two different dipole moments. It can be seen that when the CGMD dipole moment of 1.903 D is used, the bulk permittivity is not recovered. Thus, the dipole moment is optimized such that the bulk permittivity is recovered. With a dipole moment of 4.539 D, the polarization of water molecules in the bulk matches that of CGMD simulation (see Fig. 4.10 (d)). However, the variations are still missing. This can be attributed to two

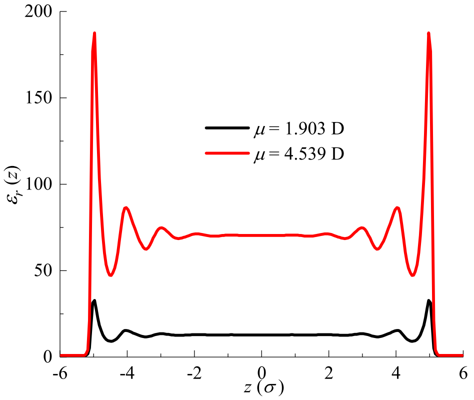

Figure 4.11: Dielectric permittivity profiles of water from the Langevin dipole model inside a capacitor channel of width 12σ with different dipole moments.

factors: The oversimplifications made in the LD approximation, and the definition of the permittivity used in the theory. In LD approximation, the molecules are treated as non-interacting dipoles, thus the dipole correlations are completely neglected, whereas in the CGMD simulations the dipoles are interacting due to the electrostatic interactions. Furthermore, in the Poisson equation, the dielectric permittivity has been modeled via one of the following approaches: using a bulk-based relation that is applicable only in the bulk or weakly inhomogenous systems, e.g. Clausius-Mossotti (CM) expression [167], phenomenological formulas that express permittivity in terms of the local density variations [167, 168], or a uniform distribution approximation throughout the inhomogenous system. As mentioned in Section 4.6.2, for a confined system, however, the dielectric permittivity has a tensorial form. Unlike the parallel permittivity that varies smoothly and locally follows the density oscillations, the perpendicular component exhibits a non-local behavior [110] with an average value as small as ∼2 compared to the bulk [169], suggesting that using bulk-based relations or local density approximations may not be an accurate way of modeling the permittivity in the Poisson equation.

4.7 Summary

In this chpater, we intorduced an extended CG dipole model for water that reproduces RDF, diffusion coefficient, and dielectric constant at room thermodynamic conditions. We showed that by merely minimizing the RE, one cannot reproduce the dielectric permittivity of bulk water. Thus, we employed the CRE method to optimize the charges and the pair potential such that the dielectric permittivity in the CG system matches that of the SPC/E AA reference simulations. We calculated the dipolar correlations in the bulk system from both CGMD and AAMD simulations. We found that the CGq method is able to capture the AAMD dipole-dipole pair correlation function. However, due to its lower screening and dipole moment, it fails to reproduce the AA SPC/E water dielectric permittivity. On the other hand, the CGqε method results in dipole moment and CG potential that reproduced water dielectric permittivity, although the local screening effects are slightly underestimated compared to that of AA SPC/E model. Furthermore, we matched the diffusion coefficient by systematically optimizing the mass of the molecule via simplex algorithm. To test our model, we demonstrated it by simulating water in slit-like graphene nano channels of various widths. We observed that without any modification to the wall-fluid interactions, the density profiles were in a good agreement with the AAMD simulations, emphasizing the role of anisotropic forces arising from the inclusion of the electrostatic interactions in the CG model. In order to obtain a quantitative agreement, we coarse-grained the wall-water interaction. Our results, revealed that the nature of the CG wall-water interaction is no longer of the 12-6 LJ potential form, but a double-well type potential with a lower attractive potential well. We showed that the agreement in density profiles from AAMD, CGMD and EQT is good. We further calculated properties such as in-plane RDFs, and parallel dielectric permittivity, and showed that the CG model is capable of reproducing these quantities in a good agreement with the AAMD simulations. Finally, to test the applicability of our model in screening the charges perpendicular to an interface, we simulated water in a capacitor wall and calculated the density, dipolar angle, and polarization profiles. Ignoring the dipole-dipole interactions (LD approximation) and improper modeling of the perpendicular permittivity in the Poisson equation, fails to capture the variations in the polarization profile, thereby providing an inaccurate picture of charge screening in confinement. However, due to the presence of dipoles and systematic parameterization, our CG model captures the polarization profile observed in AAMD simulations, suggesting that the water screening effects perpendicular to the wall have been captured to a good extent. We note that the method developed in this paper is not limited to water and can be used to coarse grain other polar molecules.

Chapter 5

A Universal Reduction in Dielectric Response of Confined Fluids

5.1 Introduction

One of the important fundamental properties of any polar fluid is its dielectric constant. In simple terms, it is the measure of the fluid's ability to screen charges. The knowledge of dielectric permittivity and its influence on electrostatic interactions are of great importance in science and technology. In energy storage devices such as electric double-layer (EDL) capacitors, the amount of energy stored in the device is directly proportional to the solvent dielectric constant, and thus, can be exploited to manipulate the capacitance [170]. In the context of coordination chemistry, dielectric permittivity is an essential component for reactions in the solution via changing the solvation free energy barriers [171]. Moreover, solubility and solvation free energy [172], ion mobility [173], and molecular transport through nanopores [174], which are relevant processes in biology [41, 175] and water desalination[176, 177] depend strongly on the dielectric permittivity and its variation near interfaces.

Similar to the structural [178, 179] and dynamical changes that a fluid undergoes in the vicinity of an interface, the dielectric response of the confined fluid is no longer a scalar quantity (as is the case in the bulk) and is a second ranked tensor exhibiting an anisotropic behavior in different spatial directions (e.g. perpendicular, $\varepsilon_\perp$, or parallel, $\varepsilon_\parallel$, to a flat interface) [39, 40]. Such an anisotropic behavior implies a strong preferred directionality for electrostatic interactions [41] and can be very important in understanding dissociation in nanoconfinement [42, 43], dielectrophoretic deposition of carbon nanotubes (CNTs) [44], developing accurate coarse-grained force fields [180] and improving the solvent-implicit approaches often used in biology and continuum theories such as the Poisson-Boltzmann (PB) equation [45] for accurate prediction of capacitance in the electric double-layer capacitors [46].

Direct measurement of the dielectric permittivity of the fluid under confinement is a very challenging task [10, 181]. Previous experiments primarily focused on water and employed different methods and techniques to measure its dielectric response perpendicular to an interface. Thin film measurements have reported a decrease in the perpendicular dielectric permittivity, $\varepsilon_\perp$, of water confined between mica plates as the water slab thickness is reduced from micrometer to nanometer [182]. For the same interface, atomic force microscopy has revealed that water dielectric constant varies from 4 to its bulk value, ε_{b} =81, within a distance of about 10 nm away from the surface [183]. On the other hand, using the streaming potential method, it was found that the dielectric permittivity of water confined in extended nano spaces is reduced to roughly 1/3 of its bulk value. Recently, capacitance microscopy analyses have revealed that water exhibits an anomalously low out-of-plane dielectric constant of 2.1, when confined between sheets of graphene and HBN. It was also found that the channel width where the water dielectric behavior converges to that of bulk extends up to mesoscales [10].

Due to the challenges and discrepancies in measuring the dielectric constant from experiments, a number of computational studies have been performed to study the dielectric permittivity of confined water at various interfaces. As shown in many studies [181, 184], bulk-based relations such as the Kirkwood-Frohlich relation [185, 186] should be avoided in calculating the interfacial dielectric permittivity. Using statistical mechanics and linear response theory, fluctuation formulas have been derived to determine the dielectric response of confined polar fluids [39, 40]. Using molecular dynamics (MD) simulations, an anomalous dielectric response was found for water confined between ionic Newton black films [187]. Later, it was shown that water exhibits a strong anisotropic dielectric relaxation when confined in graphene nanochannels [188]. This behavior led to an order of magnitude difference in the parallel and perpendicular dipolar fluctuations of water confined between graphene sheets, and was shown to persist even for a 100 nm wide channel [189]. Such anisotropic behavior has also been observed in cylindrical confinement such as in CNTs [190, 191], where the water dielectric constant parallel to the axis of CNT is enhanced while the perpendicular component is suppressed. This anomalous water dielectric behavior, particularly the reduction in perpendicular dielectric constant of water has also been reported near hydrophobic spheres [192], soft polar surfaces [193], and protein surfaces.

Albeit both computational and experimental studies have been performed on the dielectric permittivity of confined water, there have been only a few studies on non-aqueous solvents. Understanding the dielectric behavior of confined organic solvents is of paramount importance for the application of electrochemical capacitors due to their higher operating voltage thresholds compared to water. In this chapter we perform extensive MD and multiscale simulations with cumulative simulation time of 10 μs, to determine the dielectric constant as a function of channel width for water and several technologically relevant organic solvents confined in graphene slit channels. In this chapter we provide fundamental insights into the effect of confinement on perpendicular dielectric permittivity of confined fluids in slit channels of various widths. We observe universal scaling and reduction in the perpendicular dielectric permittivity as a function of the channel width. We demonstrate that the reduction in the out-of-plane dielectric permittivity exhibits a Langevin-like behavior. The reason behind this reduction is attributed to the favorable in-plane dipole-dipole interactions. Moreover, we find that the perpendicular dielectric permittivity is anomalously low in sub-nanometer channels. Finally, we introduce a multiscale parallel-plate capacitor model to calculate the perpendicular permittivity of the confined fluids. The model is more robust than the fluctuation formula (requires only two short MD simulations of about 4 ns) and its prediction of the perpendicular dielectric permittivity, in the limit of zero external electric field, agrees well with the result of the fluctuation formula.

5.2 Simulation Details

5.2.1 MD simulations

All the MD simulations were performed using the GROMACS software [194]. Equations of motion are integrated with the leap-frog algorithm with a time step of 1 fs. During the simulations, temperature is kept constant at 298 K using the Nosé-Hoover thermostat with a 0.2 ps time constant. For the bulk simulations, all systems were initially equilibrated for 5 ns, followed by a 20 ns of production run in isothermal-isobaric (NPT) ensemble with the pressure of 1 bar. For the short-ranged interactions, the cutoff radius was set to 1.2 nm. Both energy and pressure tail corrections [195] have been applied to the standard 12-6 LJ potential for the bulk MD simulations. For the bulk MD simulations, the long-range electrostatic interactions were calculated using the particle mesh Ewald (PME) summation [196] with the tinfoil boundary condition (infinite dielectric) and a fast Fourier transform (FFT) grid spacing of 0.12 nm. Periodic boundary conditions were applied in all the directions. In order to obtain enough statistics to calculate the bulk dielectric permittivity, trajectories of atoms were collected every 0.05 ps. For the confined fluid simulations, all simulations were performed in the canonical ensemble (NVT). Our system consists of two parallel graphene sheets separated at a distance of H in the z direction. The lateral dimensions lie in the x-y plane with an area of 4.17648×4.25420 nm^2. A periodic boundary condition was applied in all the directions with an extra vacuum of length at least $3H$ in the z direction to avoid slab-slab interactions between periodic images. The long-range electrostatic interactions are modeled employing the Ewald algorithm adapted for slab geometry [197]. The LJ length and energy scale parameters for carbon atoms are 0.3390 nm and 0.2334 kJ/mol, respectively. During the simulation, the graphene sheets were frozen, i.e., their positions were not updated. In this study, we have considered a total of 4 fluids of various polarity and density such as water, methanol, acetonitrile, and dichloromethane. We modelled water by the extended simple point charge model (SPC/E) and used the SHAKE algorithm [198] to maintain the molecule rigidity. For acetonitrile we adopted the six-site model from Nikitin et al. [199], where the force field parameters were optimized to reproduce the dielectric permittivity close to the experimental value. For the rest of the fluids, all parameters were adopted from the All-Atom Optimized Potential for Liquid Simulations (OPLS-AA) forcefield [200] with the exception of dichloromethane charges, which were modified for more accurate estimation of its dielectric constant [201]. Quantum, atomic and electronic polarizability effects are neglected, therefore, the fluid models are considered to be non-polarizable. In order to determine the number of confined fluid particles, each channel was connected to a big reservoir equilibrated at temperature of 298 K and the pressure of 1 bar, to allow for particle exchange in an NVT ensemble. To obtain enough statistics especially for calculating the perpendicular dielectric permittivity, the equilibrium properties are averaged over a set of 7 MD simulations each with different initial velocities and positions for a total time of 20 ns, in which the first 5 ns were discarded. Additionally, we have simulated water in capacitor channels, where uniform partial charges were assigned to the atoms of each wall to achieve external electric fields of 0.005, 0.01, 0.02, 0.05, 0.1, 0.2, 0.3, 0.5, 0.7, 1.0, and 1.5 $\mathrm{V\AA}^{-1}$.

5.2.2 Fluctuation formula for perpendicular permittivity

As mentioned before, unlike bulk, in confinement, the dielectric permittivity of a polar fluid takes a tensorial form. For a slit-channel, where the inhomogeneity is only in one direction (perpendicular to the surface, z axis), the component of the dielectric permittivity tensor spatially varies as a function of z. Using statistical mechanics and the linear response theory, the locally varying inverse perpendicular permittivity is given via the following fluctuation formula,

$$\varepsilon_{\perp}^{-1}(z) = 1 - \beta\varepsilon_0^{-1}\left[\langle p_{\perp}(z)\,P_{\perp}\rangle_0 - \langle p_{\perp}(z)\rangle_0\langle P_{\perp}\rangle_0\right], \tag{5.1}$$

where β is the inverse of thermal energy, $\langle\cdots\rangle_0$ denotes the ensemble average in the absence of an external electric field, $p_{\perp}(z)$ is the perpendicular fluid polarization density at position z, and $P_{\perp}$ is the perpendicular component of the fluid total polarization and is given by,

$$P_{\perp} = A\int_0^H p_{\perp}(z)\,dz. \tag{5.2}$$

It has been shown that in addition to dipole moment, higher order multipole moments such as quadrupole and octupole are non-negligible in calculating the perpendicular dielectric permittivity [40]. Therefore, to account for higher order multipole moments the perpendicular polarization density at position z is calculated as,

$$p_{\perp}(z) = \int_0^z \rho_{\mathrm{e}}(z')dz', \tag{5.3}$$

where $\rho_\mathrm{e}(z)$ is the fluid atomic charge density profile in the z direction, and is computed by the binning method with 0.1 Å resolution. Integrating Eq. 5.1 over the entire channel, yields the average inverse perpendicular permittivity as,

$$\varepsilon_\perp^{-1} = 1 - \frac{\left\langle P_\perp^2 \right\rangle - \left\langle P_\perp \right\rangle^2}{\varepsilon_0 V k_\mathrm{B} T}. \tag{5.4}$$

5.2.3 Electrostatic potential calculations

To compute the electrostatic potential, $\Phi(z)$, of the confined fluid in a slit channel, the Poisson equation reads as

$$\frac{d^2\Phi}{dz^2} = -\frac{\rho_e(z)}{\varepsilon_0}, \tag{5.5}$$

with the following boundary conditions:

$$\left.\frac{d\Phi}{dz}\right|_{z=0} = -\frac{\sigma_{\mathrm{c,left}}}{\varepsilon_0}, \tag{5.6a}$$

$$\left.\frac{d\Phi}{dz}\right|_{z=H} = +\frac{\sigma_{\mathrm{c,right}}}{\varepsilon_0}, \tag{5.6b}$$

$$\Phi\left(z = H/2\right) = 0, \tag{5.6c}$$

where $\sigma_{\mathrm{c,left}} = -\sigma_c$ and $\sigma_{\mathrm{c,right}} = +\sigma_c$ are the surface charge densities on the left and right wall, respectively. We note that, due to the last boundary condition (Eq. 5.6c, the electrostatic potential at any point is relative with respect to the mid-point of the channel.

5.3 Results

5.3.1 Bulk dielectric permittivity and dipolar strength

In general, solvents can be classified into two categories: protic and aprotic. The former refers to the solvents capable of forming H-bonds, whereas the latter refers to solvents which cannot accept or donate a hydrogen bond. The set of fluids considered in this study have dielectric constant (calculated from MD simulations) ranging from ∼9 (non-polar aprotic fluid such as dichloromethane) to intermediate values of ∼25 (polar protic and aprotic fluids such as methanol and acetonitrile, respectively) and to the highly polar protic fluid such as water (SPC/E) with the dielectric constant of ∼71. In addition to their technological relevance and wide range of dielectric permittivity, the selection of these solvents shows an interesting connection between bulk dielectric permittivity, proticity and dipolar strength. Assuming periodic tinfoil (conducting metal) boundary conditions, the bulk dielectric permittivity can be expressed via the following relation [202]:

$$\varepsilon_{\mathrm{b}} = 1 + 3C_{\mathrm{d}}G_{\mathrm{k}}. \tag{5.7}$$

In eq Eq. 5.7 G_{k} is the Kirkwood factor, representing the angular dipolar correlations among the dipoles (e.g. for uncorrelated dipoles G_{k} is equal to 1), and C_{d} is the dipolar strength given by,

$$C_{\mathrm{d}} = \frac{\rho_{\mathrm{b}}\mu^2}{9\varepsilon_0 k_{\mathrm{B}}T}, \tag{5.8}$$

where μ, ρ_{b}, ε_0, k_{B}, and T are the dipole moment, bulk density, vacuum permittivity, Boltzmann constant and temperature, respectively. We observe that for a similar value of dipolar strength the hydrogen-bonded liquids have a higher dielectric permittivity compared to the non-hydrogen-bonded liquids (See Appendix B, Table. B.1). This suggests larger G_{k} values, hence, stronger dipolar correlations and alignments in protic liquids. Thus, we investigate the effect of confinement on the dielectric response of both protic and aprotic solvents with distinct dipolar strengths.

5.3.2 Perpendicular dielectric permittivity of confined liquids

A typical simulation box consists of fluid molecules sandwiched between two flat graphene sheets separated by a distance, H (See Appendix B, Fig. B.1). For each channel width, we use the fluctuation formula (see Eq. 5.1) to compute the spatially varying perpendicular dielectric permittivity and average it over the entire channel width using Eq. 5.4, which makes it easier to compare with experiments and suitable for coarse-grained modeling and analytical approaches. The size of the confinement (H) investigated ranges from large channels with a well-formed bulk-like region away from the walls to smaller channels where no bulk-like region can be identified and to extremely narrow channel widths of few Angstroms, where an accurate determination of solvent dielectric constant requires high resolution experiments to reduce noise and error bar. Moreover, such small-sized carbon slit-pores of width 0.6-1 nm (less than the size of solvated ions) have exhibited anomalously high capacitance which contradicts the traditional understanding of supercapacitors [26, 203].

For all the channel widths and different fluids, we observe a reduction in perpendicular permittivity compared to the bulk value (Fig. 5.1). The reduction in permittivity with size, however, varies for different fluids. At large channel widths (with well-defined bulk-like region), the dielectric constant reduces in a nonlinear fashion from the bulk value and continues to decrease in an almost linear fashion for narrower channel widths (with no bulk-like region). For the confinement of width H_{sl} (the smallest channel width

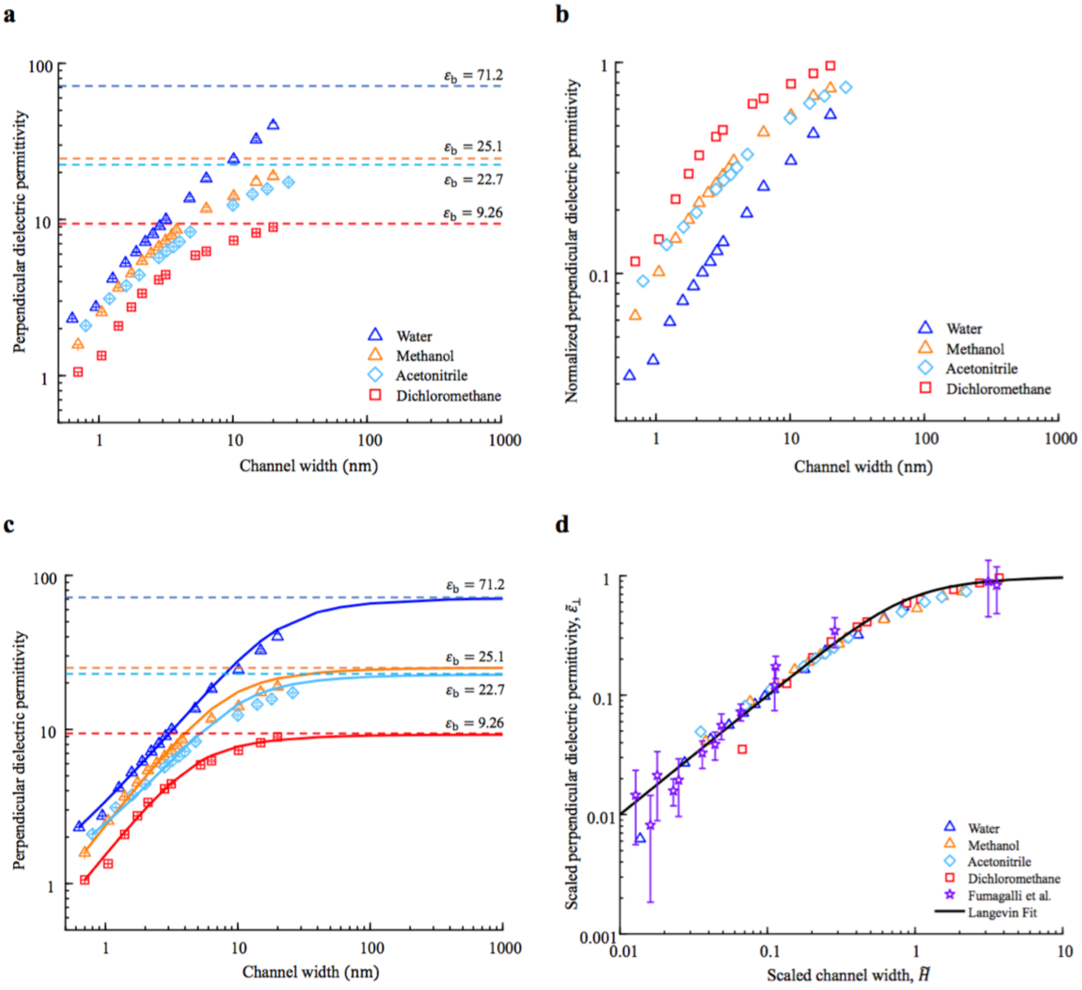

Figure 5.1: Perpendicular dielectric permittivity of confined fluids. **(a)** Perpendicular dielectric permittivity of different fluids confined in graphene slit-like channels of various widths. The bulk dielectric constant for each fluid is shown by the dashed horizontal lines and the value is denoted by ε_b. **(b)** Perpendicular dielectric permittivity normalized by the bulk dielectric constant of each fluid as a function of the channel width, i.e., $\varepsilon_\perp(H) / \varepsilon_b$. **(c)** Langevin-like behavior of the perpendicular dielectric permittivity as a function of the channel width according to Eq. 5.9. **(d)** Using proper scaling, the data for the perpendicular dielectric permittivity of confined fluids approximately collapses onto a single curve that can be described by the Langevin function. In this subfigure, the scaled perpendicular permittivity is defined as $\widetilde{\varepsilon}_\perp = \frac{\varepsilon_\perp - \varepsilon_{sl}}{\varepsilon_b - \varepsilon_{sl}}$, and the scaled channel width is given by $\tilde{H} = \frac{H - H_{sl}}{\sigma_d(\varepsilon_b - \varepsilon_{sl})}$.

considered in our simulations), where only a single layer of fluid could fit inside the channel (See Appendix B, Fig. B.2), the corresponding dielectric constant, $\varepsilon_{\mathrm{sl}}$ is exceptionally small. For some of the fluids such as dichloromethane this value is close to 1. This indicates that at small separation distances, the ability of fluids (both protic and aprotic) to screen charges normal to the surface is substantially inhibited. We note that due to the lack of electronic degrees of freedom, the high limit frequency dielectric permittivity, ε_{∞}, is equal to unity for non-polarizable force fields [204]. Thus, the value of $\varepsilon_{\mathrm{sl}}$ for all the fluids lies above ε_{∞} =1. To the best of our knowledge, with the exception of water, there are no relevant experimental studies on the variation of dielectric permittivity of non-aqueous fluids as a function of the channel width. Nevertheless, our results are in good agreement with recent experiments reported on the confined water dielectric permittivity [10]. For water, both simulations and experiments show a linear reduction in perpendicular permittivity for small channels and a nonlinear reduction from the bulk value for larger channel widths. The smallest permittivity found in experiment was ~2.1±0.2 for channel widths smaller than 2 nm. In our simulations, however, we observe such a low value of perpendicular dielectric permittivity only in sub-nanometer channels.

Our results show that the reduction in the perpendicular dielectric permittivity is not exclusive to water, rather it is a universal feature for the confined fluid systems. As a corollary, electrostatic interactions perpendicular to an interface are enhanced under confinement. In other words, the electrostatic repulsion or attraction becomes stronger between two similar or oppositely charged surfaces. This phenomenon can be very important in biology due to the polar nature of protein surfaces and their interaction with water or in energy storage applications as the dielectric permittivity of solvents can drastically impact the capacitance of a device.

5.3.3 Langevin behavior of the perpendicular permittivity

As depicted in Fig. 5.1c , the behavior of the perpendicular permittivity as a function of the channel width can be approximately modeled by a Langevin function as,

$$\varepsilon_{\perp}(H) = \varepsilon_{\mathrm{sl}} + \Delta\varepsilon \; \mathcal{L}\left(3\frac{H - H_{\mathrm{sl}}}{\sigma_{\mathrm{d}}\Delta\varepsilon}\right), \tag{5.9}$$

where $\Delta\varepsilon = (\varepsilon_{\mathrm{b}} - \varepsilon_{\mathrm{sl}})$, $\mathcal{L}(x) = \coth(x) - \frac{1}{x}$ is the Langevin function, and σ_{d} is an effective length scale which is determined from the slope at small channel widths.

In the context of dielectric theory, Langevin function has also been used to describe the orientational polarization of the system of non-interacting dipoles, the dielectric saturation effects due to the external electric field [205–207], dielectric decrement as a function of ion concentration [208, 209], and to model an effective permittivity in classical theories such as the Poisson-Boltzmann theory [210].

Table 5.1: Anomalously low perpendicular dielectric permittivity of different fluids in sub-nanometer slit channels. σ_d is the fitting parameter in the Langevin equation, λ_b is the length scale to retrieve the bulk dielectric behavior, and σ_a is the effective molecular diameter from [1].

Fluid	H_{sl}(nm)	$\varepsilon_{\mathrm{sl}}$	σ_{d}(nm)	σ_a(nm)	λ_{b}(nm)
Water	0.634	2.3146	0.3370	0.2922	1035.8
Methanol	0.700	1.5800	0.3870	0.3835	288.0
Acetonitrile	0.800	2.0900	0.5501	0.4244	344.5
Dichloromethane	0.700	1.0558	0.6318	0.5045	153.0

For small channels, especially in the limit of $H \to H_{\mathrm{sl}}$, the behavior of the perpendicular dielectric permittivity is approximately linear as a function of the channel width with the slope directly related to σ_{d} (See Appendix B, Fig. B.3). The resultant values for σ_{d} show a remarkable similarity to the effective molecular diameter of the fluids considered [1] (Table 5.1).

In addition, knowing σ_{d} for each fluid and using Eq. 5.9, we can predict the characteristic length scale, λ_{b}, for which the bulk dielectric behavior is recovered (Table 5.2). The criterion used to calculate λ_{b} was that the perpendicular dielectric permittivity at $H = \lambda_{\mathrm{b}}$ reaches 99% of ε_{b}. We found that λ_{b} ranges from hundreds of nanometers for dichloromethane, methanol, and acetonitrile to micrometers for water. Our results for water, agree well with the recent experiments [10] and previous MD simulations, showing that the effect of confinement on the dielectric response of water extends up to mesoscale dimensions.45 We emphasize that these length scales are obtained for fluids confined in the graphene slit-pores and these length scales can change as the substrate changes.

By rearranging Eq. 5.9 and plotting the scaled perpendicular dielectric permittivity, $\widetilde{\varepsilon}_{\perp} = \frac{\varepsilon_{\perp} - \varepsilon_{\mathrm{sl}}}{\varepsilon_{\mathrm{b}} - \varepsilon_{\mathrm{sl}}}$, against the scaled channel width, $\tilde{H} = \frac{H - H_{\mathrm{sl}}}{\sigma_{\mathrm{d}}(\varepsilon_{\mathrm{b}} - \varepsilon_{\mathrm{sl}})}$, it is apparent that all the data for different fluids approximately collapses onto a single curve including the experimental measurements reported in the literature for water out-of-plane dielectric permittivity [10]. This relationship between the scaled perpendicular dielectric permittivity and the scaled channel width can be modeled by the Langevin function, i.e., $\widetilde{\varepsilon}_{\perp}\left(\tilde{H}\right) = \mathcal{L}\left(3\tilde{H}\right)$.

5.3.4 Multiscale parallel-plate capacitor model

A simple capacitor consists of a dielectric medium sandwiched between two electrodes of equal and opposite charges ($\pm Q$) separated by a distance H. A capacitor can be characterized by its capacitance (C) which is a measure of the amount of charge stored for a given potential difference across its electrodes, i.e.,

$$C = \frac{Q}{\Delta\Phi} = \frac{\sigma_{\mathrm{c}} A}{\Delta\Phi}, \tag{5.10}$$

where σ_c is the electrode surface charge density, A is the surface area of the electrode, and $\Delta\Phi = \Phi_\mathrm{anode} - \Phi_\mathrm{cathode}$ with anode and cathode referring to the positive and negative electrodes, respectively. On the other hand, from a theoretical point of a view, the capacitance for a conventional parallel-plate capacitor can be written in terms of the geometry of the capacitor and the dielectric permittivity of the confined medium as,

$$C = \frac{A\varepsilon_0\varepsilon_\mathrm{r}}{H}. \tag{5.11}$$

Using Eqs. 5.10 and 5.11, the dielectric permittivity of the medium can be expressed as,

$$\varepsilon_\mathrm{r} = \frac{\sigma_\mathrm{c} H}{\varepsilon_0 \Delta\Phi}. \tag{5.12}$$

Herein, in addition to the fluctuation formula to calculate the perpendicular permittivity, we have simulated capacitor channels, where uniform partial charges, positive on the right wall ($z = H$) and negative on the left wall ($z = 0$), were assigned to the wall atoms to achieve an external electric field of strength, $E_\mathrm{ext} = \sigma_\mathrm{c}/\varepsilon_0$. Thus, by knowing the electrostatic potential of the anode and cathode, the dielectric permittivity of the confined medium, which coincides with the perpendicular dielectric permittivity (i.e., $\varepsilon_\mathrm{r} = \varepsilon_\perp$), can be obtained using Eq. 5.12. To find the electrostatic potential for a confined fluid system, we first calculated the atomic charge density profile from MD simulations and used the Poisson equation with the proper boundary conditions (Eq. 5.6) to obtain the electrostatic potential. The schematic of the entire procedure for water is shown in Figure 2a.

Compared to the fluctuation formula which is only applicable in the absence of an external electric field and requires long and tedious equilibrium simulations, Eq. 5.12 is more robust and can be used to calculate the electric-field-dependent perpendicular dielectric permittivity. However, one caveat is that it cannot be used at zero external electric field. To address this limitation and to establish verification of the results of Eq. 5.12 with the fluctuation formula, we investigated the variation of the perpendicular dielectric permittivity as a function of the electric field (Fig. 5.2c). In general, as the electric field increases the fluid dipoles get more aligned with the applied field, and thus, results in a lower dielectric permittivity. At weaker electric fields, however, it is clear that the slope plateaus indicating an almost constant dielectric permittivity. This is not surprising, as on the basis of the linear response theory, for weak enough electric fields the response of the fluid total polarization density ($p_\perp$) varies linearly with the local electric field ($E_\perp$), i.e., $p_\perp = \varepsilon_0 \left(\varepsilon_\perp - 1\right) E_\perp$. This is evident in the inset of Fig. 5.2b. It can be seen that for water, the linear regime is observed for $E_\mathrm{ext} \leq 0.2\ \mathrm{V}^{-1}$, which is consistent with prior literature for water confined in graphene channels [46]. To extract the zero field perpendicular dielectric permittivity, we used the Booth

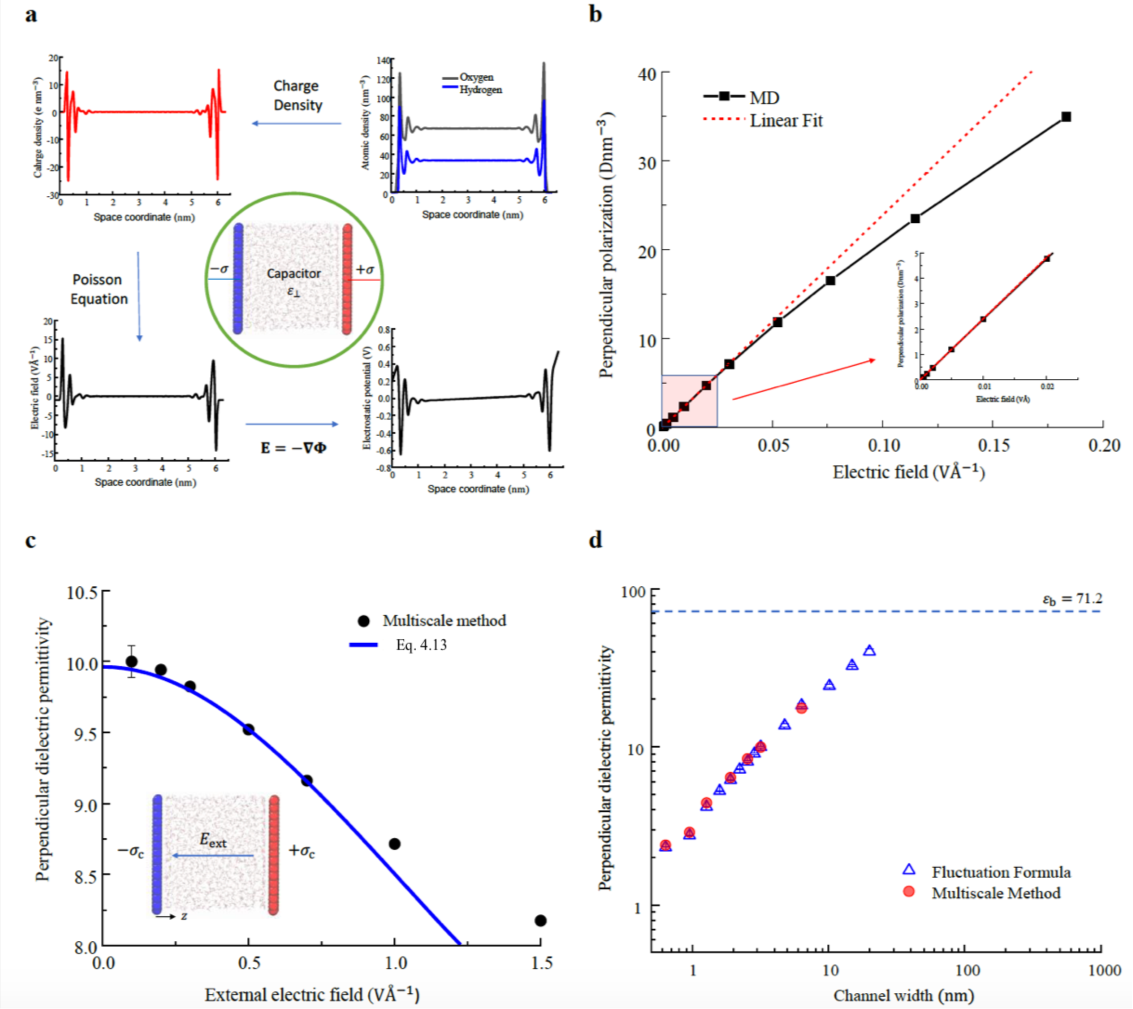

Figure 5.2: Parallel-plate capacitor multiscale method. **(a)** Schematic procedure for calculating the perpendicular dielectric permittivity of confined fluids using Eq. 5.12. The procedure is illustrated for water, where we first calculate the density of oxygen and hydrogen atoms. Multiplying by their atomic charges, we obtain the charge density profile which can be used in the Poisson equation to obtain electric field and thus the electrostatic potential required to calculate the perpendicular dielectric permittivity. **(b)** Total perpendicular polarization density ($p_\perp = P_\perp/V$, where $P_\perp$ is calculated from Eq. 5.2) of water as a function of the electric field for 3.17 nm wide channel. The inset shows the region, where the variation is almost linear and the dielectric constant is nearly independent of the electric field inside the channel. The onset of the nonlinear behavior occurs at the electric field $\sim 0.02\ V^{-1}$ ($E_{ext} = 0.2\ V^{-1}$). **(c)** Electric-field dependent perpendicular dielectric permittivity of water confined in 3.17 nm wide channel for various external electric field strengths. As shown, the direction of the applied electric field is from right to left. Circles are calculated from Eq. 5.12 and the line is the fitted curve using Eq. 5.13 with the following fitting parameters: $b = 1.78 \pm 0.03\ V^{-1}$, and $\varepsilon_\perp(0) = 9.96 \pm 0.02$ **(d)** Comparison between the water perpendicular dielectric permittivity obtained at the limit of zero electric field from the multiscale parallel-plate capacitor method versus the results obtained from the fluctuation formula.

relation [205, 206] for the electric field-dependent perpendicular dielectric permittivity,

$$\varepsilon_{\perp}\left(E_{\mathrm{ext}}\right)=n^{2}+\frac{3\left(\varepsilon_{\perp}\left(0\right)-n^{2}\right)}{bE_{\mathrm{ext}}}\mathcal{L}\left(bE_{\mathrm{ext}}\right), \tag{5.13}$$

where n is the refractive index, which is related to the infinite frequency dielectric constant by $\varepsilon_{\infty} = n^2$. In Eq. 5.13, b and $\varepsilon_{\perp}(0)$ are fitting parameters for our data and $n = 1$ due to the use of non-polarizable SPC/E forcefield. We note that eq Eq. 5.13 has been originally derived in the bulk, however, we show that (Fig. 5.2c) it can extract $\varepsilon_{\perp}$ in the limit of the zero electric field. Therefore, for each channel width, we only perform 2 non-equilibrium MD (NEMD) simulations at two distinct electric fields to obtain perpendicular dielectric permittivity via Eq. 5.12, and subsequently use Eq. 5.13 to extract the zero electric field perpendicular dielectric permittivity. The results are illustrated in Fig. 5.2d, which show a good agreement with the perpendicular dielectric permittivity obtained from the fluctuation formula. Therefore, the aforementioned multiscale method eliminates the need for long and tedious simulations required to calculate the perpendicular dielectric permittivity from the fluctuation formula. It is worth mentioning that we can further modify Eq. 5.13 to account for the dielectric saturation in the limit of very high external electric fields and consequently obtain an accurate representation of the perpendicular dielectric permittivity as a function the external electric field (See Appendix B, Fig. B.4).

5.3.5 Dipole correlations and reduced perpendicular permittivity

It is widely accepted that the low perpendicular dielectric permittivity is due to a dielectric dead layer (low permittivity interfacial region) at the fluid-solid interface [211, 212]. However, the origin of such a low dielectric layer is still debated as to whether it is intrinsic to the dielectric medium or due to the impurities on the surface.48 In either case, the existence of a dead layer will lower the overall dielectric constant, thus, having a huge impact on the capacitance of the medium [173, 213]. It has been shown for water that the reduction in permittivity is attributed to the favorable in-plane hydrogen-bond network at the solid surface, which makes it difficult for molecules to re-orient in the perpendicular direction and respond to the external field.49 However, our results indicate that not only protic fluids such as water or methanol (hydrogen bonding fluids) but also aprotic fluids exhibit a low out-of-plane dielectric permittivity under confinement, suggesting that the underlying mechanism for the reduction in permittivity is not just due to the hydrogen bond network effect in the interfacial layer (IFL). Since the main contribution to the static dielectric permittivity of polar fluids is the orientational polarizability (compared to the electronic polarizability) [214], and the dominant term is the dipole polarization, we investigate the in-plane dipole orientational correlations in the first fluid density layer (interfacial layer) adjacent to the wall (See Appendix B, Fig. B.5). As depicted in Fig. 5.3a-d,

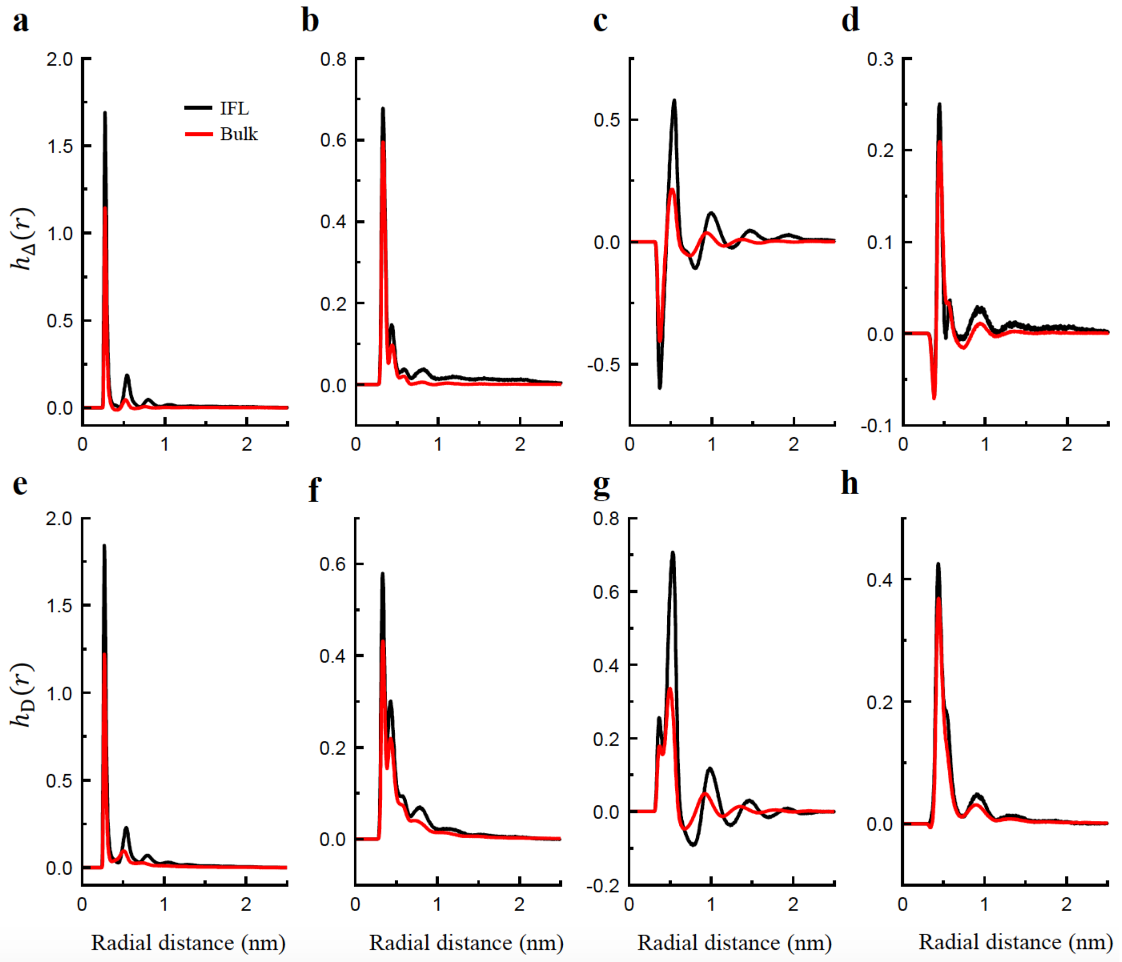

Figure 5.3: Dipolar correlations for water (a,e), methanol (b,f), acetonitrile (c,g), and dichloromethane (d,h). The top row shows the dipole-dipole pair correlation function and the bottom row shows the angular dependence of the dipole-dipole interaction energy in bulk (red color) and in the interfacial layer next to the graphene surface (black color) as a function of the separation distance r. It is important to note that in IFL the distance between the dipoles lies in the xy plane (parallel to the surface). Therefore, the separation distance is the in-plane radial distance, *i.e.*, $\boldsymbol{r}_{||} = (x, y)$.

for all the fluids considered, compared to the bulk, the in-plane dipole-dipole correlation, $h_\Delta(r)$ (Eq. 4.32) is enhanced, showing the tendency of the dipoles to lay parallel to the graphene surface. Such a preferred orientation was reported for polar liquids on graphene [214].

This preferred orientation can be understood by analyzing the in-plane dipole-dipole electrostatic energy of the interfacial layer, which can be written as,

$$U_{\mathrm{elec,dd}} = -\frac{A L_{\mathrm{IFL}}^2 \rho_{\mathrm{IFL}}^2}{2\varepsilon_0}\mu^2 \int_0^\infty \frac{h_{\mathrm{D}}\left(r_{\|}\right)}{r_{\|}^2} dr_{\|}, \tag{5.14}$$

where h_{D} represents the angular dependence of the dipole-dipole interaction energy (Eq. 4.37), $r_{\|}$ is the

Table 5.2: The dipole moment squared, bulk and the interfacial layer densities, and the in-plane dipole-dipole electrostatic potential for various fluids.

Fluid	$\mu^2(\mathrm{D}^2)$	ρ_b (nm^{-3})	ρ_IFL (nm^{-3})	$U_\mathrm{dd,elec}(\mathrm{kJ\ mol}^{-1})$
Water	5.5225	33.40	62.24	-1475.92
Methanol	5.4820	14.58	39.04	-281.09
Acetonitrile	15.1632	11.47	26.88	-316.04
Dichloromethane	4.9131	8.96	24.59	-52.53

in-plane separation distance between the dipoles, L_IFL is the width of the interfacial layer, and ρ_IFL is the density of the molecules in the interfacial layer. Fig. 5.3e-h shows the correlation function $h_\mathrm{D}(r)$ for different fluids. Similar to the in-plane dipole-dipole correlation, $h_\mathrm{D}(r)$ is enhanced next to the interface and it is dominantly positive, suggesting that the preferred alignment of dipoles is to lower the dipole-dipole interaction energy. In addition to $h_\mathrm{D}(r)$, we expect that the density and the dipole moment play an important role as they explicitly enter Eq.5.14. Using all these parameters, we have calculated the in-plane electrostatic energy for water, methanol, dichloromethane and acetonitrile (Table 5.2). We note that water has the lowest energy followed by acetonitrile and methanol (similar values), and dichloromethane has the highest in-plane dipole-dipole electrostatic energy. This explains the anomalous reduction in the perpendicular permittivity and the order to which this reduction occurs relative to the bulk permittivity, $\varepsilon_\perp(H)/\varepsilon_\mathrm{b}$ (Water $>$ Methanol $\approx$ Acetonitrile $>$ Dichloromethane) (Fig. 5.1b). Overall, our results show that the reduction in perpendicular dielectric permittivity ensues from the existence of confinement and the tendency of the fluid molecules to align parallel to the graphene surface. The preferred in-plane alignment of molecules lowers the dipole-dipole electrostatic interaction energy hindering the out-of-plane rotation and thus reducing the tendency to align with an external electric field acting in the normal direction (z-axis).

5.4 Summary

Till date, most of the literature on perpendicular dielectric permittivity dealt with confined water and less attention has been given to the response of other polar liquids. Many studies have shown that the perpendicular dielectric response is significantly reduced as a result of confining water molecules. This work goes further by demonstrating that the reduction in the perpendicular permittivity is a universal feature for both protic and aprotic fluids. The physical origin of this reduction was attributed to the low dielectric response of the interfacial layer due to the preferred in-plane alignment of the fluid molecules' dipole moments. Such an alignment lowers the in-plane dipole-dipole electrostatic energy and therefore, restricts the molecular rotations normal to the surface. Furthermore, our results reveal that for narrow confinements with no bulk-like region in the middle of the channel, perpendicular permittivity scales linearly as a function of the channel width and the slope is proportional to an effective length scale which is close to the fluid's molecular diameter. As the bulk-like region begins to form inside the channel, nonlinear effects are observed. We showed that such a behavior can be modeled by the Langevin function. Moreover, using the Langevin function we predict the length scale beyond which the fluid can be treated as bulk in terms of its dielectric properties. We found that depending on the fluid, the channel width that recovers the bulk dielectric response varies from hundreds of nanometers for less polar molecules such as dichloromethane to micrometers for fluids such as acetonitrile, methanol and water. Our results for water are in qualitative agreement with the recent capacitance microscopy experiments in which the length scale to retrieve bulk-like dielectric permittivity was estimated to be beyond 100 nm.

Under extreme confinement (sub nanometer channels), the perpendicular permittivity of the fluids is anomalously suppressed to values as low as < 2.5. This indicates that the molecules primarily take a planar orientation on the surface with very small out-of-plane dipolar components. For water the smallest value of perpendicular permittivity was found to be $\sim$2.3 in good agreement with the experimental value of $\sim$2.1 [10]. Using the multiscale parallel-plate capacitor model, we have also studied the perpendicular response of water dielectric permittivity as a function of the external electric field. In the limit of a vanishingly small electric field, our results coincide with the perpendicular dielectric permittivity obtained from the statistical mechanics approach (fluctuation formula). Furthermore, we observed a non-monotonic decrease in the out-of-plane dielectric permittivity as a function of electric field. We showed that such a dielectric decrement can be adequately modelled by the Booth relation.

We believe our findings will provide significant implications for theoretical assessment of both protic and aprotic solvents next to an interface, understanding long-ranged electrostatic interactions in biological systems, and understanding the solvation chemistry in polar fluids. Finally, our predictions for the reduction in perpendicular permittivity of both protic and aprotic fluids in confined slit channels paves way for new experimentation.

Chapter 6

Confinement-induced enhancement of dielectric permittivity

6.1 Introduction

As mentioned in Chapter 5, unlike the bulk, the dielectric response of fluids under confinement is neither isotropic nor a scalar. It is a second rank tensor, whose components vary in different spatial directions and exhibit an anisotropic behavior (e.g. perpendicular, $\varepsilon_{\perp}$, or parallel, $\varepsilon_{\parallel}$, to a flat interface) [39, 40, 188, 191]. Understanding such an anisotropic behavior is very important since different applications requires the use of specific component of dielectric permittivity tensor. For example, determining the capacitance of EDLCs requires the knowledge of perpendicular dielectric permittivity [46], which was investigated in detail in Chapter 5. Whereas, in applications such as nanofiltration and water desalination [176, 177], where the transport of species are mainly parallel to the pore surface, the parallel component becomes the most relevant quantity in the dielectric permittivity tensor. From both MD simulations and experiments, there has been a surge of interest in studying the dielectric permittivity of confined fluids, in particular, water. Most of these efforts have focused on the perpendicular dielectric permittivity. We showed that the perpendicular dielectric permittivity is significantly reduced near the interface and the reduction is universal for both protic and aprotic fluids. On the other hand, the parallel dielectric permittivity is enhanced near the interfaces and shown to roughly follow the density variations inside the confinement [40]. The results reported from the MD simulations are mostly exclusive to confined water and the relation between the parallel permittivity and density profile is not unambiguous and rigorously derived [116, 166]. Moreover, the molecular origin of the enhancement of parallel permittivity has been investigated for water and been associated with excluded volume and hydrogen bonding network [166, 215]. However, this is an open question, when it comes to aprotic fluid incapable of forming Hydrogen bonds.

In this chapter we use extensive MD simulations with cumulative time of 1 μs to study parallel permittivity variations of both protic and aprotic fluids confined in 2D graphene slit-like channels. Starting from the fluctuation formula and using statistical mechanics, we show that in addition to the density variations, dipolar correlations at the interface plays an important role in enhancing the parallel dielectric permittivity depending on the fluid polarity and degree of the confinement. We furthermore, investigate the molecular origin for such enhancement. Finally, we study the parallel dielectric permittivity inside extreme confinement, where only a single layer of fluid could fit inside the channel. We show that such confined geometries can give rise to a colossal parallel dielectric permittivity, which could be serve as a probe to identify a transition into a highly ordered structure.

6.2 Density and parallel permittivity relationship

For a slit-channel, where the inhomogeneity is only in one direction (perpendicular to the surface, z axis), the parallel dielectric permittivity spatially varies as a function of z. Using statistical mechanics and the linear response theory the locally varying parallel dielectric permittivity is given via the following fluctuation formula [39],

$$\varepsilon_{\parallel}(z) = 1 + \frac{\beta\varepsilon_0^{-1}}{2}\left[\left\langle \boldsymbol{p}_{\parallel}(z) \cdot \boldsymbol{P}_{\parallel}\right\rangle - \left\langle \boldsymbol{p}_{\parallel}(z)\right\rangle \cdot \left\langle \boldsymbol{P}_{\parallel}\right\rangle\right], \tag{6.1}$$

where $\boldsymbol{p}_{\parallel} = (p_x, p_y)$ is the in-plane fluid polarization density vector at position z, and $\boldsymbol{P}_{\parallel}$ is the parallel component of the fluid total polarization vector. Unlike the perpendicular dielectric permittivity higher order multipole moments such as quadrupole and octupole are negligible in calculating the parallel dielectric permittivity [40]. Therefore, the total parallel polarization and the local parallel polarization density can be calculated from MD using the dipole moments, respectively,

$$\boldsymbol{P}_{\parallel} = \sum_{j=1}^{N} \boldsymbol{\mu}_{\parallel,j} \tag{6.2}$$

$$\boldsymbol{p}_{\parallel}(z_i) = \frac{1}{A\Delta z}\sum_{j=1}^{N(z_i)} \boldsymbol{\mu}_{\parallel,j}, \tag{6.3}$$

where $\boldsymbol{\mu}_{\parallel,j}$ is the parallel component of the j^{th} dipole, N is the total number of fluid molecules, $N(z_i)$ represents the number of molecules located at $z = z_i$, and z_i is the location of the i^{th} layer (bin) of thickness Δz inside the slit channel. Due to the homogeneity in the x-y plane, the contribution of the second term in brackets in Eq. 6.1 is negligible. Therefore, using definitions provided in Eqs. 6.2 and 6.3, we arrive at,

$$\varepsilon_{\parallel}(z_i) = 1 + \frac{\beta\varepsilon_0^{-1}}{2A\Delta z}\left[\sum_{j=1}^{N(z_i)} \left\langle \mu_{\parallel,j}^2 \right\rangle + \sum_{j=1}^{N(z_i)} \sum_{k\neq j}^{N} \left\langle \boldsymbol{\mu}_{\parallel,j} \cdot \boldsymbol{\mu}_{\parallel,k}\right\rangle\right]. \tag{6.4}$$

In equation Eq. 6.4 the first summation is the dipole-dipole self-correlation within a layer the and second summation is the cross-correlation between dipoles of the i^{th} layer and the entire system. We can further rewrite equation Eq. 6.4 as

$$\varepsilon_{\parallel}\left(z_i\right) = 1 + \frac{\rho\left(z_i\right)\left\langle \mu_{\parallel}^2 \right\rangle}{2\varepsilon_0\ k_B T}\left(1 + \int \rho\left(z_i\right) h_{\Delta}\left(r, z_i\right) d\boldsymbol{r}\right), \tag{6.5}$$

where $\rho\left(z_i\right)$ is the density at the location z_i, $\boldsymbol{r}$ is the radial distance vector with the magnitude of r, and $h_{\Delta}(r, z_i)$ is the z-dependent parallel dipole-dipole correlation function and is defined as,

$$h_{\Delta}\left(r, z_i\right) = \frac{1}{N(z_i)\rho(z_i)}\left\langle \sum_{j=1}^{N(z_i)} \sum_{k\neq j}^{N} \widehat{\boldsymbol{\mu}}_{\parallel,\mathrm{j}} \cdot \widehat{\boldsymbol{\mu}}_{\parallel,\mathrm{k}}\ \ \delta\left(\boldsymbol{r} - \boldsymbol{r}_{jk}\right)\right\rangle, \tag{6.6}$$

where $\boldsymbol{r}_{jk} = \boldsymbol{r}_j - \boldsymbol{r}_k$ is the center-to-center distance between i and j dipoles and $\widehat{\boldsymbol{\mu}}_{\parallel}$ is the unit vector in the direction of $\boldsymbol{\mu}_{\parallel}$. The term in the parenthesis in Eq. 6.5 accounts for angular correlations among the dipoles and is very similar to the definition of the well-known Kirkwood g factor in the bulk, i.e., $G_{k,b}$ [136, 159]. Thus, we recast Eq. 6.5 in terms of the z-dependent Kirkwood g factor, $G_k(z)$:

$$\varepsilon_{\parallel}\left(z\right) = 1 + \frac{\rho\left(z\right)\left\langle \mu_{\parallel}^2 \right\rangle}{2\varepsilon_0\ k_B T} G_k(z). \tag{6.7}$$

Eq. 6.7 explicitly shows the relation between the parallel dielectric permittivity, density variations, and angular correlations inside slit-like confinement. On the other hand, for a homogeneous system (bulk) of polar molecules with periodic boundary conditions, the bulk dielectric permittivity is calculated from the following relation:

$$\varepsilon_b = 1 + \frac{\rho_b \left\langle \mu^2 \right\rangle G_{k,b}}{3\varepsilon_0 k_B T}, \tag{6.8}$$

with ρ_b representing the bulk density. Combining Eqs. 6.7 and 6.8 yields,

$$\varepsilon_{\parallel}^{*}\left(z\right) = \frac{3}{2}\rho^{*}\left(z\right)\frac{\left\langle \mu_{\parallel}^2 \right\rangle G_k\left(z\right)}{\left\langle \mu^2 \right\rangle G_{k,b}}, \tag{6.9}$$

where $\varepsilon_{\parallel}^{*}$ is the normalized parallel permittivity, $\frac{\varepsilon_{\parallel}(z)-1}{\varepsilon_b - 1}$ and $\rho^{*} = \frac{\rho(z)}{\rho_b}$ is the normalized density.

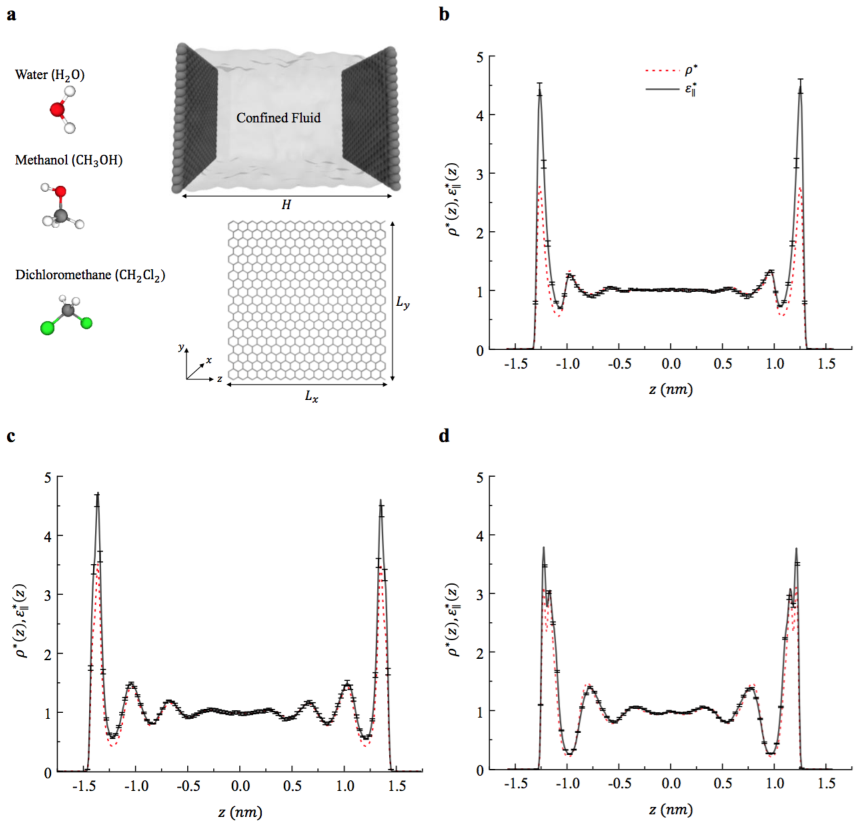

Figure 6.1: (a) Schematic illustration of the confined fluid between two graphene sheets separated by a distance H in the z direction. Lateral dimensions in the x and y directions are denoted by L_x and L_y, respectively. Oxygen (O, red), hydrogen (H, white), carbon (C, grey), and chloride (Cl, green) atoms are shown. Normalized parallel dielectric permittivity ($\varepsilon^*_\parallel(z) = \frac{\varepsilon_\parallel(z)-1}{\varepsilon_b-1}$) and density ($\rho^* = \frac{\rho(z)}{\rho_b}$) of confined fluids: (b) water ($H = 3.17\ nm$), (c) methanol ($H = 3.5\ nm$), and (d) dichloromethane ($H = 3.15\ nm$). (d) Protic (water and methanol) and aprotic (dichloromethane) fluids considered in this study.

6.3 Results

Fig. 6.1b-c compares the variation of the normalized parallel dielectric permittivity and density profile inside the confined nano channels with a well-defined bulk region (large confinement). It can be seen that for all fluids beyond the first fluid density layer (interfacial layer (IFL)) $\varepsilon^*_\parallel$ closely follows the density variations inside the channel. This indicates that except for the interfacial region, the angular correlations in the confinement behaves similar to that of the bulk regardless of the proticity of the fluid (see Eq. 6.9). In the interfacial region, however, depending on type of the fluid, the dipolar correlations deviates from the bulk and contributes to the enhancement of the parallel dielectric permittivity.

Fig. 6.2a demonstrates the contributions of both density and dipolar correlations to the interfacial parallel dielectric permittivity. For protic and more polar fluids such as water and methanol both density and dipolar correlations are responsible for enhancing the parallel dielectric permittivity adjacent to the wall. Whereas,

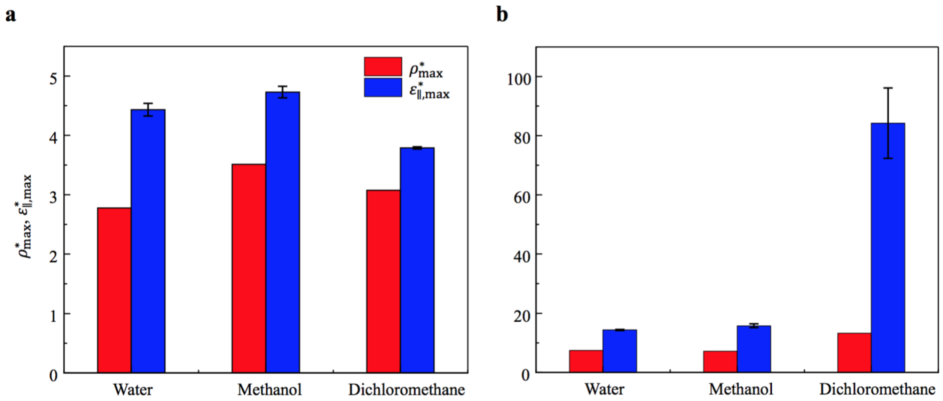

Figure 6.2: Histogram of maximum normalized density and parallel permittivity for water, methanol, and dichloromethane: (a) Wide confinements with bulk-like region in the middle (b) Extreme confinement (single layer density).

for dichloromethane, a less polar and aprotic fluid, the enhancement is due to high density region in the interfacial region. Thus, for such a fluid, the parallel permittivity can be obtained from the density variations inside the confinement (see Fig. 6.1d). We have also calculated the in-plane dipolar correlation in IFL (i.e. $h_{\Delta}\left(r_{\parallel}\right)$ calculated from Eq. 6.6 with N replaced by $N(z_{IFL})$ and $\boldsymbol{r}_{\parallel} = (x, y)$) to investigate the effect of interface on the planar dipolar correlation.

Looking closely at Fig. 6.3b-c, one can see higher in-plane dipolar correlation in IFL for more protic and polar fluids (water $>$ methanol $>$ dichloromethane). This not only corroborates the notion of hydrogen bonding network increases the parallel dielectric permittivity [215, 216], but also reveals a more underlying explanation for enhancement of parallel dielectric permittivity which is a preferred alignment of the dipoles parallel to the graphene sheet (see the Appendix C, Figs. C.1-C.3).

As shown in Fig. 6.3a-c, we also study fluids under extreme confinement characterized by a single layer density (SL). Due to the degree of the confinement, the fluid molecules arrange themselves in a condensed single layer sheet creating a high density layer with more ordered in-plane structure compared to the bulk (see the Appendix C, Fig. C.4). We observe huge enhancement factors of ∼15, 16, and 85 in parallel dielectric response of water, methanol, and dichloromethane, respectively, compared to their bulk dielectric constant. Due to the single layer arrangement, the relevant angular correlation is the in-plane parallel dipole-dipole correlation. Looking at Fig. 6.2b, it appears that the role of in-plane dipolar correlation becomes more prominent when fluid molecules acquire single layer arrangement inside the confinement. Dipolar correlation analysis show that the extreme confinement enhances the in-plane dipolar correlations (see Fig. 6.3d-f), to the extent that an aprotic less polar molecule such as dichloromethane exhibit an abnormally colossal parallel dielectric permittivity of 85 times higher than its bulk dielectric constant. According to Eq. 6.9

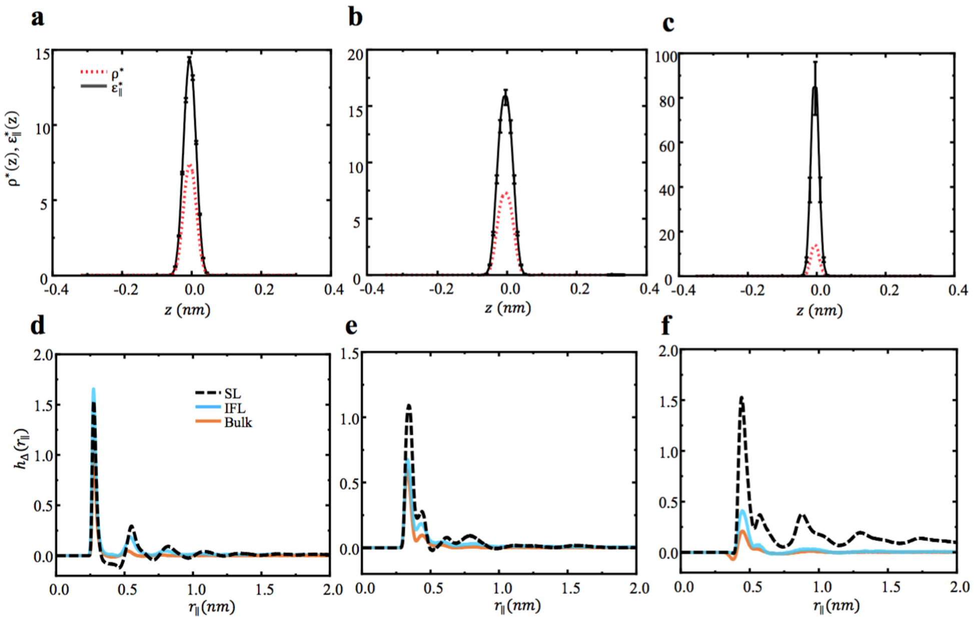

Figure 6.3: (a-c) Normalized density and parallel permittivity distribution of water (a), methanol (b), and dichloromethane (c) under an extreme confinement (single layer density). Dipole-dipole in-plane pair correlation functions of bulk , IFL, and confined single layer water, methanol, and dichloromethane depicted in subplots (d), (e), and (f), respectively. It is important to note that in extreme confinement the distance between the dipoles lies in the xy plane (parallel to the surface). Therefore, the separation distance is the in-plane radial distance, i.e., $\boldsymbol{r}_{||} = (x, y)$.

and Fig. 6.2b, the density enhancement over the bulk contributes only ∼15% to the normalized parallel dielectric permittivity of dichloromethane. Whereas for dichloromethane confined in the large slit channel this contribution in the IFL is ∼86%. The role of in-plane dipolar correlation is more evident in Fig. 6.3d-f, where the correlations exhibit more oscillations and higher peaks compared to the bulk and IFL in-plane angular correlations. It can be seen that, although the layer thickness is approximately the same, the nature of the fluid in IFL inside large confinements is very different than the fluid layer in the extreme confinement. Thus, the pre-alignment parallel to the surface and ordered structural arrangement result in super permittivity inside extreme nanoconfinement (see Appendix C, Figs. C.5 and C.6). Such an abnormal enhancement can be utilized to identify the onset of liquid transition into higher ordered structures. High dielectric permittivity has also been found to significantly affect water self-dissociation next to graphene surfaces [42, 43]. Moreover, high values of permittivity can stabilize electrochemical reactions between charge species [217]. Therefore, this opens a new research direction in science and chemistry by using extreme confinement to effectively host highly charged and polarized species.

6.4 Summary

In summary, using statistical mechanics and MD simulations we show that both high density layer and dipolar correlations are responsible for the enhancement of the parallel dielectric permittivity in the interfacial region. Nonetheless, to what extent each affects the permittivity depends on the fluid polarity, proticity, and degree of the confinement. We show that beyond the interfacial region, protic and aprotic fluids exhibit bulk-like dipolar correlations. Our results reveal that under the extreme confinement the dipole-dipole correlation becomes stronger and *via* a single layer arrangement of molecules can lead to colossal values of parallel dielectric permittivity in graphene slit-like channels. We believe that such high values of permittivity can be utilized to identify the onset of liquid transition to higher ordered structures and possibly phase transition. Moreover, such a super permittivity can facilitate hosting highly charged and polarized species.

Chapter 7

Conclusions

In this thesis, we presented the EQT approach and extended it for confined fluid mixtures. We showed that the fluid-fluid correlations can be approximated by the bulk hard sphere RDF and set of correlation correction potentials. We demonstrated the EQT for mixture of hydrogen and methane atoms of different bulk composition, and showed that atomic distributions are in very good agreement with all-atom MD simulations. We further showed that using the EQT-based potentials, one can construct an expression for the excess free energy functional in the cDFT framework to obtain various thermodynamic properties, such as density, local pressure tensor, solvation force, and surface tension. We found that our theoretical predictions compare well with the MD simulations, showing that the EQT-cDFT is a promising approach to obtain thermodynamic properties of confined fluid mixtures.

To apply EQT for polar liquids, we used a hierarchical coarsening approach and obtained CG potentials for polar liquids using an extended dipole model that reproduces RDF, diffusion coefficient and dielectric permittivity in the bulk. Using the CG potentials, we showed that CGMD results are in good agreement with the underlying all-atom MD simulations. Coupling EQT with Poisson equation, we showed that the Langevin dipole approach used in Refs [37, 38] is not able to capture water orientation polarization inside slit-like channels. The reason behind this is the incorrect dielectric permittivity obtained from the Langevin dipole approximation. Therefore, we studied in detail the dielectric permittivity tensor of polar liquids under confinement using extensive MD simulations. We found that the out-of-plane (perpendicular to the surface of graphene) component of dielectric permittivity is suppressed significantly in the presence of an interface. This feature is rather universal and observed for both protic and aprotic fluids. The physical origin of this reduction was attributed to the low dielectric response of the interfacial layer due to the preferred in-plane alignment of the fluid molecules' dipole moments. Furthermore, our results reveal that in sub-nanometer confinements the perpendicular permittivity of the fluids is anomalously suppressed to values as low as < 2.5. Moreover, we develop a multiscale parallel-plate capacitor model to predict the perpendicular permittivity of polar liquids for confinement ranging from only few angstrom to micrometer in width.

Finally, we studied the enhancement of parallel dielectric permittivity of polar liquids next to a graphene surface. Using statistical mechanics, we arrived at an expression that explicitly relates the parallel permittivity to the dipolar correlations and density variations inside the confinement. We showed that both high density layer and dipolar correlations are responsible for the enhancement of the parallel dielectric permittivity in the interfacial region. Nonetheless, to what extent each affects the permittivity depends on the fluid polarity, proticity, and degree of the confinement. Our findings revealed that under the extreme confinement the dipole-dipole correlation becomes stronger and a single layer arrangement of molecules can lead to colossal values of parallel dielectric permittivity in graphene slit-like channels. We believe that such high values of permittivity can be utilized to identify the onset of liquid transition to higher ordered structures and possibly phase transition.

Appendix A

Derivative of dielectric permittivity w.r.t A_c

For a bulk system with periodic boundary condition, the dielectric permittivity can be calculated as,

$$\varepsilon_r = 1 + \frac{\langle \boldsymbol{M}^2 \rangle}{3\varepsilon_0 V k_B T}, \tag{A.1}$$

where the total dipole moment squared can be expressed in terms of the Kirkwood correlation factor, G_k:

$$\langle \boldsymbol{M}^2 \rangle = N\mu^2 G_k. \tag{A.2}$$

In the CG model, we scale the all-atom charges via a factor A_c. Thus, using Eq. A.2, the total dipole moment square for the CG system can be written as,

$$\langle \boldsymbol{M}^2 \rangle = N A_c q^2 G_k. \tag{A.3}$$

Hence, the derivative of the dielectric permittivity w.r.t. A_c can be written as,

$$\frac{\varepsilon_r}{A_c} = \frac{N q^2 G_k}{3\varepsilon_0 V k_B T}. \tag{A.4}$$

Using Eqs. A.1, A.3, and A.4, we arrive at

$$\frac{d\varepsilon_{r,CG}}{dA_c} = \frac{\varepsilon_{r,CG} - 1}{A_c}. \tag{A.5}$$

Appendix B

A Universal Reduction in Dielectric Response of Confined Fluids

Table B.1: Bulk dielectric permittivity, Kirkwood factor, and dipolar strength. For similar values of dipolar strength (C_d) the aprotic fluids have higher bulk dielectric permittivity (ε_b). This indicates that the Hydrogen bonding network in protic fluids enhances the orientational correlations in such fluids compared to the aprotic fluids.

Fluid	C_d	G_k	ε_b
Water	6.259	3.917	71.200
Methanol	2.691	3.010	25.135
Acetonitrile	5.902	1.236	22.733
Dichloromethane	1.493	1.857	9.260

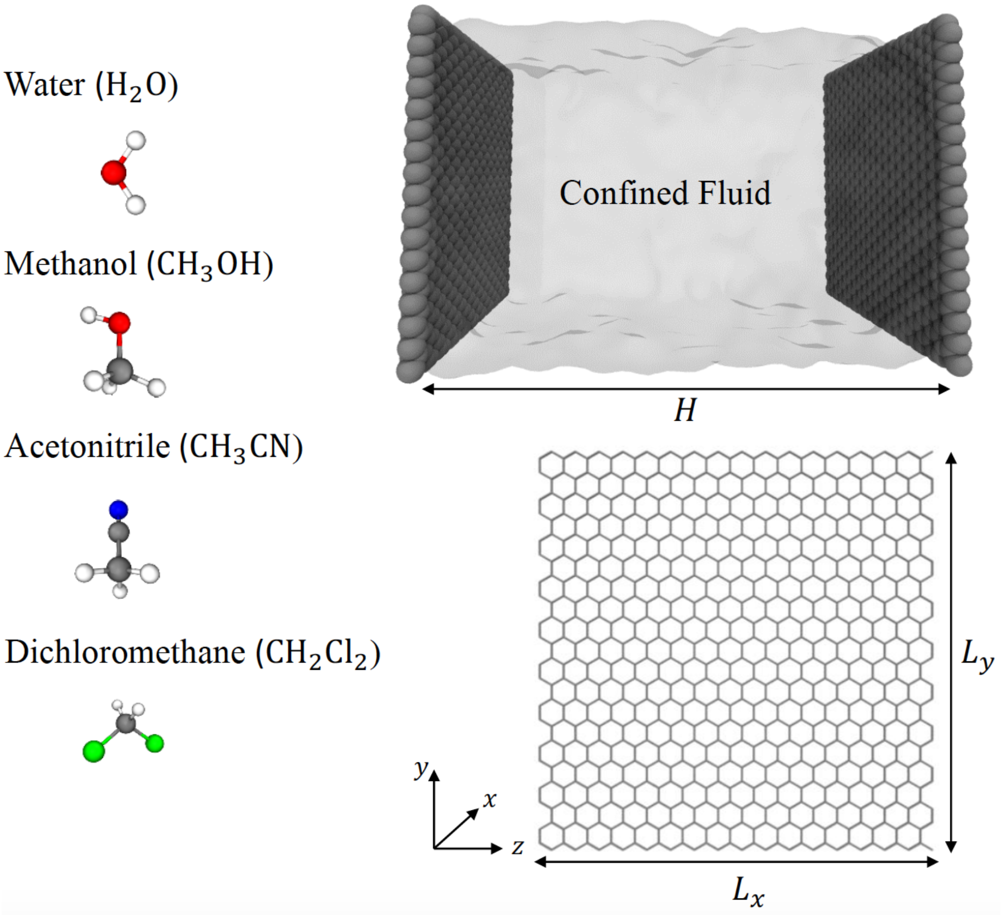

Figure B.1: Molecular dynamics simulation setup and various fluids. Protic (water and methanol) and aprotic (acetonitrile and dichloromethane) fluids considered in this study. Oxygen (O, red), hydrogen (H, white), carbon (C, grey), nitrogen (N, blue), and chloride (Cl, green) atoms are shown. On the right is the schematic illustration of the confined fluid between two graphene sheets separated by a distance H in the z direction. Lateral dimensions in the x and y directions are denoted by L_x and L_y, respectively.

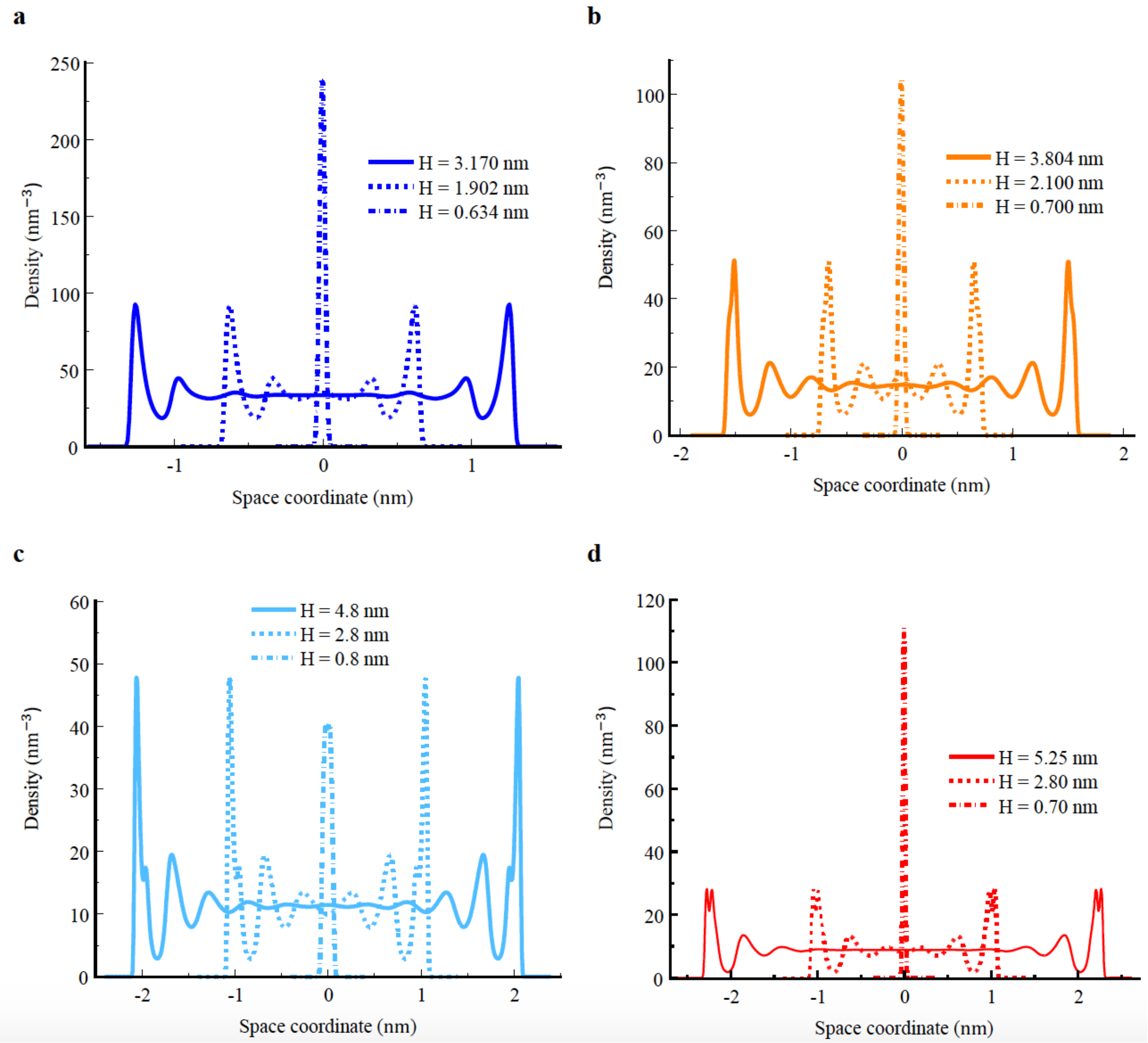

Figure B.2: Center-of-mass (COM) density variation of confined fluids in slit-like graphene channels of various widths. We have selected three slit channels for each fluid to demonstrate a large enough confinement with a well-defined bulk density away from the graphene walls, a narrow confinement with no bulk-like region in the center of the channel, and a sub-nanometer channel that only allows a single density layer formation inside the channel. In the figure, labels (a), (b), (c) , and (d) correspond to water, methanol, acetonitrile, and dichloromethane COM densities, respectively.

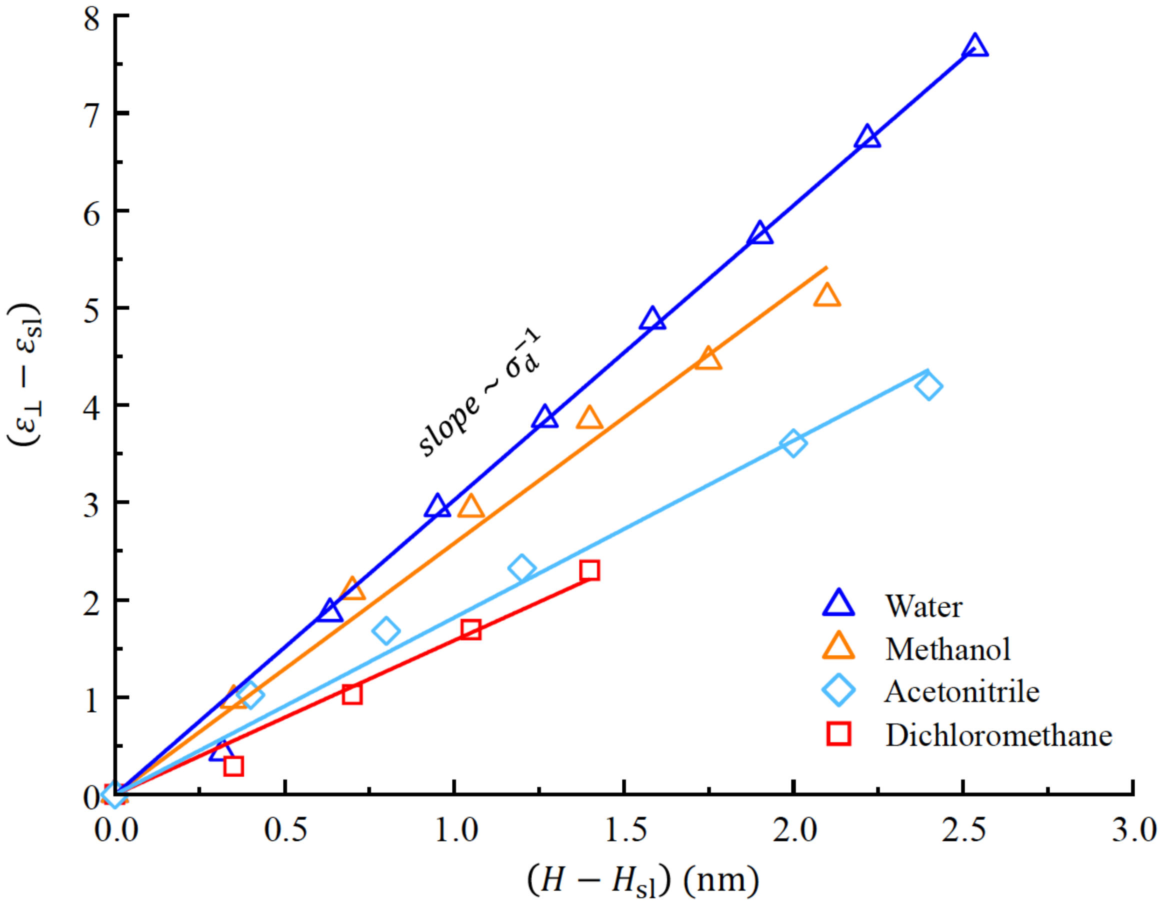

Figure B.3: Linear variation of perpendicular dielectric permittivity as a function of the channel width. As the channel width becomes smaller, approaching the limit where only a single layer of fluid can be fit inside the channel (H_{sl}), the perpendicular dielectric permittivity decreases in a linear fashion to a limiting value of ε_{sl}. Thus, for all the fluids considered in this study, we found a linear relationship between the perpendicular dielectric permittivity and the channel width whose slope is proportional to the inverse of a characteristic length scale, σ_d. We observe that the linear trend for extreme confinements, where no bulk-like region is formed in the middle of the channel. The onset of the bulk-like region formation for water, methanol, acetonitrile, and dichloromethane occurs in channel widths of ~ 3.17 nm, 3.804 nm, 3.5 nm, and 2.8 nm, respectively.

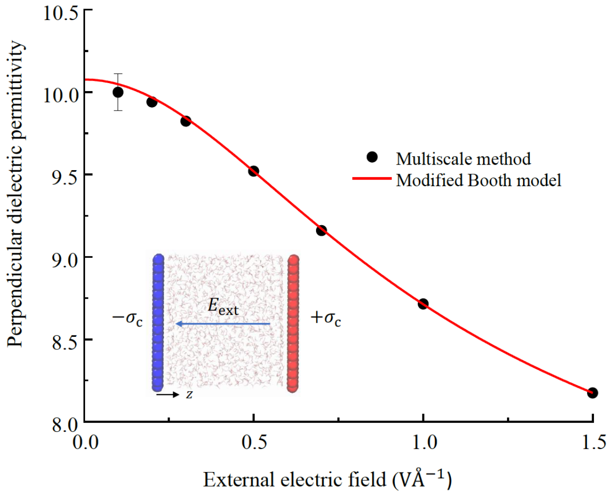

Figure B.4: Electric field dependent perpendicular dielectric permittivity. Filled circles are results from the parallel-plate capacitor model, Eq. 5.12. The red line is the modified Booth model, $\varepsilon_\perp(E_{\text{ext}}) = \varepsilon_{\perp,st} + \frac{3(\varepsilon_\perp(0) - \varepsilon_{\perp,st})}{bE_{\text{ext}}}\mathcal{L}(bE_{\text{ext}})$, fitted to the filled circle data. All the parameters in the modified Booth model are the same as in Eq. 5.13 in the main text, except that n^2 is not unity anymore and is replaced by a fitting variable $\varepsilon_{\perp,st}$,which represents the perpendicular dielectric permittivity in the limit of very high external electric fields, i.e., $E_{\text{ext}} \to \infty$. Therefore, using the modified Booth formula, we capture the trend of the perpendicular dielectric permittivity for both low and high external electric fields. The data shown in the figure is for water confined in the 3.17 nm wide channel, and the resultant fitting parameters of the modified Booth model are: $b = 2.55$ V^{-1}, $\varepsilon_{\perp,st} = 6.52$, and $\varepsilon_\perp(0) = 10.076$. The value of the perpendicular dielectric permittivity is in a very good agreement with the prediction of Eq. 5.12 and the fluctuation formula.

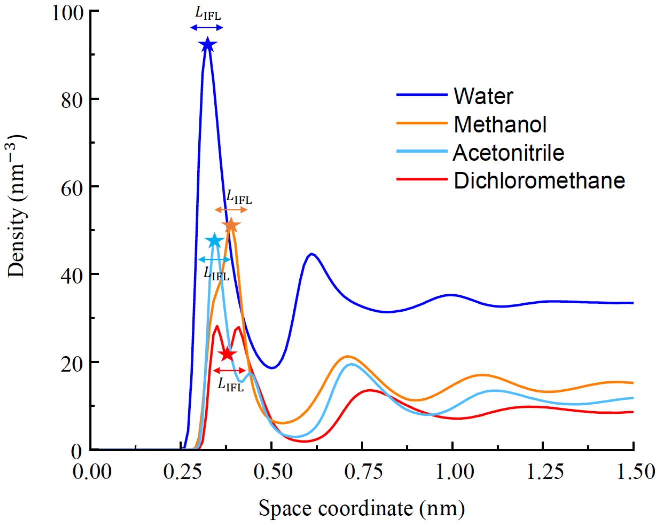

Figure B.5: Density profile and the marked interfacial layer next to the graphene surface. The stars showing the center of interfacial layer of width L_{IFL}. The interfacial slabs are centered at the locations marked in the figure with a thickness of $L_{IFL} = 1\mathring{A}$ to avoid interference of atoms from the adjacent layers.

Appendix C

Confinement-induced enhancement of dielectric permittivity

C.1 Orientation Profiles and Angular Distributions

To assess the alignment and orientation of the molecules next to the graphene surface, we have plotted the angular distribution of molecules in the IFL (Fig. C.1) and calculated the average cosine of dipole orientation (Fig. C.2), cosθ (z), where θ is defined as an angle between the positive z axis and the fluid dipole moment vector as shown in Fig. C.2. By looking at Figs. C.1 and C.2, we observe that the majority of water and methanol molecules tend to lie in the x-y plane next to the interface. In the case of dichloromethane, there are two preferred alignments of dipoles in the IFL region. Adjacent to the wall ($0 < z < 3.5$ Å), the molecules are aligned parallel to the surface, while the dipoles of the next layer are perpendicular to the wall. This gives rise to the formation of to two sublayers within the first density layer of dichloromethane next to the graphene (Fig. C.3).

C.2 In-plane Radial Distribution Function (RDF)

The in-plane RDF, $g(r_{\|})$, provides information on the planar (here, x-y plane) arrangement of molecules. It can be considered as an order parameter to identify ordering and possible phase transition close to an interface [163]. The RDFs are calculated in the slabs centered at the location of the maximum density with a thickness of 1 Å to avoid interference of atoms from the adjacent layers [162]. Figs. C.4(a-c) compares the in-plane RDFs in IFL and extreme confinement with the bulk radial distribution function. The IFL in-plane RDFs shows more structure compared to the bulk indicating higher degree of ordering in the liquid. This becomes more evident in the extreme confinement.

C.3 Parallel permittivity as an order parameter for phase transition

As illustrated in Fig. C.5, due to the degree of the confinement majority of the fluid molecules lie in the x-y plane. Depending on the fluid chemistry this planar arrangement can induce transition into higher order structures or even phase change. By looking at Figs. C.4(a) and C.4(b), we observe that both water and methanol in-plane RDFs exhibit more pronounced peaks compared to the IFL indicating higher ordering in the first, second and third coordination shells. In the case of dichloromethane (Fig. C.4(c)), we notice the emergence of a new peak located at $r = 4.4$, more peaks, and oscillations. To further analyze this, we obtained a 2D XY contour plot of the center-of-mass (COM) of dichloromethane molecules illustrated in Figs. C.6. It can be seen under extreme confinement dichloromethane forms pentagon-like structures supporting the fact that extreme confinement can push liquid into higher ordered structures with properties that are very different than not only bulk but also the interfacial region in the large confinements.

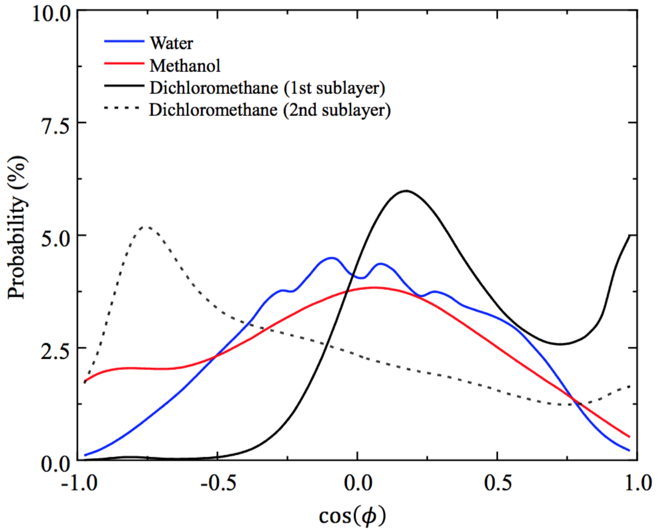

Figure C.1: Histogram of the angle distribution of water, methanol, and dichloromethane molecules within the first density layer next to the graphene interface inside the large confinement (well-defined bulk region in the middle of the channel).

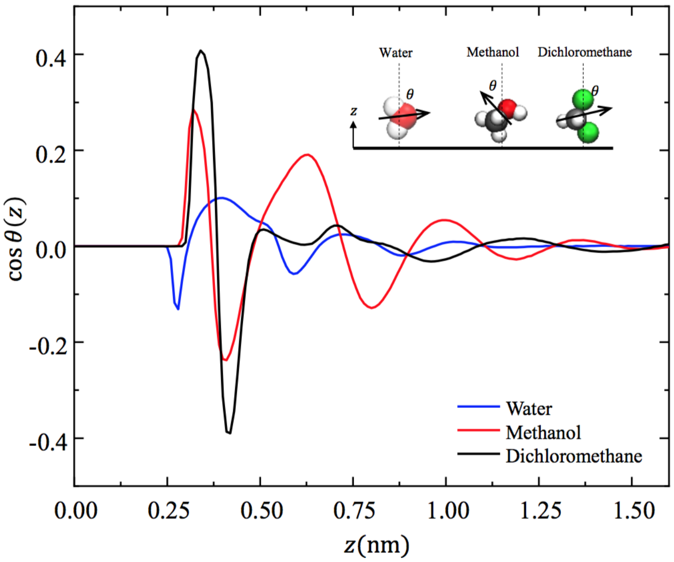

Figure C.2: Dipolar orientation profiles of water, methanol, and dichloromethane inside the 3.17 nm, 3.5 nm, and 3.15 nm channels, respectively. Oxygen (O, red), hydrogen (H, white), carbon (C, grey), and chloride (Cl, green) atoms are shown.

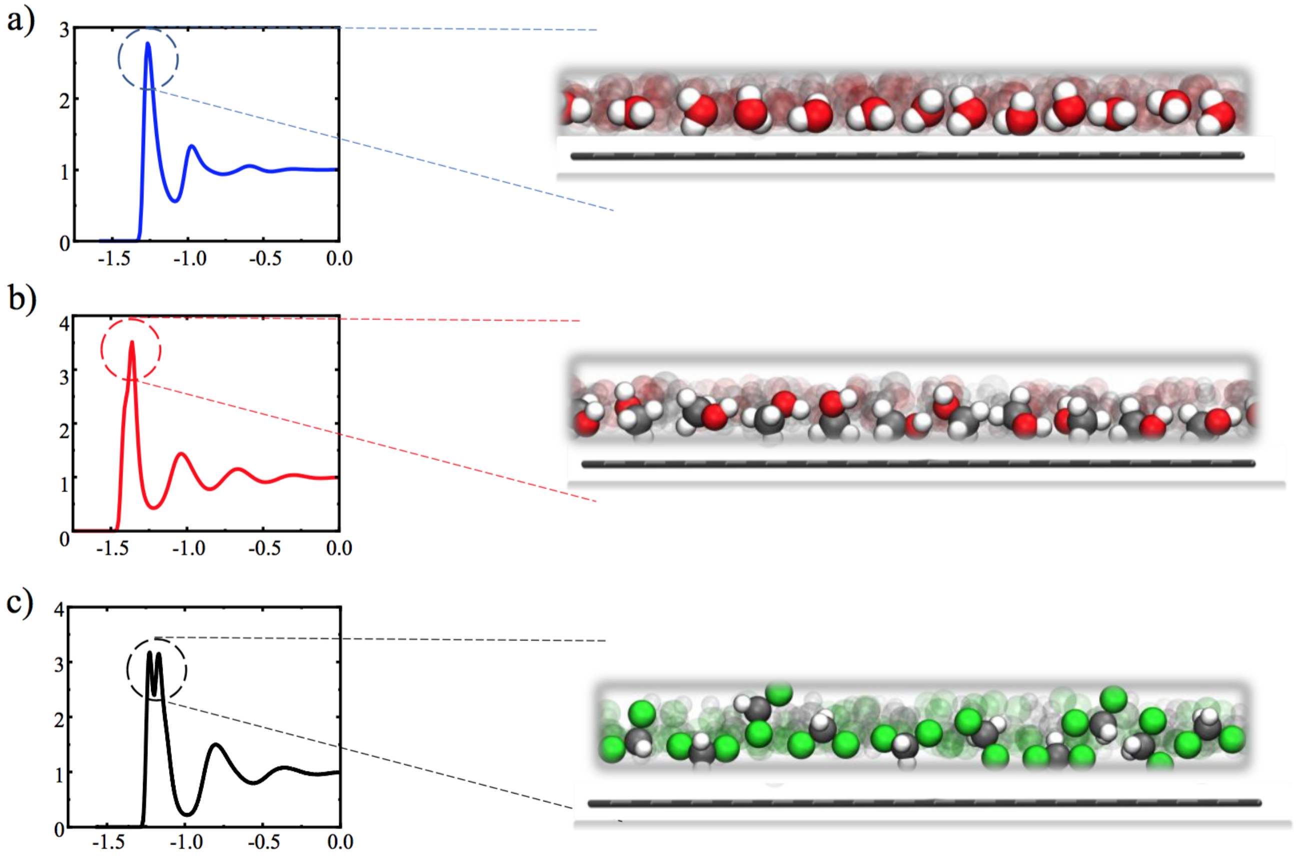

Figure C.3: Density profiles (left) and molecular arrangements (right) of water (a), methanol (b), and dichloromethane (c) on the graphene surface. Oxygen (O, red), hydrogen (H, white), carbon (C, grey), and chloride (Cl, green) atoms are shown.

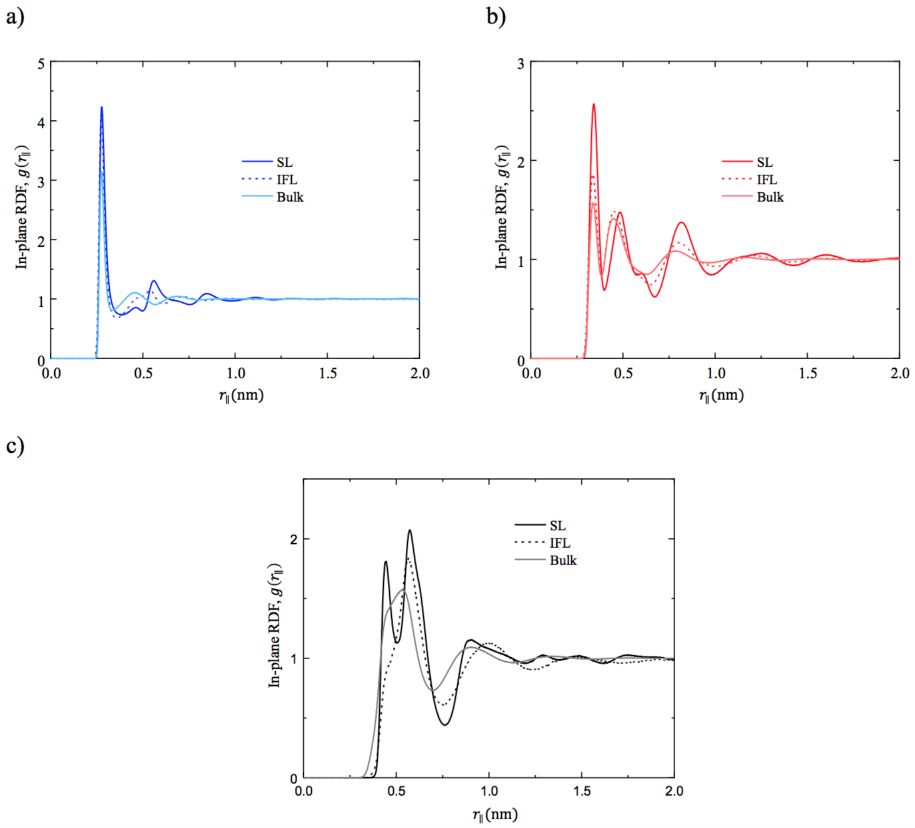

Figure C.4: (a) Water in-plane RDF (b) methanol in-plane RDF and (c) dichloromethane in-plane RDF in the interfacial region, extreme confinement and bulk, respectively.

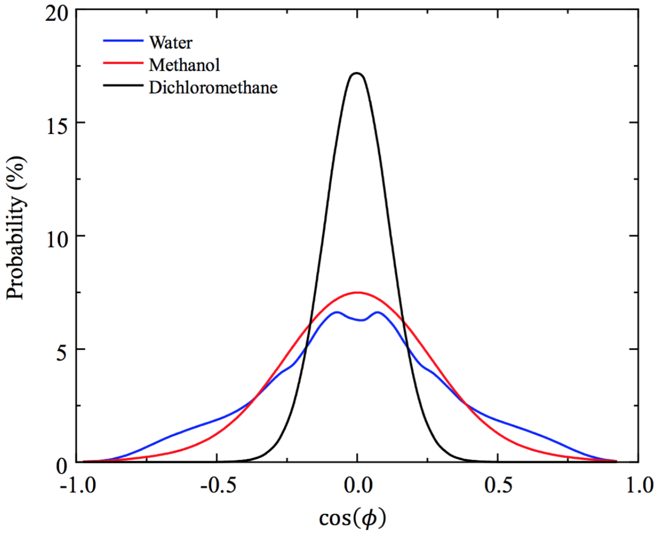

Figure C.5: Histogram of the angle distribution of water, methanol, and dichloromethane in 0.634 nm, 0.7 nm, 0.7 nm channels, respectively.

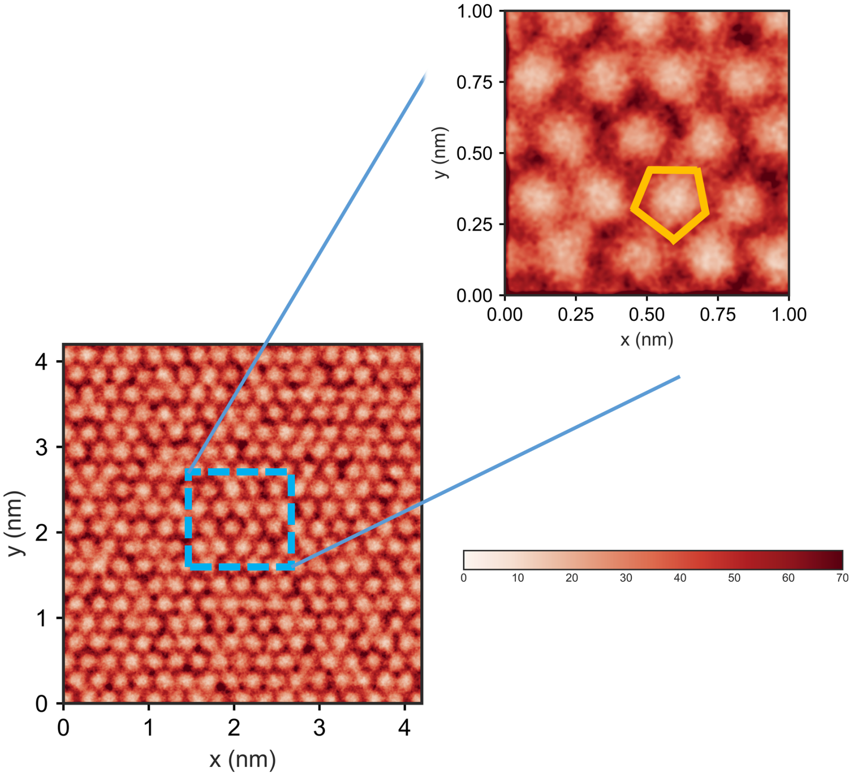

Figure C.6: 2D XY contour plot of the COM of dichloromethane molecules inside a 0.7 nm slit-like graphene channel. The inset is the zoomed-in 1×1 nm^2 contour plot showing a pentagon-like structure emerging via single layer arrangement of dichloromethane molecules.

References

[1] Dor. Ben-Amotz and Dudley R. Herschbach. Estimation of effective diameters for molecular fluids. *The Journal of Physical Chemistry*, 94(3):1038–1047, 1990.

[2] C Alba-Simionesco, Benoit Coasne, G Dosseh, G Dudziak, KE Gubbins, R Radhakrishnan, and MJPCM Sliwinska-Bartkowiak. Effects of confinement on freezing and melting. *Journal of Physics: Condensed Matter*, 18(6):R15, 2006.

[3] G Ali Mansoori. *Principles of nanotechnology: molecular-based study of condensed matter in small systems*. World Scientific, 2005.

[4] Clarence A Miller and Partho Neogi. *Interfacial phenomena: equilibrium and dynamic effects*, volume 139. CRC Press, 2007.

[5] Sergi Ruiz-Barragan, Daniel Munoz-Santiburcio, and Dominik Marx. Nanoconfined water within graphene slit pores adopts distinct confinement-dependent regimes. *The journal of physical chemistry letters*, 10(3):329–334, 2018.

[6] Yun Long, Jeremy C. Palmer, Benoit Coasne, Magorzata liwinska Bartkowiak, and Keith E. Gubbins. Pressure enhancement in carbon nanopores: a major confinement effect. *Physical Chemistry Chemical Physics*, 13(38):17163–17170, 2011.

[7] G Ali Mansoori and Stuart A Rice. Confined fluids: Structure, properties and phase behavior. *Advances in Chemical Physics*, 156:197, 2014.

[8] Sungho Han, MY Choi, Pradeep Kumar, and H Eugene Stanley. Phase transitions in confined water nanofilms. *Nature Physics*, 6(9):685–689, 2010.

[9] Amir Barati Farimani and Narayana R Aluru. Existence of multiple phases of water at nanotube interfaces. *The Journal of Physical Chemistry C*, 120(41):23763–23771, 2016.

[10] L. Fumagalli, A. Esfandiar, R. Fabregas, S. Hu, P. Ares, A. Janardanan, Q. Yang, B. Radha, T. Taniguchi, K. Watanabe, G. Gomila, K. S. Novoselov, and A. K. Geim. Anomalously low dielectric constant of confined water. *Science*, 360(6395):1339–1342, 2018.

[11] A Barati Farimani and NR Aluru. Spatial diffusion of water in carbon nanotubes: from fickian to ballistic motion. *The Journal of Physical Chemistry B*, 115(42):12145–12149, 2011.

[12] Xingcai Qin, Quanzi Yuan, Yapu Zhao, Shubao Xie, and Zhongfan Liu. Measurement of the rate of water translocation through carbon nanotubes. *Nano letters*, 11(5):2173–2177, 2011.

[13] Jianzhong Wu. Density functional theory for chemical engineering: From capillarity to soft materials. *AIChE Journal*, 52(3):1169–1193, 2006.

[14] M. E. Suk, A. V. Raghunathan, and N. R. Aluru. Fast reverse osmosis using boron nitride and carbon nanotubes. *Applied Physics Letters*, 92:133120, 2008.

[15] Jongyoon Han, Jianping Fu, and Reto B. Schoch. Molecular sieving using nanofilters: Past, present and future. *Lab on a Chip*, 8(1):23–33, 2007.

[16] Kah Peng Lee, Tom C. Arnot, and Davide Mattia. A review of reverse osmosis membrane materials for desalinationDevelopment to date and future potential. *Journal of Membrane Science*, 370(12):1–22, 2011.

[17] N. Hilal, H. Al-Zoubi, N. A. Darwish, A. W. Mohammad, and M. Abu Arabi. A comprehensive review of nanofiltration membranes:Treatment, pretreatment, modelling, and atomic force microscopy. *Desalination*, 170(3):281–308, 2004.

[18] Caitlin Smith. Tools for drug discovery: Tools of the trade. *Nature*, 446(7132):219–222, 2007.

[19] Anahita Fathi Azarbayjani, Abolghasem Jouyban, and Sui Yung Chan. Impact of surface tension in pharmaceutical sciences. *Journal of Pharmacy & Pharmaceutical Sciences*, 12(2):218–228, 2009.

[20] B. A. Suleimanov, F. S. Ismailov, and E. F. Veliyev. Nanofluid for enhanced oil recovery. *Journal of Petroleum Science and Engineering*, 78(2):431–437, 2011.

[21] D. A. Z. Wever, F. Picchioni, and A. A. Broekhuis. Polymers for enhanced oil recovery: A paradigm for structureproperty relationship in aqueous solution. *Progress in Polymer Science*, 36(11):1558–1628, 2011.

[22] Koki Urita, Yuichi Shiga, Toshihiko Fujimori, Taku Iiyama, Yoshiyuki Hattori, Hirofumi Kanoh, Tomonori Ohba, Hideki Tanaka, Masako Yudasaka, Sumio Iijima, Isamu Moriguchi, Fujio Okino, Morinobu Endo, and Katsumi Kaneko. Confinement in carbon nanospace-induced production of KI nanocrystals of high-pressure phase. *Journal of the American Chemical Society*, 133(27):10344–10347, 2011.

[23] Peter T Cummings, Hugh Docherty, Christopher R Iacovella, and Jayant K Singh. Phase transitions in nanoconfined fluids: The evidence from simulation and theory. *AIChE journal*, 56(4):842–848, 2010.

[24] Lev D Gelb, KE Gubbins, R Radhakrishnan, and M Sliwinska-Bartkowiak. Phase separation in confined systems. *Reports on Progress in Physics*, 62(12):1573, 1999.

[25] Mohammad Asadi, Mohammad Hossein Motevaselian, Alireza Moradzadeh, Leily Majidi, Mohammadreza Esmaeilirad, Tao Victor Sun, Cong Liu, Rumki Bose, Pedram Abbasi, Peter Zapol, et al. Highly efficient solar-driven carbon dioxide reduction on molybdenum disulfide catalyst using choline chloride-based electrolyte. *Advanced Energy Materials*, 9(9):1803536, 2019.

[26] J. Chmiola. Anomalous increase in carbon capacitance at pore sizes less than 1 nanometer. *Science*, 313(5794):1760–1763, 2006.

[27] Francisco Zaera. Surface chemistry at the liquid/solid interface. *Surface science*, 605(13-14):1141–1145, 2011.

[28] Olle Bjorneholm, Martin H Hansen, Andrew Hodgson, Li-Min Liu, David T Limmer, Angelos Michaelides, Philipp Pedevilla, Jan Rossmeisl, Huaze Shen, Gabriele Tocci, et al. Water at interfaces. *Chemical reviews*, 116(13):7698–7726, 2016.

[29] Yi Liu and Toshiko Ichiye. Soft sticky dipole potential for liquid water: a new model. *The Journal of Physical Chemistry*, 100(7):2723–2730, 1996.

[30] R Qiao and NR Aluru. Ion concentrations and velocity profiles in nanochannel electroosmotic flows. *The Journal of Chemical Physics*, 118(10):4692–4701, 2003.

[31] A. V. Raghunathan, J. H. Park, and N. R. Aluru. Interatomic potential-based semiclassical theory for Lennard-Jones fluids. *The Journal of Chemical Physics*, 127(17):174701–174701–11, 2007.

[32] T. Sanghi and N. R. Aluru. A transferable coarse-grained potential to study the structure of confined, supercritical Lennard-Jones fluids. *The Journal of Chemical Physics*, 132(4):044703–044703–10, 2010.

[33] T. Sanghi and N. R. Aluru. Coarse-grained potential models for structural prediction of carbon dioxide (CO2) in confined environments. *The Journal of Chemical Physics*, 136(2):024102–024102–13, 2012.

[34] SY Mashayak and NR Aluru. Coarse-grained potential model for structural prediction of confined water. *Journal of Chemical Theory and Computation*, 8(5):1828–1840, 2012.

[35] SY Mashayak and NR Aluru. Thermodynamic state-dependent structure-based coarse-graining of confined water. *The Journal of Chemical Physics*, 137(21):214707, 2012.

[36] SY Mashayak, MH Motevaselian, and NR Aluru. An eqt-cdft approach to determine thermodynamic properties of confined fluids. *The Journal of chemical physics*, 142(24):244116, 2015.

[37] SY Mashayak and NR Aluru. Langevin-poisson-eqt: A dipolar solvent based quasi-continuum approach for electric double layers. *The Journal of Chemical Physics*, 146(4):044108, 2017.

[38] SY Mashayak and NR Aluru. A multiscale model for charge inversion in electric double layers. *The Journal of Chemical Physics*, 148(21):214102, 2018.

[39] V. Ballenegger and J.-P. Hansen. Dielectric permittivity profiles of confined polar fluids. *The Journal of Chemical Physics*, 122(11):114711, 2005.

[40] Douwe Jan Bonthuis, Stephan Gekle, and Roland R. Netz. Dielectric profile of interfacial water and its effect on double-layer capacitance. *Physical Review Letters*, 107(16), 2011.

[41] Mazen Ahmad, Wei Gu, Tihamér Geyer, and Volkhard Helms. Adhesive water networks facilitate binding of protein interfaces. *Nature Communications*, 2(1), 2011.

[42] Daniel Muñoz-Santiburcio and Dominik Marx. Nanoconfinement in slit pores enhances water self-dissociation. *Physical Review Letters*, 119(5), 2017.

[43] Yamila A. Perez Sirkin, Ali Hassanali, and Damián A. Scherlis. One-dimensional confinement inhibits water dissociation in carbon nanotubes. *The Journal of Physical Chemistry Letters*, 9(17):5029–5033, 2018.

[44] Martial Duchamp, Kyumin Lee, Benjamin Dwir, Jin Won Seo, Eli Kapon, László Forró, and Arnaud Magrez. Controlled positioning of carbon nanotubes by dielectrophoresis: Insights into the solvent and substrate role. *ACS Nano*, 4(1):279–284, 2010.

[45] Vikram Jadhao, Francisco J. Solis, and Monica Olvera de la Cruz. Simulation of charged systems in heterogeneous dielectric media via a true energy functional. *Physical Review Letters*, 109(22), 2012.

[46] Douwe Jan Bonthuis, Stephan Gekle, and Roland R. Netz. Profile of the static permittivity tensor of water at interfaces: Consequences for capacitance, hydration interaction and ion adsorption. *Langmuir*, 28(20):7679–7694, 2012.

[47] Jean-Pierre Hansen and Ian R. McDonald. Chapter 4 - Distribution Function Theories. In Jean-Pierre Hansen and Ian R. McDonald, editors, *Theory of Simple Liquids (Fourth Edition)*, pages 105–147. Academic Press, Oxford, 2013.

[48] F Lado. An efficient procedure for the study of inhomogeneous liquids. *Molecular Physics*, 107(4-6): 301–308, 2009.

[49] Feng-Qi You, Yang-Xin Yu, and Guang-Hua Gao. Structure of inhomogeneous attractive and repulsive hard-core yukawa fluid: Grand canonical monte carlo simulation and density functional theory study. *The Journal of Physical Chemistry B*, 109(8):3512–3518, 2005.

[50] Yang-Xin Yu, Feng-Qi You, Yiping Tang, Guang-Hua Gao, and Yi-Gui Li. Structure and adsorption of a hard-core multi-yukawa fluid confined in a slitlike pore: grand canonical monte carlo simulation and density functional study. *The Journal of Physical Chemistry B*, 110(1):334–341, 2006.

[51] Søren Toxvaerd. Hydrostatic equilibrium in fluid interfaces. *Journal of Chemical Physics*, 64:2863–2867, 1976.

[52] Jonathan C Barrett. Some estimates of the surface tension of curved surfaces using density functional theory. *The journal of chemical physics*, 124(14):144705, 2006.

[53] Guy J Gloor, George Jackson, FJ Blas, E Martin Del Rio, and E De Miguel. Prediction of the vapor-liquid interfacial tension of nonassociating and associating fluids with the saft-vr density functional theory. *The Journal of Physical Chemistry C*, 111(43):15513–15522, 2007.

[54] Alireza Moradzadeh and Narayana R Aluru. Transfer-learning-based coarse-graining method for simple fluids: Toward deep inverse liquid-state theory. *The journal of physical chemistry letters*, 10(6):1242–1250, 2019.

[55] Yiping Tang and Jianzhong Wu. A density-functional theory for bulk and inhomogeneous Lennard-Jones fluids from the energy route. *The Journal of Chemical Physics*, 119(14):7388–7397, 2003.

[56] J. A. Barker and D. Henderson. Perturbation theory and equation of state for fluids. II. a successful theory of liquids. *The Journal of Chemical Physics*, 47:4714–4721, 1967.

[57] JL Lebowitz. Exact solution of generalized percus-yevick equation for a mixture of hard spheres. *Physical Review*, 133(4A):A895, 1964.

[58] PJ Leonard, D Henderson, and JA Barker. Calculation of the radial distribution function of hard-sphere mixtures in the percus-yevick approximation. *Molecular Physics*, 21(1):107–111, 1971.

[59] Paho Lurie-Gregg, Jeff B Schulte, and David Roundy. Approach to approximating the pair distribution function of inhomogeneous hard-sphere fluids. *Physical Review E*, 90(4):042130, 2014.

[60] John D Weeks, David Chandler, and Hans C Andersen. Role of repulsive forces in determining the equilibrium structure of simple liquids. *The Journal of chemical physics*, 54(12):5237–5247, 1971.

[61] Yaakov Rosenfeld. Free-energy model for the inhomogeneous hard-sphere fluid mixture and density-functional theory of freezing. *Physical Review Letters*, 63(9):980, 1989.

[62] R. Roth, R. Evans, A. Lang, and G. Kahl. Fundamental measure theory for hard-sphere mixtures revisited: the white bear version. *Journal of Physics: Condensed Matter*, 14(46):12063, 2002.

[63] Roland Roth. Fundamental measure theory for hard-sphere mixtures: a review. *Journal of Physics: Condensed Matter*, 22(6):063102, 2010.

[64] Suresh K Bhatia and David Nicholson. Modeling mixture transport at the nanoscale: Departure from existing paradigms. *Physical review letters*, 100(23):236103, 2008.

[65] Sander Pronk, Szilrd Pll, Roland Schulz, Per Larsson, Pr Bjelkmar, Rossen Apostolov, Michael R. Shirts, Jeremy C. Smith, Peter M. Kasson, David van der Spoel, Berk Hess, and Erik Lindahl. Gromacs 4.5: a high-throughput and highly parallel open source molecular simulation toolkit. *Bioinformatics*, 29(7):845, 2013.

[66] Shuichi Nosé. A unified formulation of the constant temperature molecular dynamics methods. *The Journal of chemical physics*, 81(1):511–519, 1984.

[67] IK Snook and W Van Megen. Solvation forces in simple dense fluids. i. *The Journal of Chemical Physics*, 72(5):2907–2913, 1980.

[68] Sanjit K Das, Mukul M Sharma, and Robert S Schechter. Solvation force in confined molecular fluids using molecular dynamics simulation. *The Journal of Physical Chemistry*, 100(17):7122–7129, 1996.

[69] Eckhard Spohr, Andrij Trokhymchuk, and Douglas Henderson. Adsorption of water molecules in slit pores. *Journal of Electroanalytical Chemistry*, 450(2):281–287, 1998.

[70] M Sliwinska-Bartkowiak, R Sikorski, SL Sowers, LD Gelb, and KE Gubbins. Phase separations for mixtures in well-characterized porous materials: Liquid–liquid transitions. *Fluid phase equilibria*, 136 (1-2):93–109, 1997.

[71] Marco Gallo, Tina M Nenoff, and Martha C Mitchell. Selectivities for binary mixtures of hydrogen/methane and hydrogen/carbon dioxide in silicalite and ets-10 by grand canonical monte carlo techniques. *Fluid phase equilibria*, 247(1-2):135–142, 2006.

[72] Chong Gu, Guang-Hua Gao, Yang-Xin Yu, and Tomoshige Nitta. Simulation for separation of hydrogen and carbon monoxide by adsorption on single-walled carbon nanotubes. *Fluid Phase Equilibria*, 194: 297–307, 2002.

[73] Roger F Cracknell, David Nicholson, Stephen R Tennison, and Jill Bromhead. Adsorption and selectivity of carbon dioxide with methane and nitrogen in slit-shaped carbonaceous micropores: simulation and experiment. *Adsorption*, 2(3):193–203, 1996.

[74] Benoit Coasne, Joanna Czwartos, Malgorzata Sliwinska-Bartkowiak, and Keith E Gubbins. Freezing of mixtures confined in silica nanopores: experiment and molecular simulation. *The Journal of chemical physics*, 133(8):084701, 2010.

[75] R Evans. Density functional theory for inhomogeneous fluids i: Simple fluids in equilibrium. *Lecture Notes at 3rd Warsaw School of Statistical Physics, Kazimierz Dolny*, 27:43, 2009.

[76] J. Z. Wu. Density functional theory for liquid structure and thermodynamics. In Xiaohua Lu and Ying Hu, editors, *Molecular Thermodynamics of Complex Systems*, number 131 in Structure and Bonding, pages 1–73. Springer Berlin Heidelberg, 2009.

[77] Hartmut Löwen. Density functional theory of inhomogeneous classical fluids: recent developments and new perspectives. *Journal of Physics: Condensed Matter*, 14(46):11897, 2002.

[78] Shuangliang Zhao, Honglai Liu, Rosa Ramirez, and Daniel Borgis. Accurate evaluation of the angular-dependent direct correlation function of water. *The Journal of chemical physics*, 139(3):034503, 2013.

[79] Yang-Xin Yu and Jianzhong Wu. Density functional theory for inhomogeneous mixtures of polymeric fluids. *The Journal of chemical physics*, 117(5):2368–2376, 2002.

[80] Yang-Xin Yu, Jianzhong Wu, Yu-Xuan Xin, and Guang-Hua Gao. Structures and correlation functions of multicomponent and polydisperse hard-sphere mixtures from a density functional theory. *The Journal of chemical physics*, 121(3):1535–1541, 2004.

[81] Yang-Xin Yu. A novel weighted density functional theory for adsorption, fluid-solid interfacial tension, and disjoining properties of simple liquid films on planar solid surfaces. *The Journal of chemical physics*, 131(2):024704, 2009.

[82] Bo Peng and Yang-Xin Yu. A density functional theory with a mean-field weight function: applications to surface tension, adsorption, and phase transition of a lennard-jones fluid in a slit-like pore. *The Journal of Physical Chemistry B*, 112(48):15407–15416, 2008.

[83] Lourdes F. Vega and George Jackson. 20 years of the SAFT equation of stateRecent advances and challenges: Symposium held in bellaterra, barcelona, 1921 september 2010. *Fluid Phase Equilibria*, 306(1):1–3, 2011.

[84] Jessica Hughes, Eric J Krebs, and David Roundy. A classical density-functional theory for describing water interfaces. *The Journal of chemical physics*, 138(2):024509, 2013.

[85] Kai Gong, Bennett D Marshall, and Walter G Chapman. Modeling lower critical solution temperature behavior of associating polymer brushes with classical density functional theory. *The Journal of chemical physics*, 139(9):094904, 2013.

[86] Eric J Krebs, Jeff B Schulte, and David Roundy. Improved association in a classical density functional theory for water. *The Journal of chemical physics*, 140(12):124507, 2014.

[87] Oliver Berger, Olle Edholm, and Fritz Jähnig. Molecular dynamics simulations of a fluid bilayer of dipalmitoylphosphatidylcholine at full hydration, constant pressure, and constant temperature. *Biophysical journal*, 72(5):2002, 1997.

[88] Enrique de Miguel and George Jackson. The nature of the calculation of the pressure in molecular simulations of continuous models from volume perturbations. *The Journal of Chemical Physics*, 125: 164109, 2006.

[89] E Kierlik, Y Fan, PA Monson, and ML Rosinberg. Liquid–liquid equilibrium in a slit pore: Monte carlo simulation and mean field density functional theory. *The Journal of chemical physics*, 102(9): 3712–3719, 1995.

[90] J.R. Henderson and Frank van Swol. On the interface between a fluid and a planar wall. *Molecular Physics*, 51(4):991–1010, 1984.

[91] Frank van Swol and J. R. Henderson. Wetting and drying transitions at a fluid-wall interface: Density-functional theory versus computer simulation. *Physical Review A*, 40(5):2567–2578, 1989.

[92] Michael P Allen. Pressure tensor profiles at the isotropic–nematic interface. *Chemical Physics Letters*, 331(5):513–518, 2000.

[93] John G. Kirkwood and Frank P. Buff. The statistical mechanical theory of surface tension. *The Journal of Chemical Physics*, 17(3):338–343, 1949.

[94] Song Hi Lee, Jayendran C Rasaiah, and JB Hubbard. Molecular dynamics study of a dipolar fluid between charged plates. ii. *The Journal of chemical physics*, 86(4):2383–2393, 1987.

[95] Juan M. Vanegas, Alejandro Torres-Snchez, and Marino Arroyo. Importance of Force Decomposition for Local Stress Calculations in Biomembrane Molecular Simulations. *Journal of Chemical Theory and Computation*, 10:691–702, 2014.

[96] Pradeep Kumar, Sergey V Buldyrev, Francis W Starr, Nicolas Giovambattista, and H Eugene Stanley. Thermodynamics, structure, and dynamics of water confined between hydrophobic plates. *Physical Review E*, 72(5):051503, 2005.

[97] Jacob Klein and Eugenia Kumacheva. Confinement-induced phase transitions in simple liquids. *Science*, 269(5225):816, 1995.

[98] M. Heuberger, M. Zch, and N. D. Spencer. Density fluctuations under confinement: When is a fluid not a fluid? *Science*, 292(5518):905–908, 2001.

[99] Yun Long, Jeremy C. Palmer, Benoit Coasne, Magorzata liwinska Bartkowiak, George Jackson, Erich A. Mller, and Keith E. Gubbins. On the molecular origin of high-pressure effects in nanoconfinement: The role of surface chemistry and roughness. *The Journal of Chemical Physics*, 139(14): 144701, 2013.

[100] Keith E Gubbins, Yun Long, and Małgorzata Śliwinska-Bartkowiak. Thermodynamics of confined nano-phases. *The Journal of Chemical Thermodynamics*, 74:169–183, 2014.

[101] Benoit Coasne, Y Long, and KE Gubbins. Pressure effects in confined nanophases. *Molecular Simulation*, 40(7-9):721–730, 2014.

[102] Hossein Eslami and Nargess Mehdipour. Local chemical potential and pressure tensor in inhomogeneous nanoconfined fluids. *The Journal of chemical physics*, 137(14):144702, 2012.

[103] Jacob Israelachvili and Håkan Wennerström. Role of hydration and water structure in biological and colloidal interactions. *Nature*, 379(6562):219, 1996.

[104] Douwe Jan Bonthuis, Stephan Gekle, and Roland R Netz. Profile of the static permittivity tensor of water at interfaces: Consequences for capacitance, hydration interaction and ion adsorption. *Langmuir*, 28(20):7679–7694, 2012.

[105] Mark A Shannon, Paul W Bohn, Menachem Elimelech, and John G Georgiadis. Science and technology for water purification in the coming decades. *Nature*, 452(7185):301–310, 2008.

[106] Mohammad Heiranian, Amir Barati Farimani, and Narayana R Aluru. Water desalination with a single-layer mos 2 nanopore. *Nature Communications*, 6:8616, 2015.

[107] Ken A Dill. Dominant forces in protein folding. *Biochemistry*, 29(31):7133–7155, 1990.

[108] Marie-Claire Bellissent-Funel, Ali Hassanali, Martina Havenith, Richard Henchman, Peter Pohl, Fabio Sterpone, David van der Spoel, Yao Xu, and Angel E Garcia. Water determines the structure and dynamics of proteins. *Chemical Reviews*, 116(13):7673–7697, 2016.

[109] Arieh Ben-Naim. *Molecular Theory of Water and Aqueous Solutions: The role of water in protein folding, self-assembly and molecular recognition*, volume 2. World Scientific, 2011.

[110] Douwe Jan Bonthuis, Stephan Gekle, and Roland R Netz. Dielectric profile of interfacial water and its effect on double-layer capacitance. *Physical Review Letters*, 107(16):166102, 2011.

[111] Michel Armand, Frank Endres, Douglas R MacFarlane, Hiroyuki Ohno, and Bruno Scrosati. Ionic-liquid materials for the electrochemical challenges of the future. In *Materials For Sustainable Energy: A Collection of Peer-Reviewed Research and Review Articles from Nature Publishing Group*, pages 129–137. World Scientific, 2011.

[112] Karlheinz Graf, Michael Kappl, et al. *Physics and Chemistry of Interfaces*. John Wiley & Sons, 2006.

[113] R Qiao and NR Aluru. Charge inversion and flow reversal in a nanochannel electro-osmotic flow. *Physical Review Letters*, 92(19):198301, 2004.

[114] K Michael Salerno, Amalie L Frischknecht, and Mark J Stevens. Charged nanoparticle attraction in multivalent salt solution: A classical-fluids density functional theory and molecular dynamics study. *The Journal of Physical Chemistry B*, 120(26):5927–5937, 2016.

[115] Harry A Stern and Scott E Feller. Calculation of the dielectric permittivity profile for a nonuniform system: application to a lipid bilayer simulation. *The Journal of Chemical Physics*, 118(7):3401–3412, 2003.

[116] Christian Schaaf and Stephan Gekle. Spatially resolved dielectric constant of confined water and its connection to the non-local nature of bulk water. *The Journal of Chemical Physics*, 145(8):084901, 2016.

[117] PIC Teixeira, JM Tavares, and MM Telo da Gama. The effect of dipolar forces on the structure and thermodynamics of classical fluids. *Journal of Physics: Condensed Matter*, 12(33):R411, 2000.

[118] Vladimir A Froltsov and Sabine HL Klapp. Anisotropic dynamics of dipolar liquids in narrow slit pores. *The Journal of Chemical Physics*, 124(13):134701, 2006.

[119] Gabriele Raabe and Richard J Sadus. Molecular dynamics simulation of the dielectric constant of water: The effect of bond flexibility. *The Journal of Chemical Physics*, 134(23):234501, 2011.

[120] Sereina Riniker and Wilfred F van Gunsteren. A simple, efficient polarizable coarse-grained water model for molecular dynamics simulations. *The Journal of Chemical Physics*, 134(8):084110, 2011.

[121] Walter H Stockmayer. Second virial coefficients of polar gases. *The Journal of Chemical Physics*, 9 (5):398–402, 1941.

[122] Dušan Bratko, L Blum, and Alenka Luzar. A simple model for the intermolecular potential of water. *The Journal of Chemical Physics*, 83(12):6367–6370, 1985.

[123] Edgar Ávalos, Fernando del Río, and Santiago Lago. Nonconformal interaction models and thermodynamics of polar fluids. *The Journal of Physical Chemistry B*, 109(1):508–517, 2005.

[124] Tonalli Rodríguez-López, Yuriy Khalak, and Mikko Karttunen. Non-conformal coarse-grained potentials for water. *The Journal of Chemical Physics*, 147(13):134108, 2017.

[125] Mario Orsi and Jonathan W Essex. The elba force field for coarse-grain modeling of lipid membranes. *PLoS One*, 6(12):e28637, 2011.

[126] Mario Orsi. Comparative assessment of the elba coarse-grained model for water. *Molecular Physics*, 112(11):1566–1576, 2014.

[127] Patrick G Lafond and Sergei Izvekov. Multiscale coarse-graining of polarizable models through force-matched dipole fluctuations. *Journal of Chemical Theory and Computation*, 12(12):5737–5750, 2016.

[128] Alireza Moradzadeh, Mohammad H Motevaselian, Sikandar Y Mashayak, and Narayana R Aluru. Coarse-grained force field for imidazolium-based ionic liquids. *Journal of Chemical Theory and Computation*, 2018.

[129] V Ballenegger and J-P Hansen. Structure and dielectric properties of polar fluids with extended dipoles: results from numerical simulations. *Molecular Physics*, 102(6):599–609, 2004.

[130] Dirk Reith, Mathias Pütz, and Florian Müller-Plathe. Deriving effective mesoscale potentials from atomistic simulations. *Journal of Computational Chemistry*, 24(13):1624–1636, 2003.

[131] Alexander P Lyubartsev and Aatto Laaksonen. Calculation of effective interaction potentials from radial distribution functions: A reverse monte carlo approach. *Physical Review E*, 52(4):3730, 1995.

[132] M Scott Shell. The relative entropy is fundamental to multiscale and inverse thermodynamic problems. *The Journal of Chemical Physics*, 129(14):144108, 2008.

[133] Aviel Chaimovich and M Scott Shell. Coarse-graining errors and numerical optimization using a relative entropy framework. *The Journal of Chemical Physics*, 134(9):094112, 2011.

[134] SY Mashayak, Mara N Jochum, Konstantin Koschke, NR Aluru, Victor Rühle, and Christoph Junghans. Relative entropy and optimization-driven coarse-graining methods in votca. *PLoS one*, 10(7): e0131754, 2015.

[135] Martin Neumann. Dipole moment fluctuation formulas in computer simulations of polar systems. *Molecular Physics*, 50(4):841–858, 1983.

[136] Manu Sharma, Raffaele Resta, and Roberto Car. Dipolar correlations and the dielectric permittivity of water. *Physical Review Letters*, 98(24):247401, 2007.

[137] Han Wang, Christoph Junghans, and Kurt Kremer. Comparative atomistic and coarse-grained study of water: What do we lose by coarse-graining? *The European Physical Journal E*, 28(2):221–229, 2009.

[138] Chia-Chun Fu, Pandurang M Kulkarni, M Scott Shell, and L Gary Leal. A test of systematic coarse-graining of molecular dynamics simulations: Transport properties. *The Journal of Chemical Physics*, 139(9):094107, 2013.

[139] Tanmoy Sanyal and M Scott Shell. Coarse-grained models using local-density potentials optimized with the relative entropy: Application to implicit solvation. *The Journal of Chemical Physics*, 145(3): 034109, 2016.

[140] Jacob W Wagner, Thomas Dannenhoffer-Lafage, Jaehyeok Jin, and Gregory A Voth. Extending the range and physical accuracy of coarse-grained models: Order parameter dependent interactions. *The Journal of Chemical Physics*, 147(4):044113, 2017.

[141] Sergei Izvekov and Gregory A Voth. A multiscale coarse-graining method for biomolecular systems. *The Journal of Physical Chemistry B*, 109(7):2469–2473, 2005.

[142] Sergei Izvekov and Gregory A Voth. Multiscale coarse graining of liquid-state systems. *The Journal of Chemical Physics*, 123(13):134105, 2005.

[143] Anna Oleksy and Jean-Pierre Hansen. Wetting of a solid substrate by a civilized model of ionic solutions. *The Journal of chemical physics*, 132(20):204702, 2010.

[144] Mark James Abraham, Teemu Murtola, Roland Schulz, Szilárd Páll, Jeremy C Smith, Berk Hess, and Erik Lindahl. Gromacs: High performance molecular simulations through multi-level parallelism from laptops to supercomputers. *SoftwareX*, 1:19–25, 2015.

[145] Jean-Paul Ryckaert, Giovanni Ciccotti, and Herman JC Berendsen. Numerical integration of the cartesian equations of motion of a system with constraints: molecular dynamics of n-alkanes. *Journal of Computational Physics*, 23(3):327–341, 1977.

[146] Ariel A Chialvo and Peter T Cummings. Molecular-based modeling of water and aqueous solutions at supercritical conditions. *Advances in Chemical Physics*, 109:115–206, 1999.

[147] Tom Darden, Darrin York, and Lee Pedersen. Particle mesh ewald: An n log (n) method for ewald sums in large systems. *The Journal of Chemical Physics*, 98(12):10089–10092, 1993.

[148] Please see https://github.com/Hosseinmote/Extended-Dipole-Model-for-Polar-Liquids.

[149] Gerald Mathias and Paul Tavan. Angular resolution and range of dipole–dipole correlations in water. *The Journal of Chemical Physics*, 120(9):4393–4403, 2004.

[150] MSt Wertheim. Exact solution of the mean spherical model for fluids of hard spheres with permanent electric dipole moments. *The Journal of Chemical Physics*, 55(9):4291–4298, 1971.

[151] Jean-Pierre Hansen and Ian R McDonald. *Theory of Simple Liquids*. Elsevier, 1990.

[152] David P Shelton. Long-range orientation correlation in liquids. *The Journal of Chemical Physics*, 136 (4):044503, 2012.

[153] David P Shelton. Long-range orientation correlation in water. *The Journal of Chemical Physics*, 141 (22):224506, 2014.

[154] J Maruthi Pradeep Kanth, Satyavani Vemparala, and Ramesh Anishetty. Long-distance correlations in molecular orientations of liquid water and shape-dependent hydrophobic force. *Physical Review E*, 81(2):021201, 2010.

[155] Yu Liu and Jianzhong Wu. Communication: Long-range angular correlations in liquid water. *The Journal of Chemical Physics*, 139:041103, 2013.

[156] Cui Zhang and Giulia Galli. Dipolar correlations in liquid water. *The Journal of Chemical Physics*, 141(8):084504, 2014.

[157] Quinn Alexander Besford, Andrew Joseph Christofferson, Maoyuan Liu, and Irene Yarovsky. Long-range dipolar order and dispersion forces in polar liquids. *The Journal of Chemical Physics*, 147(19): 194503, 2017.

[158] Saul Goldman and Chris Joslin. Why hydrogen-bonded liquids tend to have high static dielectric constants. *The Journal of Physical Chemistry*, 97(47):12349–12355, 1993.

[159] Chao Zhang, Jurg Hutter, and Michiel Sprik. Computing the kirkwood g-factor by combining constant maxwell electric field and electric displacement simulations: application to the dielectric constant of liquid water. *The Journal of Physical Chemistry Letters*, 7(14):2696–2701, 2016.

[160] Upayan Baul, J Maruthi Pradeep Kanth, Ramesh Anishetty, and Satyavani Vemparala. Effect of simple solutes on the long range dipolar correlations in liquid water. *The Journal of Chemical Physics*, 144(10):104502, 2016.

[161] Ateeque Malani, KG Ayappa, and Sohail Murad. Influence of hydrophilic surface specificity on the structural properties of confined water. *The Journal of Physical Chemistry B*, 113(42):13825–13839, 2009.

[162] Dimitrios Argyris, Naga Rajesh Tummala, Alberto Striolo, and David R Cole. Molecular structure and dynamics in thin water films at the silica and graphite surfaces. *The Journal of Physical Chemistry C*, 112(35):13587–13599, 2008.

[163] Leandro B Krott and Marcia C Barbosa. Anomalies in a waterlike model confined between plates. *The Journal of Chemical Physics*, 138(8):084505, 2013.

[164] V Ballenegger and J-P Hansen. Dielectric permittivity profiles of confined polar fluids. *The Journal of Chemical Physics*, 122(11):114711, 2005.

[165] Cui Zhang, Francois Gygi, and Giulia Galli. Strongly anisotropic dielectric relaxation of water at the nanoscale. *The Journal of Physical Chemistry Letters*, 4(15):2477–2481, 2013.

[166] Richard Renou, Anthony Szymczyk, Guillaume Maurin, Patrice Malfreyt, and Aziz Ghoufi. Superpermittivity of nanoconfined water. *The Journal of Chemical Physics*, 142(18):184706, 2015.

[167] Anna Oleksy and Jean-Pierre Hansen. Microscopic density functional theory of wetting and drying of a solid substrate by an explicit solvent model of ionic solutions. *Molecular Physics*, 107(23-24): 2609–2624, 2009.

[168] Vadim Warshavsky and Marcelo Marucho. Polar-solvation classical density-functional theory for electrolyte aqueous solutions near a wall. *Physical Review E*, 93(4):042607, 2016.

[169] L. Fumagalli, A. Esfandiar, R. Fabregas, S. Hu, P. Ares, A. Janardanan, Q. Yang, B. Radha, T. Taniguchi, K. Watanabe, G. Gomila, K. S. Novoselov, and A. K. Geim. Anomalously low dielectric constant of confined water. *Science*, 360(6395):1339–1342, 2018.

[170] Akira Sugahara, Yasunobu Ando, Satoshi Kajiyama, Koji Yazawa, Kazuma Gotoh, Minoru Otani, Masashi Okubo, and Atsuo Yamada. Negative dielectric constant of water confined in nanosheets. *Nature Communications*, 10(1), 2019.

[171] Cheng-Peng Li and Miao Du. Role of solvents in coordination supramolecular systems. *Chemical Communications*, 47(21):5958, 2011.

[172] Richard M. Noyes. Thermodynamics of ion hydration as a measure of effective dielectric properties of water. *Journal of the American Chemical Society*, 84(4):513–522, 1962.

[173] Yuki Uematsu, Roland R. Netz, and Douwe Jan Bonthuis. Analytical interfacial layer model for the capacitance and electrokinetics of charged aqueous interfaces. *Langmuir*, 34(31):9097–9113, 2018.

[174] Samuel Faucher, Narayana Aluru, Martin Z. Bazant, Daniel Blankschtein, Alexandra H. Brozena, John Cumings, J. Pedro de Souza, Menachem Elimelech, Razi Epsztein, John T. Fourkas, Ananth Govind Rajan, Heather J. Kulik, Amir Levy, Arun Majumdar, Charles Martin, Michael McEldrew, Rahul Prasanna Misra, Aleksandr Noy, Tuan Anh Pham, Mark Reed, Eric Schwegler, Zuzanna Siwy, YuHuang Wang, and Michael Strano. Critical knowledge gaps in mass transport through single-digit nanopores: A review and perspective. *The Journal of Physical Chemistry C*, 123(35):21309–21326, 2019.

[175] Marie-Claire Bellissent-Funel, Ali Hassanali, Martina Havenith, Richard Henchman, Peter Pohl, Fabio Sterpone, David van der Spoel, Yao Xu, and Angel E Garcia. Water determines the structure and dynamics of proteins. *Chemical Reviews*, 116(13):7673–7697, 2016.

[176] Mark A. Shannon, Paul W. Bohn, Menachem Elimelech, John G. Georgiadis, Benito J. Mariñas, and Anne M. Mayes. Science and technology for water purification in the coming decades. *Nature*, 452 (7185):301–310, 2008.

[177] Mohammad Heiranian, Amir Barati Farimani, and Narayana R. Aluru. Water desalination with a single-layer MoS2 nanopore. *Nature Communications*, 6(1), 2015.

[178] Michael F. Toney, Jason N. Howard, Jocelyn Richer, Gary L. Borges, Joseph G. Gordon, Owen R. Melroy, David G. Wiesler, Dennis Yee, and Larry B. Sorensen. Voltage-dependent ordering of water molecules at an electrode–electrolyte interface. *Nature*, 368(6470):444–446, 1994.

[179] G. Algara-Siller, O. Lehtinen, F. C. Wang, R. R. Nair, U. Kaiser, H. A. Wu, A. K. Geim, and I. V. Grigorieva. Square ice in graphene nanocapillaries. *Nature*, 519(7544):443–445, 2015.

[180] M. H. Motevaselian, S. Y. Mashayak, and N. R. Aluru. Extended coarse-grained dipole model for polar liquids: Application to bulk and confined water. *Physical Review E*, 98(5), 2018.

[181] Stanislav Parez, Milan Předota, and Michael Machesky. Dielectric properties of water at rutile and graphite surfaces: Effect of molecular structure. *The Journal of Physical Chemistry C*, 118(9):4818–4834, 2014.

[182] L. S. PALMER, A. CUNLIFFE, and J. M. HOUGH. Dielectric constant of water films. *Nature*, 170 (4332):796–796, 1952.

[183] O. Teschke, G. Ceotto, and E. F. de Souza. Interfacial water dielectric-permittivity-profile measurements using atomic force microscopy. *Physical Review E*, 64(1), 2001.

[184] Philip Loche, Amanuel Wolde-Kidan, Alexander Schlaich, Douwe Jan Bonthuis, and Roland R. Netz. Comment on "hydrophobic surface enhances electrostatic interaction in water". *Physical Review Letters*, 123(4), 2019.

[185] John G. Kirkwood. The dielectric polarization of polar liquids. *The Journal of Chemical Physics*, 7 (10):911–919, 1939.

[186] H. Frhlich and A. Maradudin. Theory of dielectrics. *Physics Today*, 12(2):40–42, 1959.

[187] Jordi Faraudo and Fernando Bresme. Anomalous dielectric behavior of water in ionic newton black films. *Physical Review Letters*, 92(23), 2004.

[188] Cui Zhang, François Gygi, and Giulia Galli. Strongly anisotropic dielectric relaxation of water at the nanoscale. *The Journal of Physical Chemistry Letters*, 4(15):2477–2481, 2013.

[189] Sergio De Luca, Sridhar Kumar Kannam, B. D. Todd, Federico Frascoli, J. S. Hansen, and Peter J. Daivis. Effects of confinement on the dielectric response of water extends up to mesoscale dimensions. *Langmuir*, 32(19):4765–4773, 2016.

[190] A. Ghoufi, A. Szymczyk, R. Renou, and M. Ding. Calculation of local dielectric permittivity of confined liquids from spatial dipolar correlations. *EPL (Europhysics Letters)*, 99(3):37008, 2012.

[191] Sayantan Mondal and Biman Bagchi. Water in carbon nanotubes: Pronounced anisotropy in dielectric dispersion and its microscopic origin. *The Journal of Physical Chemistry Letters*, 10(20):6287–6292, 2019.

[192] Takato Sato, Tohru Sasaki, Jun Ohnuki, Koji Umezawa, and Mitsunori Takano. Hydrophobic surface enhances electrostatic interaction in water. *Physical Review Letters*, 121(20), 2018.

[193] Alexander Schlaich, Ernst W. Knapp, and Roland R. Netz. Water dielectric effects in planar confinement. *Physical Review Letters*, 117(4), 2016.

[194] Mark James Abraham, Teemu Murtola, Roland Schulz, Szilárd Páll, Jeremy C. Smith, Berk Hess, and Erik Lindahl. GROMACS: High performance molecular simulations through multi-level parallelism from laptops to supercomputers. *SoftwareX*, 1-2:19–25, 2015.

[195] Ariel A. Chialvo and Peter T. Cummings. Molecular-based modeling of water and aqueous solutions at supercritical conditions. In *Advances in Chemical Physics*, pages 115–205. John Wiley & Sons, Inc., 2007.

[196] Tom Darden, Darrin York, and Lee Pedersen. Particle mesh ewald: AnN·log(n) method for ewald sums in large systems. *The Journal of Chemical Physics*, 98(12):10089–10092, 1993.

[197] In-Chul Yeh and Max L. Berkowitz. Ewald summation for systems with slab geometry. *The Journal of Chemical Physics*, 111(7):3155–3162, 1999.

[198] Jean-Paul Ryckaert, Giovanni Ciccotti, and Herman J.C Berendsen. Numerical integration of the cartesian equations of motion of a system with constraints: molecular dynamics of n-alkanes. *Journal of Computational Physics*, 23(3):327–341, 1977.

[199] Alexei M. Nikitin and Alexander P. Lyubartsev. New six-site acetonitrile model for simulations of liquid acetonitrile and its aqueous mixtures. *Journal of Computational Chemistry*, 28(12):2020–2026, 2007.

[200] Carl Caleman, Paul J. van Maaren, Minyan Hong, Jochen S. Hub, Luciano T. Costa, and David van der Spoel. Force field benchmark of organic liquids: Density, enthalpy of vaporization, heat capacities, surface tension, isothermal compressibility, volumetric expansion coefficient, and dielectric constant. *Journal of Chemical Theory and Computation*, 8(1):61–74, 2011.

[201] Zhu Liu, Jakob Timmermann, Karsten Reuter, and Christoph Scheurer. Benchmarks and dielectric constants for reparametrized OPLS and polarizable force field models of chlorinated hydrocarbons. *The Journal of Physical Chemistry B*, 122(2):770–779, 2017.

[202] Manu Sharma, Raffaele Resta, and Roberto Car. Dipolar correlations and the dielectric permittivity of water. *Physical Review Letters*, 98(24), 2007.

[203] C. Merlet, C. Péan, B. Rotenberg, P. A. Madden, B. Daffos, P. L. Taberna, P. Simon, and M. Salanne. Highly confined ions store charge more efficiently in supercapacitors. *Nature Communications*, 4(1), 2013.

[204] J. L. Aragones, L. G. MacDowell, and C. Vega. Dielectric constant of ices and water: A lesson about water interactions. *The Journal of Physical Chemistry A*, 115(23):5745–5758, 2011.

[205] F. Booth. The dielectric constant of water and the saturation effect. *The Journal of Chemical Physics*, 19(4):391–394, 1951.

[206] F. Booth. Errata: The dielectric constant of water and the saturation effect. *The Journal of Chemical Physics*, 19(10):1327–1328, 1951.

[207] Isaak N. Daniels, Zhenxing Wang, and Brian B. Laird. Dielectric properties of organic solvents in an electric field. *The Journal of Physical Chemistry C*, 121(2):1025–1031, 2017.

[208] Nir Gavish and Keith Promislow. Dependence of the dielectric constant of electrolyte solutions on ionic concentration: A microfield approach. *Physical Review E*, 94(1), 2016.

[209] Esther Heid, Borja Docampo-Álvarez, Luis M. Varela, Konstantin Prosenz, Othmar Steinhauser, and Christian Schrder. Langevin behavior of the dielectric decrement in ionic liquid water mixtures. *Physical Chemistry Chemical Physics*, 20(22):15106–15117, 2018.

[210] S. Y. Mashayak and N. R. Aluru. Langevin-poisson-EQT: A dipolar solvent based quasi-continuum approach for electric double layers. *The Journal of Chemical Physics*, 146(4):044108, 2017.

[211] Massimiliano Stengel and Nicola A. Spaldin. Origin of the dielectric dead layer in nanoscale capacitors. *Nature*, 443(7112):679–682, 2006.

[212] Li-Wu Chang, Marin Alexe, James F. Scott, and J. Marty Gregg. Settling the "dead layer" debate in nanoscale capacitors. *Advanced Materials*, 21(48):4911–4914, 2009.

[213] Timothy Duignan and Xiu Song Zhao. Impurities limit the capacitance of carbon based supercapacitors. 2018.

[214] Jeronimo Terrones, Patrick J. Kiley, and James A. Elliott. Enhanced ordering reduces electric susceptibility of liquids confined to graphene slit pores. *Scientific Reports*, 6(1), 2016.

[215] Wenpeng Qi and Hongwei Zhao. Hydrogen bond network in the hydration layer of the water confined in nanotubes increasing the dielectric constant parallel along the nanotube axis. *The Journal of chemical physics*, 143(11):114708, 2015.

[216] Sleeba Varghese, Sridhar Kumar Kannam, Jesper Schmidt Hansen, and Sarith P. Sathian. Effect of hydrogen bonds on the dielectric properties of interfacial water. *Langmuir*, 35(24):8159–8166, 2019.

[217] Daniel Munoz-Santiburcio and Dominik Marx. Chemistry in nanoconfined water. *Chemical science*, 8 (5):3444–3452, 2017.